

Copyright Notices

Notice 1

Under the Copyright Act 1968, this thesis must be used only under the normal conditions of scholarly fair dealing. In particular no results or conclusions should be extracted from it, nor should it be copied or closely paraphrased in whole or in part without the written consent of the author. Proper written acknowledgement should be made for any assistance obtained from this thesis.

Notice 2

I certify that I have made all reasonable efforts to secure copyright permissions for third-party content included in this thesis and have not knowingly added copyright content to my work without the owner's permission.

Numerical investigation of the gas and particle dynamics during the cold spray process

Shuo Li

A Thesis submitted to Monash University
for the degree of
Doctor of Philosophy

June 2011

Department of Mechanical and Aerospace Engineering
Monash University

Statement of Originality

This thesis contains no material that has been accepted for the award of a degree or diploma in this or any other university. To the best of the candidate's knowledge and belief, this thesis contains no material previously published or written by another person except where due reference is made in the text of this thesis.'

Candidate: Shuo Li

<Submission Date>

*Conversation enriches the understanding,
but solitude is the school of genius.*
- *Edward Gibbon*

Acknowledgments

I would like to thank first and foremost my principal supervisor Professor Julio Soria for his support and guidance throughout the candidature. Our discussions regarding the nature scientific research have been both insightful and memorable. I should also extend my thanks to my co-supervisors Professor Barry Muddle and Dr. Mahnaz Jahedi for funding this unique research collaboration and acknowledge the computational resources provided by the Victorian Partnership for Advanced Computing. Throughout the years, I have had the benefit of meeting and making many friends from both the undergraduate, postgraduate and academic level. I can honestly say that without their friendship and support, the experience of doing a PhD would have been less interesting and enjoyable. Last but not least, I am very grateful to my family and relatives for encouraging me though the difficult times and keeping me motivated.

Abstract

The present numerical investigation of the cold spray process examines the gas and particle dynamics both inside and outside the nozzle in the context of improving particle deposition. In the first part of the investigation, the one-dimensional isentropic relations coupled with the drag force acting on a particle is employed in a parametric study of the nozzle performance. Next, the addition of a barrel section to the end of the nozzle is proposed and shown to be more efficient in some cases than using the diverging section of the nozzle for particle acceleration. Finally, the effect of nozzle wall friction is incorporated to assess the amount of deviation from the isentropic model.

The gas and particle dynamics between the nozzle and substrate during the steady cold spray process is the focus of the second part of the investigation. An underexpanded and overexpanded nozzle is employed to accelerate the particles and the operating conditions were set to those used in the validation cases. The particle impact statistics are extracted to provide information on the particle impact speed, angle and location. The particles are also tracked during their flight between the nozzle and substrate to characterise their response to changes in the gas flow. It was found that the variation in particle speed across the embedded shock structures became minimal as the diameter increased. For particles with a Stokes number greater than one, the nozzle exit velocity may be used as an approximation of the impact speed. A theoretical model is also proposed for calculating the particle impact speed using the nozzle exit conditions.

The deployment of the shock tube in cold spray is a recent innovation in which a planar shock is released into the ambient air towards a substrate while the particles are injected across the wake of the shock. Although the process suffers from a number of practical limitations, monodisperse particles are used to compare the impact speed produced by steady and unsteady cold spray processes. It was found that this process also offers a mean of studying the shock formation process in underexpanded impinging jets. The shock speeds were selected such that either a shock diamond or Mach disk is reproduced in the impingement region characteristic of a moderately and highly underexpanded jet. Although the unsteady cold spray process requires a much lower driving pressure to produce the impact speeds found during the steady process, there are several practical limitations associated with it.

Nomenclature

Symbol	Description
--------	-------------

Ma	Mach number
Re	Reynolds number
Kn	Knudsen number
PR	pressure ratio (P_e/P_a)
NPR	pressure ratio (P_0/P_a)
C_D	drag coefficient
St	Stokes number
Co	Courant number

1

R	radius
D	diameter
s	standoff distance
L	length
A	cross section area
θ	nozzle divergence angle
x	horizontal axis
y	vertical axis

Continued on the next page.

¹Note that this list excludes the symbols used in the appendices

Continued from previous page.

Symbol	Description
z	axial axis
r	radial axis
t	time
ρ	density
m	mass
u	axial velocity
v	radial velocity
P	pressure
E	total internal energy
T	temperature
c	speed of sound
τ	shear stress
q	heat flux
μ	kinematic viscosity
γ	specific heat ratio
τ_A	particle response time
τ_B	fluid time scale
F_D	drag
U	solution vector
F	inviscid axial flux
G	inviscid radial flux
S	inviscid source flux
A	Jacobian in axial direction
B	Jacobian in radial direction
K	right eigenvector
K ⁻¹	left eigenvector
Λ	diagonal matrix of eigenvalues
W	characteristic solution vector
λ	eigenvalue

Continued on the next page.

Continued from previous page.

Symbol	Description
β	normalised length
ϕ	TVD limiter function
Γ	forward difference of characteristic variables
ζ	'extra' eigenvalue
Δq	magnitude of discontinuity
S_L	left wave
S_R	right wave
S_{HL}	left head wave
S_{HR}	right head wave
S_{TL}	left tail wave
S_{TR}	right tail wave
S^*	contact wave
W_L	left primitive solution vector
W_R	right primitive solution vector
W_{Lfan}	primitive solution vector across left fan
W_{Rfan}	primitive solution vector across right fan
W_L^*	primitive solution vector in left star region
W_R^*	primitive solution vector in right star region
α	forward difference of characteristic variables
ξ	'extra' eigenvalues
φ	4 x 1 matrix for Roe type Riemann solver
Φ	limiter function for Yees Riemann solver
\bar{U}	magnitude of gas velocity
\bar{U}_p	magnitude of particle velocity
Subscript	
0	stagnation flow condition
e	exit flow condition
t	throat flow condition
a	ambient flow condition

Continued on the next page.

Continued from previous page.

Symbol	Description
P	post shock condition
p	particle condition
sh	moving shock
$inlet$	inlet condition
$sonic$	sonic condition
$crit$	critical condition
r	ratio across nozzle exit
L	left state flow conditions
R	right state flow conditions
B	barrel section
D	diverging section
N	nozzle section

Superscript

'	dimensionless value
*	star region flow condition
~	linearised condition

Contents

Introduction	1
1 Background and research aim	3
1.1 Cold spray process	3
1.2 Flow through nozzles	8
1.3 Supersonic free jets	12
1.4 Supersonic impinging jets	16
1.5 Particle-laden flows	23
1.6 Cold spray using shock tubes	24
1.7 Research aim	26
2 Numerical method	29
2.1 Governing equations of fluid motion	29
2.2 Godunov schemes	32
2.2.1 Solution to the Riemann problem	34
2.2.2 Multidimensional extension of the Riemann problem	39
2.3 Approximate Riemann solvers	41
2.3.1 HLLC Riemann solver	41
2.3.2 Roe's Riemann solver	45
2.4 Particle dynamics	51
2.5 Initial conditions	54
2.6 Boundary conditions	58
2.7 Spatial discretization	61
2.8 Temporal discretization	63
3 Results and discussion	65
3.1 Cold spray nozzle dynamics	65
3.1.1 Cold spray nozzle design	66
3.1.2 Parametric study of isentropic nozzle performace	69
3.1.3 Effect of attaching a barrel section to the nozzle	73
3.1.4 Particle acceleration through the nozzle diverging section	84
3.1.5 Discussion of results	85

3.2	Steady cold spray process	94
3.2.1	Numerical validation	95
3.2.2	Particle impact statistics	102
3.2.3	Particle dynamics	104
3.2.4	Discussion of results	108
3.3	Transient cold spray process	113
3.3.1	Numerical validation	113
3.3.2	Flow morphology	115
3.3.3	Particle dynamics	116
3.3.4	Discussion of results	117
4	Conclusions and future work	129
A	Euler equations - Jacobian matrices and eigenvectors	133
B	Total variation diminishing (TVD) schemes	137
C	Compressible flow through a duct with variable cross section area	141

Introduction

Cold gas dynamic spray is an emerging surface coating spray technology developed in the former Soviet Union during the 1980s by Alkhimov *et al.* (Patent No.1618778, Sept 8, 1990). This technology is currently being commercialised in the aeronautical and automotive industry for repair and maintenance purposes. An understanding of supersonic nozzle flow and high speed impinging gas jets is crucial to the development and improvement of the cold spray process. The concept underlying this process is that a supersonic gas jet is generated by passing a pressurised gas through a de-Laval (converging and diverging) nozzle. Particulates of the coating material are then injected inside the nozzle to accelerate them towards a substrate. Provided that the particles achieve sufficient kinetic energy upon impact, they will successfully deposit onto the substrate. It is widely believed that a coating is deposited through intensive plastic deformation of the solid particles (Klinkov *et al.* (2005)). This occurs at a temperature well below the melting point of the spray material - hence the name cold spray - and as a result the disadvantages inherent in traditional thermal spray technologies, such as oxidation and phase transformation, can be avoided. To increase the particle impact speed, the carrier gas is often preheated in the nozzle chamber to temperatures as high as 800 to 1000 K. Particles diameters typically range between 5 and 50 μm and it is believed the impact speed varies somewhere between 500 and 1000 m/s. A wide range of materials such as tin, zinc, aluminium, copper, titanium and iron have been successfully sprayed using this technology (Jodoin *et al.* (2006)).

A review of literature in Chapter.1 indicates that the general flow characteristics of supersonic free and impinging gas jets have been well established through experimentation and simulation. The shock structures were first identified using qualitative techniques such as schlieren and shadowgraphy with pressure measurements along the impingement plate providing additional insight into the impingement region flow. The recent application of quantitative flow visualisation techniques such as PIV has enabled

quantitative information to be extracted from the flow field. The present numerical investigation examines the gas and particle dynamics both inside and outside the nozzle in the context of nozzle performance. This includes the standard steady cold spray process and an unsteady process using a shock tube.

Chapter.2 describes the governing equations and numerical schemes used to model the gas and particle dynamics. For the gas phase, the axisymmetric Euler equations are solved using a total variation diminishing (TVD) version of Roe's approximate Riemann solver (Yee (1990)). A TVD HLLC Riemann solver is also employed to compare the accuracy of the two numerical schemes. Section.2.2 discusses the principles behind Godunov's scheme and the critical role played by the solution to the Riemann problem. The exact solution is presented in Section.2.2.1 and approximations to the solution are covered in Sections.2.3. Assuming low particle loading, the particle phase is decoupled from the gas phase and solved using a Lagrangian discrete particle model presented in Section.2.4. The time integration and the initial and boundary conditions used in the simulations are discussed in Section.2.6.

The numerical data collected for the purpose of the present investigation are presented in Chapter.3. Section.3.1 presents the result of a parametric study examining the effects of the nozzle chamber pressure, temperature and geometry on the particle velocity at the nozzle exit. The benefits of attaching a barrel section to the end of the nozzle is also examined. Section.3.2 presents the data extracted from simulations of the steady cold spray process in the region between the nozzle exit and the substrate. Both an underexpanded and overexpanded nozzle is used to accelerate the particles. The particle impact statistics are calculated followed by an examination of the gas and particle dynamics between the nozzle exit and substrate. From these results, a theoretical model is proposed for calculating the particle impact speed using the nozzle exit conditions. Section.3.3 investigates an unsteady cold spray process produced by the impingement of a planar shock onto a substrate. The flow morphology is visualised using a numerical schlieren technique and is complemented with both streamwise and spanwise data. Particles are injected across the shock tube exit to assess the particle response in a transient high speed impinging jet. The conclusions drawn from the present investigation are summarised in Chapter.4 along with several recommendations for future research.

Chapter 1

Background and research aim

The chapter begins with a review of the research that has been done on the cold spray process Section.1.1. A discussion of the nozzle operating conditions required for cold spraying is also included. It is clear from the numerical and experimental studies of cold spray that the emphasis has been on process optimisation with few attempts at understanding the underlying physics. To gain a better understanding of the particle-laden supersonic impinging jet underlying the cold spray process, one needs to consult the fluid mechanics literature. The following five sections are an attempt to extract and summarise the information most relevant to cold spray. A review of the flow through supersonic nozzles is presented in Section.1.2 followed by a discussion on supersonic free and impinging gas jets in Sections.1.3 and 1.4 respectively. The chapter concludes with an overview of the research on particle laden compressible flow (Section.1.5) and the recent deployment of shock tube technology in cold spray (Section.1.6). The aims of the present investigation are outlined in Section.1.7.

1.1 Cold spray process

During the cold spray process, a compressed gas enters a convergent divergent nozzle to attain supersonic velocity at the exit as shown in Figure.1.1. Solid powder particles are then injected into either the convergent or divergent section of the nozzle and accelerated by the expanding gas. To achieve higher velocity, the gas is often preheated in the chamber to temperatures as high as 900 K. It is widely believed that given sufficient kinetic energy, the particles will deform upon collision and bond to the substrate. The exact physical mechanisms by which the particles deform and bond is an area of ongoing research (Jodoin *et al.* (2006), Klinkov *et al.* (2005)).

The most common method of achieving supersonic gas flow is to pass the gas through

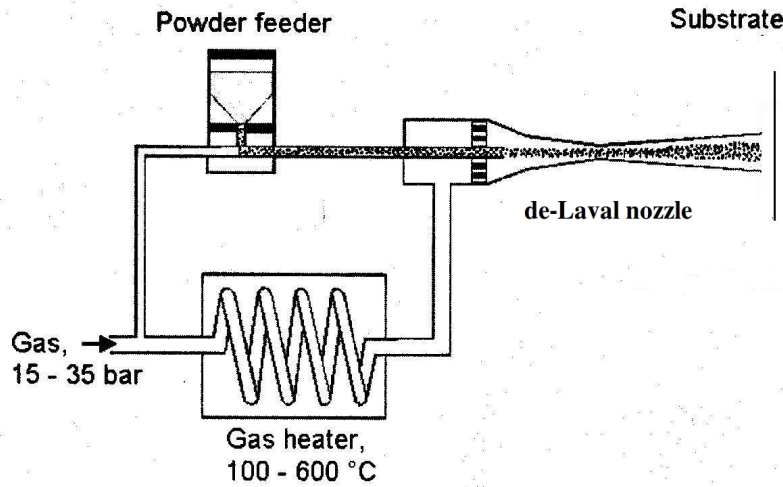


FIGURE 1.1: Schematic representation of the cold spray process. Adapted from Davis (2004).

a de-Laval nozzle which is operating in either the underexpanded or overexpanded flow regime. The left hand side of Fig.1.2 shows the pressure variation through a de-Laval nozzle as the chamber pressure (P_0) is increased relative to the back (P_b) or ambient pressure (P_a). In curves *a* and *b*, the chamber pressure is not high enough to induce sonic conditions at the throat and the flow is subsonic throughout the nozzle. In curve *c* the throat becomes sonic and the flow is said to be choked - no additional mass can be added. In this case, the flow decelerates to subsonic speeds in the divergent section of the nozzle. As the chamber pressure is further increased, the flow reaches supersonic speeds in the diverging section and remains choked. A normal shock may be present in the diverging section to adjust the nozzle exit conditions to ambient conditions as represented in curves *d* and *e*. The shock moves downstream with increasing chamber pressure. Eventually the normal shock reaches the nozzle exit as shown in curve *f*. Beyond this point, three flow regimes are possible depending on magnitude of the pressure at the nozzle exit (P_e) relative to the ambient. Curve *h* represents an ideally expanded nozzle in which the pressure at the exit matches that of the ambient. Curves *g* and *i* represent an overexpanded ($P_e < P_b$) and underexpanded nozzle ($P_e > P_b$) respectively. As there is no shock at the exit to adjust the pressure to ambient conditions, the flow compresses and expands in a series of compression waves and expansion waves until it matches the ambient flow conditions (Donaldson & Snedeker (1971)). The bottom of Fig.1.2 shows the pressure variation through a convergent nozzle commonly employed

TABLE 1.1: Cold spray nozzle operating conditions

Reference	$P_0(MPa)$	A_e/A_t	Ma	$Casef(KPa)$	$Caseg(kPa)$
Jen <i>et al.</i> (2005)	2.0	28.4	5.19	3.03	94.8
Stoltenhoff <i>et al.</i> (2002)	2.0	9.0	3.85	20.2	345
Samareh & Dolatabadi (2007)	0.62	9.0	2.19	59.3	321
Katanoda <i>et al.</i> (2007)	3.0	12.3	4.19	15.3	312

in a variant of cold spray called kinetic metallization. As the chamber pressure is increased, the flow becomes choked at the nozzle throat as shown in curve *c*. Upon further increases, the nozzle becomes underexpanded with sonic conditions at the exit as seen in curves *d* and *e*.

To achieve a supersonic nozzle required for cold spraying, it must operate in either the underexpanded or overexpanded flow regime. An ideally expanded nozzle is uncommon as it is highly unlikely for the pressure at the nozzle exit to be exactly the same as the ambient. To characterise the nozzles used in previous cold spray simulations, it is necessary to calculate the pressure at the nozzle exit. The exit pressure assuming an ideally expanded nozzle (*h*) is listed in Table.3.1 for several cold spraying conditions. This is calculated using the one dimensional isentropic relations White (1999). The pressure following a normal shock at the nozzle exit is also given as case *f*. In most cold spray applications, the ambient pressure (101.3 kPa) falls between cases *f* and *h* which implies the nozzle is overexpanded. In the case of Jen *et al.* (2005), there should be a shock near the nozzle exit. However the assumptions used in the calculation (see Section.3.1.1 for detail) may carry enough uncertainty error for it to be just overexpanded. It is fortunate that overexpanded nozzles have been used instead of underexpanded nozzles because a lower chamber pressure is required to produce the same supersonic exit conditions. The difference between the two nozzles occurs outside the nozzle in the jet shock structure as discussed later in Section.1.3.

The first attempt at modeling the gas and particle dynamics through a cold spray nozzle assumed a quasi one dimensional isentropic gas flow (Dykhuizen & Smith (1998)). The particle velocity was determined by solving the drag acting around a sphere.

$$F_D = m_p \frac{du_p}{dt} = \frac{1}{2} \rho C_D (u - u_p) |u - u_p| A_p \quad (1.1)$$

Under the assumption of constant gas velocity, density and drag coefficient, the above equation can be rearranged and integrated by parts to yield

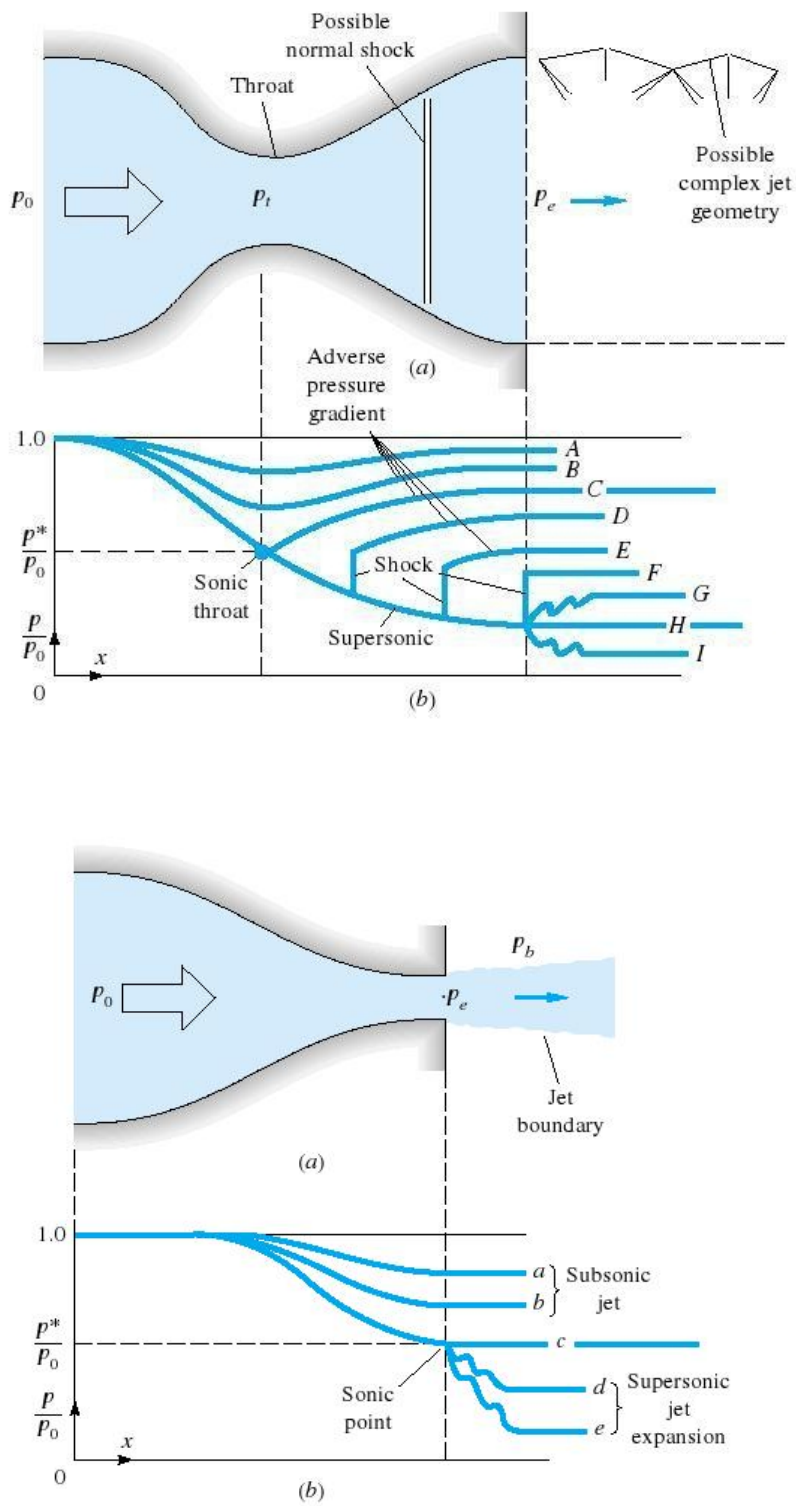


FIGURE 1.2: Flow regimes through a convergent divergent (de-Laval) nozzle (top) and a convergent nozzle (bottom). White (1999)

$$\begin{aligned}
m_p \frac{du_p}{dx} \frac{dx}{dt} &= \frac{1}{2} \rho C_D (u - u_p) |u - u_p| A_p \\
\int_0^u m_p \times u_p \times du_p &= \int_0^x \frac{1}{2} \rho C_D (u - u_p) |u - u_p| A_p dx \\
\log\left(\frac{u \times u_p}{u}\right) + \frac{u}{u \times u_p} &= \frac{C_D A_p \rho x}{2m_p}
\end{aligned} \tag{1.2}$$

In cases where the particle velocity is very small in comparison to that of the gas, Dykhuizen & Smith (1998) showed that Equation.1.2 may be simplified even further to

$$u_p = u \sqrt{\frac{C_D A_p \rho x}{m_p}} = u \sqrt{\frac{3C_D \rho x}{d_p \rho_p}} \tag{1.3}$$

By analysing the terms in the above equations, the authors noted that higher particle velocities could be achieved by increasing the nozzle chamber pressure, temperature and overall length while reducing the particle size. Clearly then, the maximum particle velocity is limited by the pressure and temperature that can be withstood by the nozzle chamber without damaging it. The accuracy of this model was later assessed in several experimental studies (Phani *et al.* (2008), Jodoin *et al.* (2006) and Wu *et al.* (2005)) using commercial high speed optic diagnostics and shown to be agreeable.

An important theoretical study on the cold spray nozzle gas and particle dynamics (Grujicic *et al.* (2003)) demonstrated a numerical technique for optimising the contour profile of the nozzle divergent section to produce maximum particle acceleration. This is achieved by maximising the the particle acceleration at each axial location via an iterative solution. It was shown that Helium is a more efficient though expensive carrier gas than air due to its monatomic character and lower molecular weight. In a later paper, the authors (Grujicic *et al.* (2004)) derived an empirical function which relates the gas velocity at the nozzle exit to the nozzle expansion ratio and chamber conditions. Analytical solutions for the nozzle exit particle velocity in the limit of very short and long nozzles were combined to produce an expression for intermediate nozzle lengths.

Alkhimov & Kosarev (2003) was one of the first to study the growth of the boundary layer in the diverging section of a cold spray nozzle. In order for the particles to catch up to the gas velocity, it is desirable to increase the nozzle length. However, the thickening of the boundary layer that comes with this would decrease the effective nozzle cross sectional area downstream. Using boundary layer theory, the authors found that for nozzles with a diameter to length ratio (D/L) of less than 0.02, the average Mach

number at the nozzle exit is significantly lower than the theoretical isentropic value. This is due to the fact that the boundary layer has merged along the nozzle centerline, giving rise to the self-similar $1/7$ velocity distribution law.

The flow between the nozzle exit and substrate has been modelled using the commercial software package FLUENT, albeit with limited experimental validation (Kosarev *et al.* (2003), Katanoda *et al.* (2007), Samareh & Dolatabadi (2007)). These simulations have been parametric studies examining the effects of the nozzle chamber pressure, temperature, geometry and standoff distance on the particle impact velocity. For long nozzles with heavy particles, the particles appeared to be relatively unaffected by the bow shock within the supersonic impinging jet. Recent studies (Jodoin *et al.* (2006), Fukanuma *et al.* (2006), Li *et al.* (2006)) have started using a commercial high speed CCD camera system (SprayWatch 2i, Oseir Ltd, Finland) to measure the particle velocity and compare them with CFD simulations. Once the particle impact information (i.e. impact speed) is given, it can be used as the input data for modelling the particle impact phenomena. This technique allows an estimation of the particle deposition efficiency and an understanding of the interfacial bonding phenomena for various combinations of particle and substrate materials (see Figure.1.3).

It is clear from these studies that the emphasis of cold spray modeling has been on optimisation of the process in regards to increasing the impact velocity. To obtain a better understanding of the particle-laden supersonic impinging jet underlying the cold spray process, one needs to consult the fluid mechanics literature. There exists an extensive body of literature on flow through supersonic nozzles and the jets issuing from them due its widespread application in the aeronautical industry. The following sections are an attempt to extract and summarise the information most relevant to cold spray fluid dynamics and in doing so place the current research in context.

1.2 Flow through nozzles

The flow regimes depicted in Figure.1.2 assume an isentropic gas flow and ignore viscous effects such as the boundary layer along the wall. The occurrence of flow separation in supersonic nozzles has received considerable attention in the fluids literature because it generates unsteady and asymmetrical shock loads which can damage the internal structure of the nozzle. However, it also holds potential applications in mixing enhancement due to the large instability associated with supersonic flow separation (Papamoschou

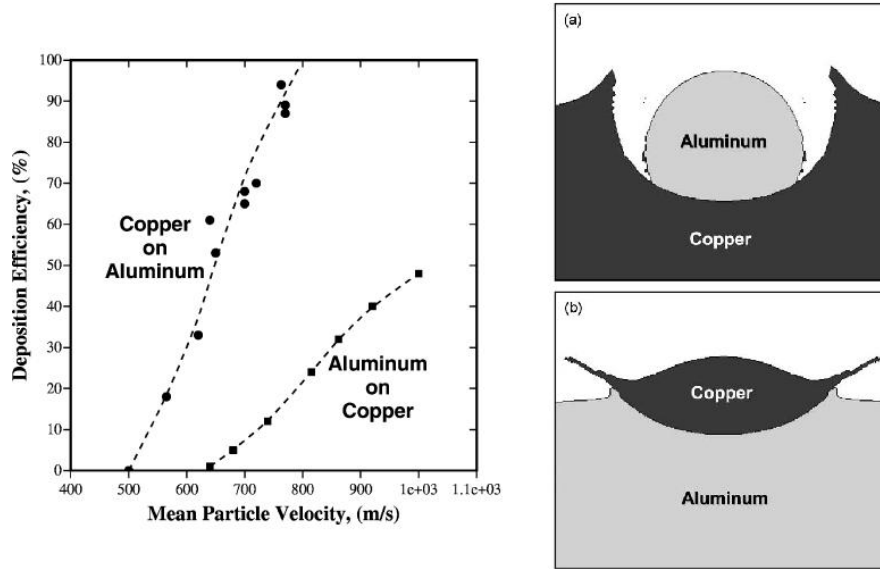


FIGURE 1.3: (Left) Deposition efficiency for the cold spraying of Copper on Aluminium and vice versa. (Right) Deformation of the particle and substrate at 50 nsec following particle impact at speeds of (a) 400 m/s and (b) 500m/s. Reprinted with permission from Grujicic *et al.* (2003).

(2000), Papamoschou (2001) and Papamoschou (2004)). The occurrence of flow separation in nozzles is dictated by the nozzle divergence angle and the presence of a normal shock in the diverging section. The adverse pressure gradient along the wall of a subsonic nozzle with large divergence angle may be sufficient to induce reverse flow. Otherwise, if the nozzle is operating in the flow regime indicated by curves *d* and *e* in Figure.1.2, the shock in the divergent section of the nozzle may detach from the wall as a result of the pressure recovery across the shock to form a lambda shaped shock structure.

A review of the literature dealing with the prediction of the onset of flow separation in subsonic nozzles with large divergence angles was compiled by Morrisette & Golberg (1978). It was noted that zero pressure gradient separation predictors like the method of Reshotko & Tucker (1955) gave reasonable predictions for nozzles with turbulent separation. The ratio of the pressure at point of flow separation relative to the ambient pressure decreased with increasing Mach number M_{sep} and is $P_{sep}/P_a \simeq 0.5$ for $M_{sep} \sim 2$ and $P_{sep}/P_a \simeq 0.3$ for $M_{a_{sep}} \sim 4$. Nozzles with laminar flow separation exhibited higher separation pressure ratios. For nozzles with local wall angles (such as conical and contoured nozzles), the observed separation deviated from those of predictor methods. Flow separation does not occur in underexpanded and overexpanded supersonic nozzles as the pressure gradient along the divergent section is always favorable as seen in

Figure.1.2.

A schematic representation Figure.1.4 clearly shows the main features of a symmetrical and asymmetrical lambda shock structure in nozzles with a strong standing shock in the divergent section (see Figure.1.2 curves *d* and *e*). Each lambda foot is characterised by the incident shock $C1$ and $C3$, the reflected shocks $C2$ and $C4$ and the triple points $T1$ and $T2$ where the incident and reflected shocks merge to form to the standing shock $N1$ also referred to as the Mach disk. The slip lines $L1$ and $L2$ originates from each triple point and the fluid bounded by them is recompressed back to the ambient pressure. Further downstream from the Mach disk, the incident shocks are reflected between the detached boundary layers and the slip lines to form secondary shocks $C2$ and $C4$. These oblique shocks are confined between the slip line and the detached mixing layers until the mixing layer merges with the slipstream.

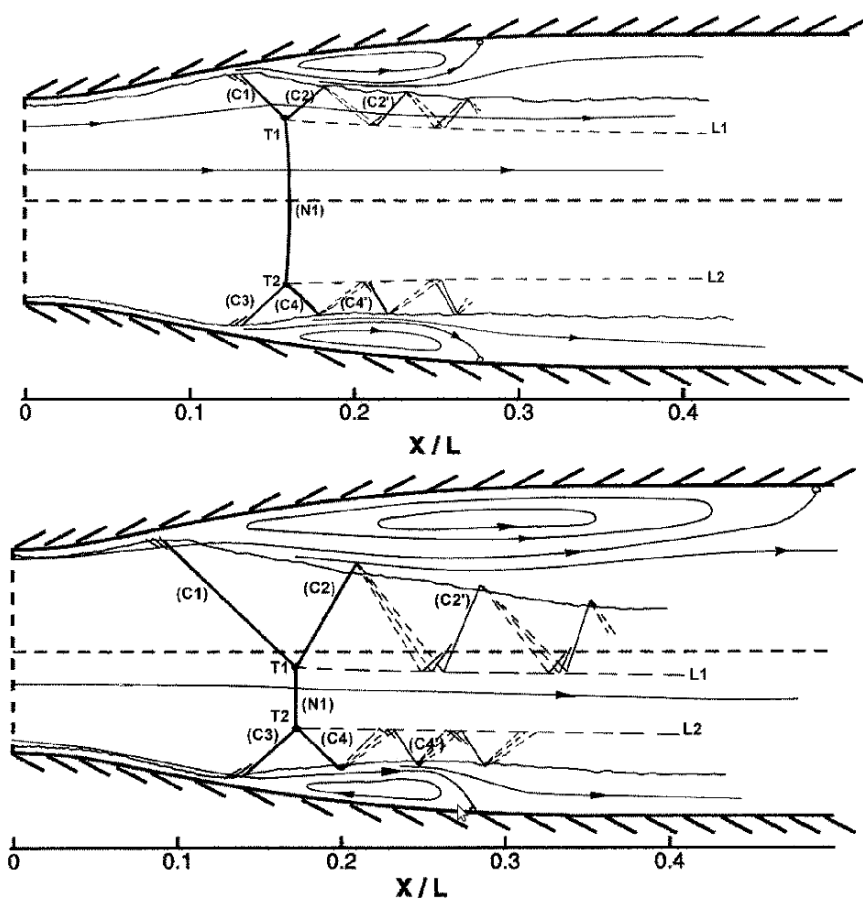


FIGURE 1.4: Schematic representation of shock induced flow separation in nozzles with symmetric (top) and asymmetric (bottom) lambda structures. Reprinted with permission from Bourgoing & Reijasse (2005)

Papamoschou (2004) performed an extensive study on shock induced flow separation inside a rectangular supersonic nozzle using spark schlieren photography. The instantaneous flow visualisations are shown in Figure.1.5. A well defined 'lambda' structure can be observed along the walls and can be either symmetrical and asymmetrical for different test runs. The shock structure chooses its orientation at the start of the test run and remains the same for the remainder of the run. The separated shear layer downstream of the large lambda foot displayed strong instabilities while that of the smaller lambda foot was more stable. Very large eddies, sometimes occupying more than half the nozzle height, were shed from the large lambda foot. The Mach disk occurred at a smaller expansion ratio than that predicted by isentropic theory. In the theory, the flow is assumed to remain attached after passing through the shock and compresses isentropically to the ambient pressure. In reality, the viscous flow becomes detached along the wall and expands non-isentropically downstream. Hence the back pressure felt by the shock is substantially larger in the experiment than in the theoretical prediction and this pushes the shock upstream towards the throat.

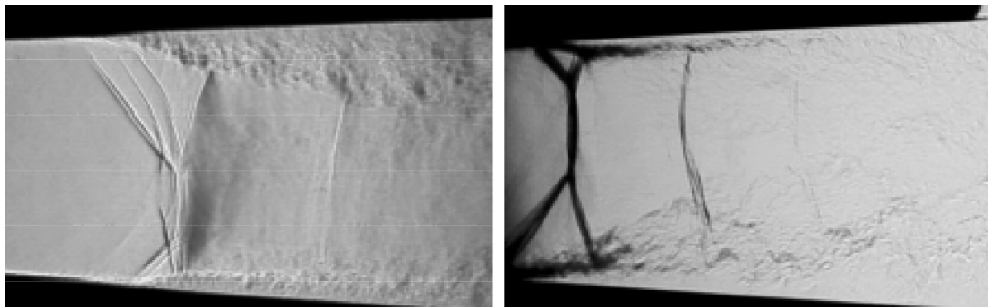


FIGURE 1.5: Instantaneous schlieren flow visualisation of flow through a planar nozzle with area (A_e/A_t) and pressure (P_e/P_a) ratios of 1.5 respectively. The two images were taken using different illumination settings and field of view. Reprinted with permission from Papamoschou (2004)

Numerical studies by Wilmoth & Leavitt (1987) and Hamed & Vogiatzis (1997) assessed the accuracy of turbulence models in predicting the nozzle flow and thrust performance. The simulations reproduced the basic structure of the lambda shock structure and the thrust predictions were in good agreement with experimental measurements except in cases with flow separation. A combined experimental and numerical paper by Hunter (1998) revealed two flow separation regimes for a nozzle with an expansion ratio of 1.8. Three dimensional separation with partial reattachment was observed for pressure ratios (P_e/P_a) smaller than 1.8 and fully-detached two dimensional separation

was noted for pressure ratios greater than 2. The author believed that the transition was brought about by the tendency of the overexpanded flow to detach and reach a stable thermodynamic equilibrium.

Other studies have focused on the aeroacoustics associated with supersonic nozzle flow separation such as in the paper by Zaman *et al.* (2002). Zaman observed that the phenomena occurred often but not always in nozzles operating at low pressure ratios and was characterised by strong acoustic tones and harmonics. The study attributed the tone generation to the unsteadiness of the shock structure and demonstrated that the frequencies scaled with the distance between the lambda foot and the nozzle exit. The author also noted that tripping the nozzle boundary layer helped to suppress the tone. Some attention has also been paid to the duration of the nozzle starting process. An inviscid numerical investigation by Mouronval *et al.* (2002) simulated the start up process by passing a moving planar shock through the nozzle. It was shown that by decreasing the nozzle divergence angle and the shock speed, the starting process was comparatively shorter.

1.3 Supersonic free jets

Before discussing the supersonic impinging jets commonly found in cold spray and other aeronautical applications, it is necessary to first review the free jet. This section describes the jet flow field produced by an underexpanded and overexpanded nozzle. The general structure of an underexpanded free jet issuing from a convergent nozzle is well established. A jet is said to be underexpanded when the pressure at the nozzle exit is greater than that of the ambient and vice versa for an overexpanded jet.

A schematic representation of the mean flow field proposed by Donaldson & Snedeker (1971) is shown in Figure.1.6. The subsonic jet is characterised by a potential core surrounded by a mixing region between the jet and ambient fluid. Several nozzle diameters downstream, the mixing region penetrates inward to reach the jet centerline and the core completely dissipates. Beyond this point, the mixing region continues to spread as the velocity w decays at a rate required to conserve axial momentum. In the fully developed region of the jet, the mean velocity profiles approach self-similarity such that $w/w_{c/2} = f(r/r_s)$

As the nozzle exit approaches sonic conditions, a weak normal shock is formed. This shock changes rapidly with increasing pressure ratio which can be defined as either as

the ratio of the throat to ambient pressure (PR) or the chamber to ambient pressure (NPR). The boundaries of the jet core is determined by the requirement of pressure equilibrium between the outer portion of the flow within the shock structure and the surrounding ambient air. The physical mechanisms for achieving this involve a series of expansion and compression waves. At $PR = 1.1$, the familiar ‘shock diamonds’ pattern composed of intersecting expansion and compression waves is established in each shock cell and can be observed until a pressure ratio of $PR = 2$; this flow regime is described as being *moderately underexpanded*. The inward diffusion of the mixing region continues and ultimately results in the dissipation of the core. Downstream from the core where the jet has become subsonic, the spread and decay characteristics is expected to be similar to that of a fully subsonic jet.

Above a pressure ratio of about $PR = 2.0$, the shock structure in the initial shock cell begins to change. Along the jet centerline where the expansion is maximum, the pressure becomes so low relative to the ambient pressure that the required compression takes place across a normal shock also referred to as the Mach disk. Once the disk is formed, the jet is said to be *highly underexpanded*. Most of the research dealing with this flow regime have examined the near field shock structure with particular attention given to the size and location of the Mach disk. Addy (1981) has shown that the nozzle geometry doesn’t affect the distance between the Mach disk and nozzle exit but had some influence on its diameter. Cumber *et al.* (1995) collated the experimental data of various researchers and found that the Mach distance correlates very well with the pressure ratio whereas the diameters correlates poorly. At very high pressure ratios $NPR > 4$, the first cell shock structure dominates over a long distance and no Mach disks are present in the subsequent cells (Octobe *et al.* (2008)). The radial diffusion in the mixing region surrounding the jet core is minimum and this gave rise to a longer core length.

Much attention has also been given to the symmetric and helical large scale structures which occur in the jet shear layer as a result of instabilities. Novopashin & Perepelkin (1989) used Rayleigh scattering to generate density contours maps of highly underexpanded jets. He observed an axisymmetric structure which he subsequently referred to as a ‘petal’ structure. As the nozzle is rotated, it results in an equivalent rotation of the lobes. From this, the authors deduced that the structure was likely to be a consequence of stationary streamwise vortices. Krothapalli *et al.* (1991) confirmed

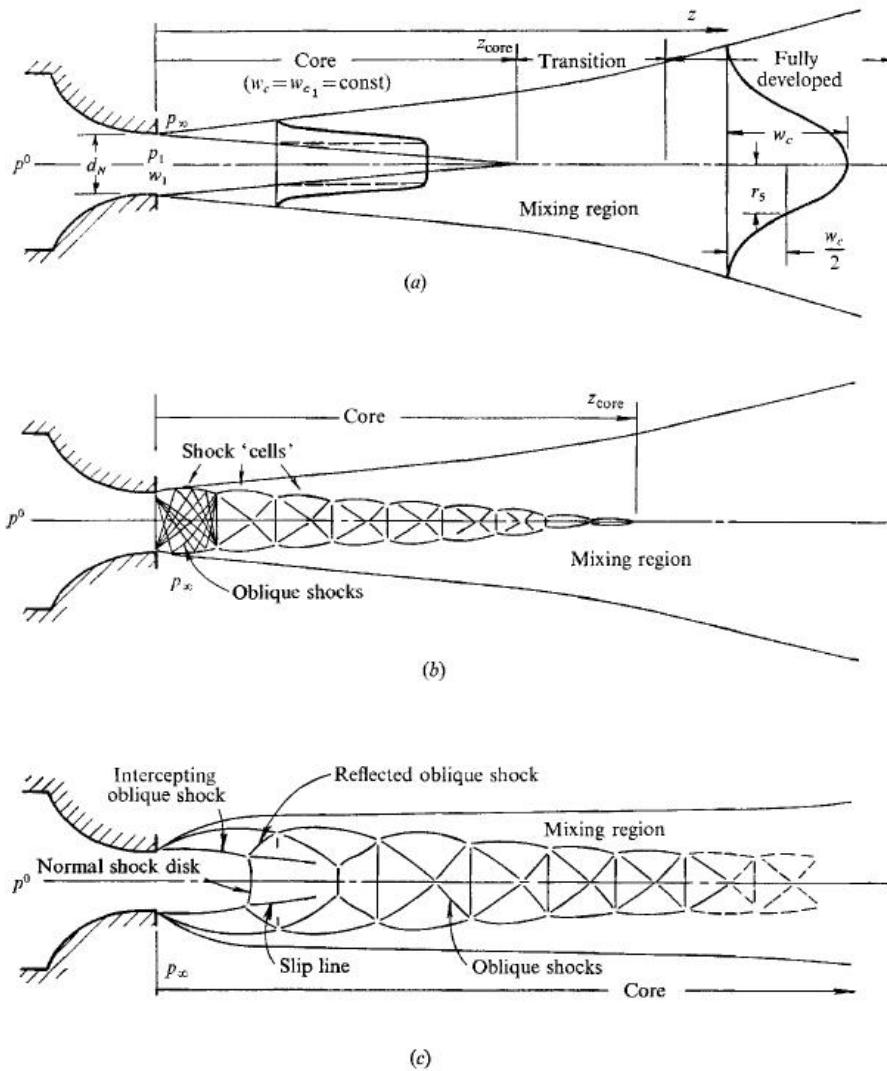


FIGURE 1.6: Schematic representation of a (a) subsonic jet (b) moderately underexpanded jet and (c) highly underexpanded jet taken from Donaldson & Snedeker (1971). Reprinted with permission from the Journal of Fluid mechanics.

the existence of streamwise vortices by taking pressure measurements around the jet circumference. The sinusoidal variation suggests the presence of streamwise vortices of significant strength. Flow visualisations were also obtained using condensed water particles formed by the process of vapor in the ambient air being entrained and mixed into the cold supersonic jet. The strong indentations in the shear layer marked by these condensed water particles again support the presence of streamwise vortices.

Underexpanded dual coaxial jets have been investigated in order to improve the mixing efficiency of two gas streams. Gutmark *et al.* (1991) investigated the effect of introducing a secondary annular jet around the primary jet and reported a considerable

increase in the shear layer growth. Masuda & Moriyama (1994) later showed that the presence of a secondary jet reduces the diameter of the Mach disk formed in the primary jet. Buckley (1975) argued that the location of this Mach disk is unaffected by the secondary jet because the axial variation of the Mach number is independent of external conditions. However, Narayanan & Domodaran (1993) contradicted Buckley's statement by stating that the presence of the secondary jet significantly changes the Mach number variation upstream of the Mach disk. Further study have been promised by both authors in order to resolve this contradiction. A recent study by Lee *et al.* (2004) imposed swirling jets on top of the underexpanded dual coaxial jets. The results indicate that the swirl causes the Mach disk to move downstream with an increase in diameter.

Very little research had been performed on overexpanded free jets until recently. A numerical study by Hadjadj *et al.* (2004) revealed the similarity in shock structure between an overexpanded free jet and supersonic flow between symmetric wedges. A schematic representation of both flowfields is shown in Figure.1.7. The incident shock (*IS*) is reflected as either a regular reflection (*RR*) or as a Mach reflection (*MR*) depending on the flow speed and pressure ratio across the nozzle exit. In the case of a Mach reflection, a Mach disk is formed between the two incident shocks where as for a regular reflection the incident shocks intersect one another. Previous research on supersonic flow through wedges have shown that the transition criteria between a regular and Mach reflection is accompanied by hysteresis. In other words, as the angle of the incident shock relative to the freestream (α) varies, the transition from a regular to Mach reflection and back is observed at different angles. The experimental verification of the hysteresis process associated with supersonic flow between symmetric wedges is complicated by the influence of freestream disturbances. Nevertheless it is possible to obtain transition angles close to the theoretical values in a low noise wind tunnels (Ivanov *et al.* (2003)).

Hadjadj *et al.* (2004) also simulated the hysteresis effect in overexpanded planar nozzles by imposing piecewise changes on the incident shock angle through variation of the pressure ratio. The observed transition criteria is similar to that of flow past symmetric wedges and is surmised in Figure.1.8. The regular and Mach reflections occurs above and below the detachment and von Neumann curve respectively. Between the two curves, at a Mach number of greater than 2 exists a dual solution domain where

both configurations are possible. If the incident shock angle is increasing within this domain, the RR configuration is formed otherwise a MM configuration is formed.

Shimshi *et al.* (2009) performed a numerical study in which the nozzle contour is included in the computational domain. In order to ensure a uniform and parallel flow at the the nozzle exit for a given pressure ratio and Mach number, the method of characteristics was employed in the design of the nozzle contour. However, flow separation is still observed in the divergent section of the nozzle for low pressure ratios. The separation point moves upstream as the pressure ratio increases and this had the effect of shifting the shock structure back into the nozzle.

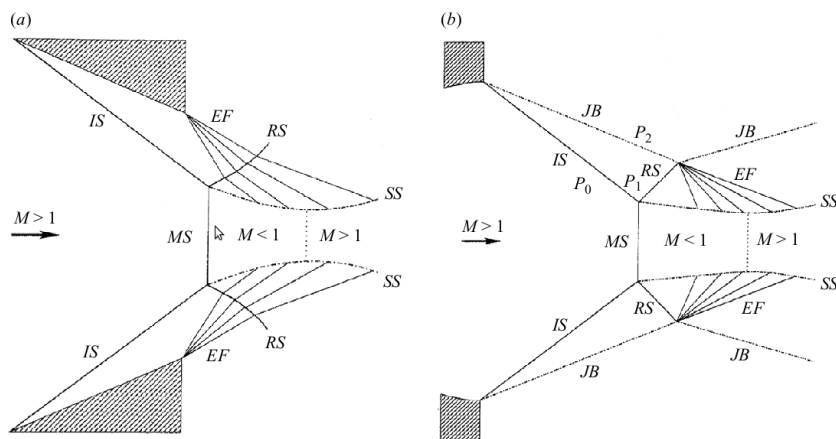


FIGURE 1.7: Schematic representation of (a) flow between symmetric wedges and (b) flow at the exit of an overexpanded planar nozzle. Figure nomenclature: incident shock (IS), reflected shock (RS), Mach disk (MS), expansion fan (EF), slip stream (SS) and jet boundary (JB). Reprinted with permission from Hadjadj *et al.* (2004).

1.4 Supersonic impinging jets

An understanding of supersonic impinging jets is important given its application in both the cold spray technology and various aeronautical applications. It has been observed that the ground induced effects associated with Vertical Take Off and Landing (VTOL) aircrafts can result in a significant lift loss during the hovering mode. The unsteady pressure fields associated with the supersonic impinging jets are dominated by discrete tones which could match the resonant frequencies of aircraft components and cause severe fatigue problems. The presence of a plate shock in the supersonic impinging jet during the cold spray process is widely believed to be responsible for reducing the particle impact velocity.

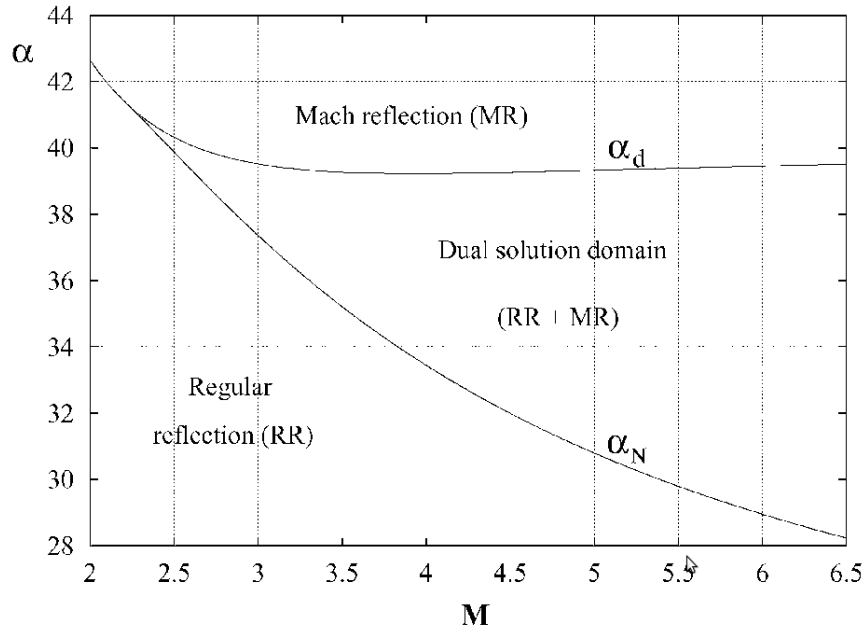


FIGURE 1.8: Theoretical transition criteria between regular (RR) and Mach reflection (MR) taken from Hadjadj *et al.* (2004). Reprinted with permission from the American Institute of Aeronautics and Astronautics.

The early studies of underexpanded impinging gas jets were performed using qualitative flow visualisation techniques like schlieren, shadowgraphy and streakline patterns. Using these experimental techniques, the mean qualitative flow features were established. After comparing surface pressure distribution with flow visualisations, researchers proposed the existence of a recirculation bubble whenever an annular pressure peak is observed. Due to the lack of quantitative data available at the time, this hypothesis was debated by some (i.e. Kalghatgi (1976)). During the past decade, the application of Particle Image Velocimetry (PIV) has enabled velocity fields to be extracted and this led to the confirmation of the hypothesis.

A schematic representation of the mean flow field proposed by Alvi & Iyer (1999) is represented in Figure.1.9. The flow field can be divided into three parts: the primary jet region upstream from the plate shock, the impingement region between the plate shock and impingement surface and the wall jet region.

It's should be mentioned at this point that the plate shock is referred to by several names in the material and fluids literature. In the former literature, the terms bow shock and stand off shock are commonly used to describe the strong shock prior to the substrate while in the fluids literature the terms Mach disk, plate shock are applied.

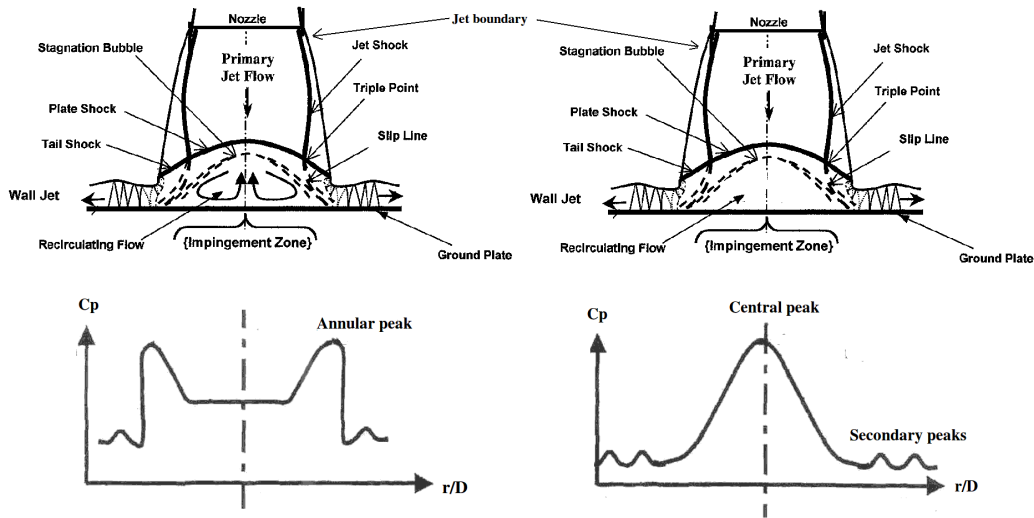


FIGURE 1.9: Schematic representation of underexpanded impinging jet (a) with and (b) without a recirculation bubble. Reprinted with permission from Alvi & Iyer (1999)

The distance between the shock and the plate is called the shock distance whereas the distance between the nozzle exit and the plate is referred to as the standoff distance.

For cases without recirculation bubbles the plate shock is relatively flat and the jet deflects almost perpendicularly along the plate. The surface pressure distribution is characterised by a central peak. The jet shock interacts the plate shock at the triple point (Kalghatgi & Hunt (1975)) to produce a third shock generally referred to as the tail shock. A shear layer known as the slip line emanates from the triple point as a result of the velocity difference between the flow processed by the jet and tail shocks and the flow which travels through the standoff shock. In cases with a recirculation bubble, the impingement of the slip line on the plate surface raises the local pressure sufficiently to cause boundary layer separation. Hence, the extent of the stagnation bubble is defined by a plateau in the surface pressure distribution while the annular pressure peaks correspond to the slip line impingement point. A second weaker shock sometimes referred to as a contact wave is often observed between the plate shock and the impingement plate. The wall jet consists of an alternating series of expansion and compression regions (Carling & Hunt (1974)). It should be noted that the shock nomenclature of a supersonic impinging jet varies between authors. For consistency, the jet shock and plate shock from here on will be referred to as the inner shock and Mach disk respectively.

The occurrence of unsteady shock motion in an underexpanded impinging jet has

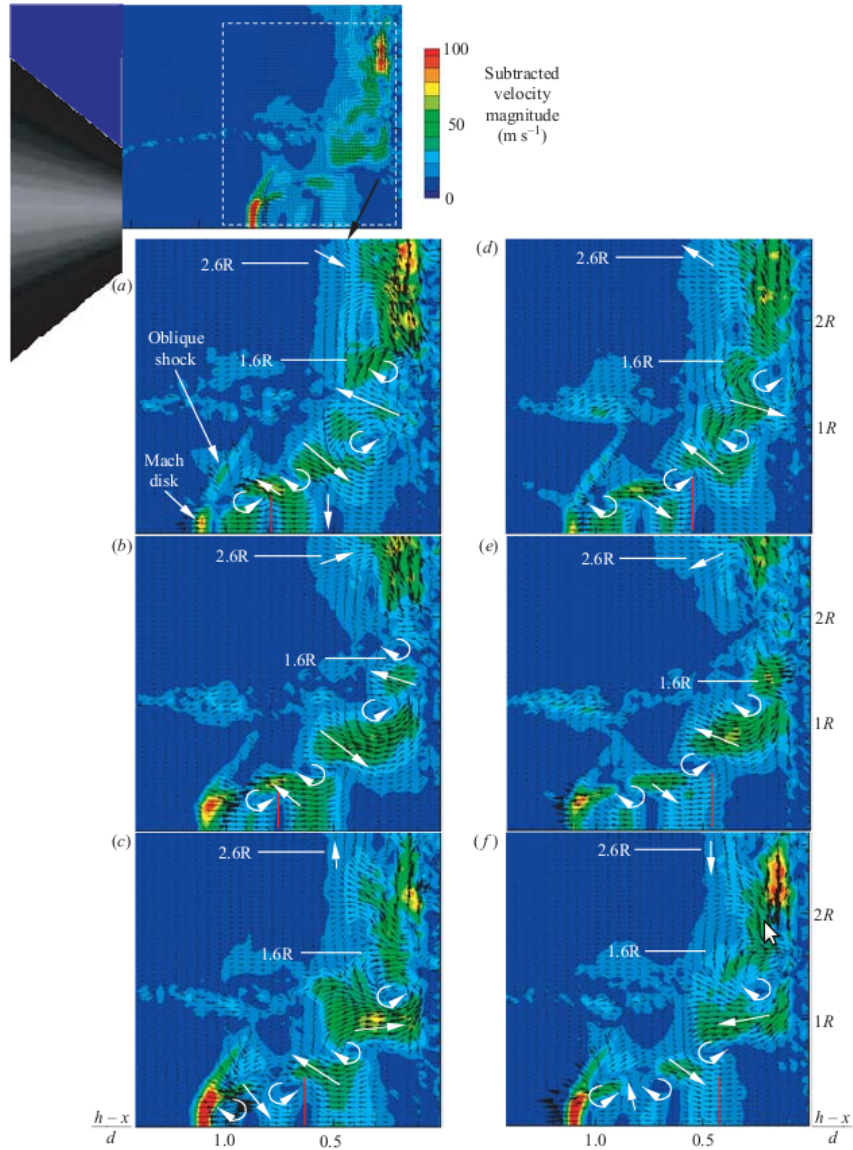


FIGURE 1.10: Phase locked vector fields of an underexpanded impinging jet operating at $NPR = 4.03$, $Ma_e = 1.0$, $s/D = 2.08$. Reprinted with permission from Henderson *et al.* (2005)

been frequently reported in the literature but the features vary depending on the operating conditions. To obtain high spatial resolution velocity measurement of the flowfield, a novel PIV processing algorithm was developed by Lourenco & Krothapalli (1998). Although particle lag is inevitable in regions with very high velocity gradients such as shocks, Krothapalli *et al.* (1999) demonstrated that the algorithm is capable of capturing the large scale structures in the primary and wall jet region. Henderson *et al.* (2005) later obtained phase averaged PIV measurement as shown in Figure.1.10. Two pairs of counter rotating vortices are distributed along the jet boundary which successively

entrain and remove fluid as indicated by the direction of the arrows. These vortices collapse in the wall jet at a radius of $1.6R$ from the jet centerline and this location is the equivalent of a saddle point. The direction of the vortices are reversed during each cycle of oscillation while the velocity vector at $2.6R$ rotates in the counter clockwise direction.

Figure.1.11 shows the variation in the shock structure as the pressure ratio and impingement distance is changed (Risborg & Soria (2008)). At an impingement distance of $s/D = 1.5$, a Mach disk followed by the contact wave is observed as the pressure ratios increases from $PR = 1.6$ to 1.8 . Despite both pressure ratios being in the moderately underexpanded flow regime, the decrease in pressure over such a short distance can only be compensated through a Mach disk. As the impingement distance increases to $s/D = 2.0, 2.5$ for $PR = 1.6, 1.8$, the shock structure in the first shock cell gradually resembles that of a moderately underexpanded free jet. A second shock diamond is faintly visible at $s/D = 2.5$ and $PR = 1.6$ while a Mach disk appears in the second shock cell for a higher pressure ratio of $PR = 1.8$. A Mach disk is always present in the first and second shock cells for a pressure ratio of $PR = 2.1$.

High-speed phase averaged measurements of an underexpanded impinging jet were also acquired by the same author. The conditions are similar to those used in Henderson *et al.* (2005) at $PR = 2.1$, $Ma_e = 1.0$, $s/D = 2.0$. The shadowgraphs were averaged over four periods of oscillation whereas Henderson's PIV images were averaged over two cycles. In Figure.1.12, Risborg & Soria (2008) identified the mode of oscillation as being a helical instability. The contact wave appears to rotate in an helical manner while the Mach disk remains relatively stationary. The contact wave tilts by as much as 20° relative to the plate while rotating about the jet centerline over a period of $36\mu s$. Using an edge detection algorithm, the shock distance is found to vary between $1.03D$ to $1.09D$ which constituted a 6% deviation from the mean. Several modes of instability have been identified for varying degrees of underexpansion and different standoff distances and further study will be undertaken to characterise the transition between different modes.

A linear stability model was developed by Kuo & Dowling (1996) to provide insight into the self excited oscillations that occur in moderately underexpanded impinging jets. Using the jet centerline velocity, a characteristic equation is derived for the eigen-frequencies of the Mach disk oscillation. Two families of isolated roots are calculated

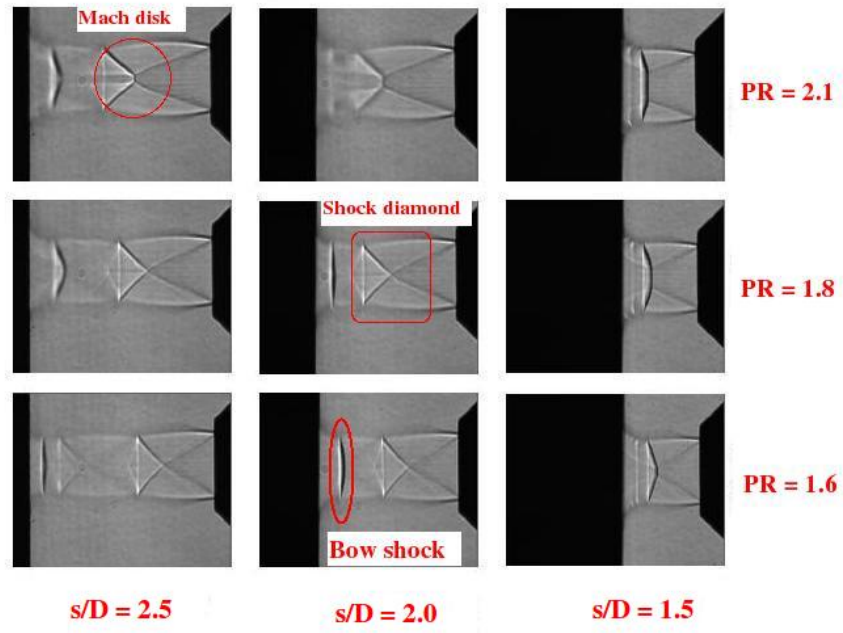


FIGURE 1.11: Averaged shadowgraphs of underexpanded impinging jets operating at different pressure ratios and standoff distances. Reprinted with permission from Risborg & Soria (2008)

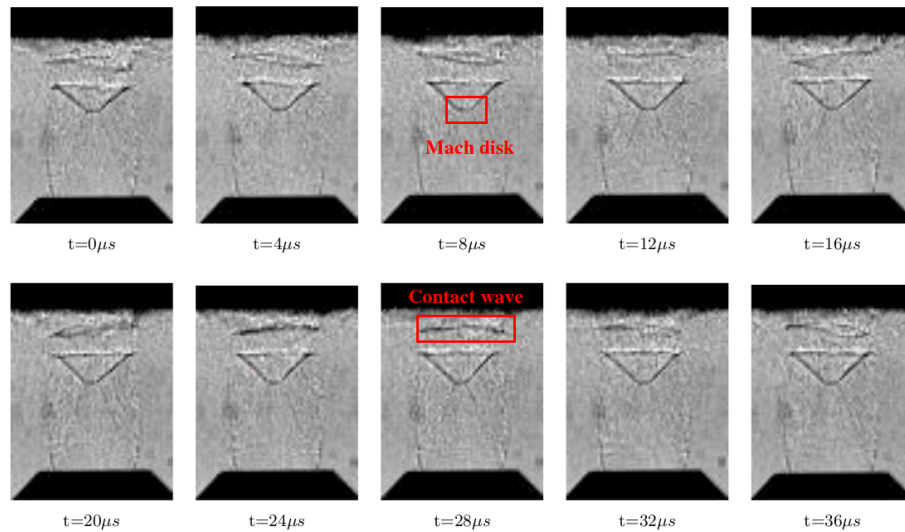


FIGURE 1.12: Phase-averaged shadowgraphs of an underexpanded impinging jet operating at $NPR = 4.0$, $Ma_e = 1.0$, $s/D = 2.0$. Reprinted with permission from Risborg & Soria (2008)

with the lowest frequency mode being the least stable. The threshold at which this mode becomes unstable is a function of the standoff distance and shock distance. The frequencies and damping rates of the oscillation modes are determined from the roots of the characteristic equation and found to match well with the numerical simulation.

Several studies have shown that the sound production mechanism in supersonic impinging jets is highly dependent on the size of the impingement plate. Small plate impinging tones usually occur for plate diameters less than or equal to two nozzle diameters. Henderson & Powell (1993) proposed that the primary tones are produced by periodic changes in the jet diameter and large oscillations of the shocks upstream of the plate shock. The secondary tones resulted from the interaction of the disturbances with the plate shock and waves in the near wall jet region. The production of tones for large impingement plates was found to be strongly dependent on the standoff distance and to a lesser extent the degree of underexpansion (Henderson & Powell (1996)). Tones produced at small to moderate standoff distances originated in the impingement region while tones produced at very short standoff distances originated in the near wall jet region and may be associated with vortices along the wall jet. Discrete impingement tones have even been detected for ideally expanded jets (Krothapalli *et al.* (1999)) despite their having a very weak shock structure.

There has been considerably less research into supersonic jets issued from a convergent-divergent nozzle. A study by Alvi & Iyer (1999) examined an ideally expanded and underexpanded impinging jet issued from a de-Laval nozzle. The data showed that for an ideally expanded jet, the impingement region is free of a recirculation zone and exhibits a centrally peaking surface pressure distribution. In contrast, the underexpanded jet has a recirculation bubble defined by the distance between the pressure peaks. These features are consistent with those of underexpanded impinging jets issued from a convergent nozzle. Recent PIV measurements of twin underexpanded impinging jets (Elavarasan *et al.* (1999)) show the inner wall jets pushing the flow upwards to form a fountain. Although the fountain could potentially enhance the lift of the VSTOL aircraft hovering near the ground, it could also enter the propulsive system and degrade engine performance. Very few attempts have been made to extract information about overexpanded impinging jets (Ahn *et al.* (2003) and Xu *et al.* (2006)).

A comprehensive validation of the CHEM software for modeling underexpanded impinging jets was carried out by Wu *et al.* (2002). The simulations were compared with schlieren flow visualisation taken by Lamont & Hunt (1980) for a wide range of standoff distances, impingement angles and pressure ratios. Although good agreement was obtained at low impingement angles, the deviation became more pronounced with increasing impingement angle. The maximum pressure along an inclined plate is several

times larger than the perpendicular case and the recirculation bubble has been suppressed. Alvi & Iyer (1999) compared the accuracy of the Spalart-Allmaras rotation curvature turbulence model with the Menter’s shear stress transport turbulence model in simulating moderately underexpanded impinging jets. Both models gave nearly identical results and were in good agreement with the surface pressure measurements. The source of error is believed to have originated from the Boussinesq approximation which was necessary for closure of the Reynolds Averaged Navier Stokes equations. It is believed that the jet impingement gives rise to unequal Reynold stresses in the impingement region and causes the approximation to fail.

1.5 Particle-laden flows

Most literature on particle laden flows deals with particle dispersion in turbulent shear flows which plays an important role in many industrial applications. Typical examples include the dispersion of liquid fuel droplets in gas combustors and the mixing of coal particles by the input jets of coal fired power plants. In many of these processes, the dispersion of particles is a controlling factor of the efficiency and stability of the process. Hence, the primary focus of previous research has been on the prediction of the particle dispersion in turbulent shear flows using either time averaged turbulent properties or by treating the turbulent flow as a random field.

The classic paper by Crowe *et al.* (1985) include a comprehensive set of experiments on the particle dispersion in the turbulent mixing layer of an incompressible free jet. To characterise the degree of particle dispersion, a time scale ratio was defined using the particle aerodynamic response time and a time scale related to the coherent turbulent structures. The aerodynamics response time of a particle is defined as $\tau_A = \frac{\rho_p d_p^2}{18\mu}$ and represents the time required for a particle released from from rest in a uniform flow to reach 63% of the flow velocity assuming Stoke’s drag law. It is effectively a measure of the aerodynamic responsiveness of a particle. The characteristic time scale for the large vortex structures in the mixing layer was defined as $\tau_F = \frac{\delta(x)}{D}$. The ratio of the two time scales is also commonly referred to as the Stokes number.

For $\frac{\tau_A}{\tau_F} \gg 1$, the particles doesn’t have sufficient time to respond to the large vortex structures and travel in a nearly rectilinear path. In this case, the flow spreading rate is larger than the lateral dispersion rate of the particles. For $\frac{\tau_A}{\tau_F} \ll 1$, the particles have sufficient time to respond to the changing velocity field of large eddies and hence

disperse laterally at the spreading rate of the fluid mixing layer. On the other hand, for $\frac{\tau_A}{\tau_F} \sim O(1)$, the large organised vortices are able to temporarily capture the particles and fling them beyond the fluid momentum mixing region, giving rise to a lateral particle dispersion rate larger than the spreading rate of the mixing layer.

Very few studies have investigated the response of particles in compressible flows. Sommerfeld (1994) is one of the few to perform a numerical study of particle-laden highly underexpanded free jets. An Eulerian-Lagrangian approach including two-way momentum and thermal coupling between the gas and particulate phases was employed in the study. The results indicated that the free jet diameter decreased with increasing particle loading as the Mach disk moved closer towards the nozzle exit. The simulated particle velocity using drag coefficients that accounted for rarefaction and compressibility effects Carlson & Høglund (1973) was higher than the Laser Doppler Anemometry (LDA) measurements. It is believed that the supersonic relative velocity between the gas and individual particles generated tiny bow shocks which interacted with those of neighbouring particles.

1.6 Cold spray using shock tubes

One possible way of increasing the particle velocities during the cold spray process is to attach the conventional de-Laval nozzle to the end of a shock tube (Nickel *et al.* (2007) and Luo *et al.* (2009)). The shock tube is a disciplinary tool used in a wide range of fields. In aerodynamic related studies, it is used to study the vibrational and chemical relaxation process in high temperature gases and to generate reservoir conditions for hypersonic shock tunnels. After bursting the shock tube diaphragm, a planar shock is formed in the low pressure region. Because the nozzle entry is smaller in diameter than the shock tube, a portion of the incident shock will be reflected from the entry and the gas in the vicinity be heated as a result of the multiple shock reflections. Once the planar shock reaches the substrate and is reflected to form a bow shock, the particles are injected into the fully supersonic nozzle and the entire spraying process lasts a few milliseconds. A description of the operating principles behind a shock tube is provided next.

A simple shock tube can have either a rectangular or circular cross-section in which a low and high pressure gas is separated using a diaphragm as shown in Figure.1.13 (http://en.wikipedia.org/wiki/Shock_tube). The low-pressure gas is referred to as

the driven gas and the high pressure gas is known as the driver gas. The corresponding sections of the tube are likewise called the driver and driven sections. The bursting diaphragm produces a series of pressure waves, each increasing the speed of sound behind them so that they compress into a shock wave propagating through the driven gas. This shock wave increases the temperature and pressure of the driven gas and induces a flow in the direction of the moving shock. Simultaneously a rarefaction wave, also referred to the Prandtl-Meyer wave, travels back into the driver gas. The interface which separates the driven and driver gases processed by the shock and rarefaction waves respectively is referred to as the contact surface and follows the shock at a lower velocity.

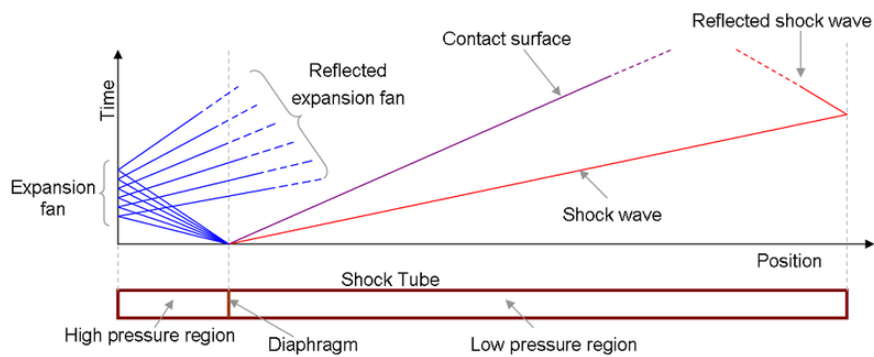


FIGURE 1.13: An idealized shock tube showing the different waves which are formed once the diaphragm is ruptured.

In a real shock tube experiment, the viscous interaction between the boundary layer and the shock reflected from the end walls produces a highly complex flow field known as a bifurcation. Mark (1959) was the first to propose a model for the bifurcation process and a schematic representation of the model is shown in Figure.1.14. Because the low energy boundary layer has a lower stagnation pressure than that behind the reflected shock it cannot pass smoothly into the reflected shock region. Instead, the boundary layer detaches itself from the wall and a region of separated flow is established near the wall. The bifurcated foot and tail shocks merge with the main reflected shock at the triple point similar to the lambda shock structure observed in supersonic nozzle flow separation (see Section.1.2). Due to entropy change from the gas traveling through the bifurcation zone and that which is processed by the single shock system, a slip line is formed. This slip line is unstable and eventually rolls up to form vortices. The gas which encounters the bifurcated foot and tail shocks retain more forward momentum

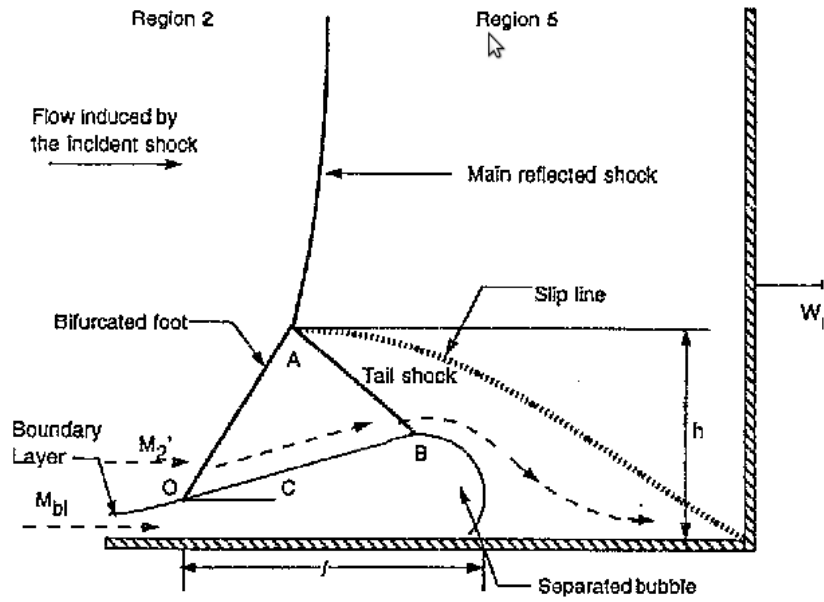


FIGURE 1.14: Schematic representation of the interaction between a reflected shock and boundary layer in a shock tube taken from Weber *et al.* (1995). Reprinted with permission from the American Institute of Physics.

than the gas which is decelerated through the main reflected shock. The result is a jet of fluid feeding into the flow region bounded by the separated boundary layer and the slip line. As the reflected shock structure travels upstream, the boundary layer fluid is continually being entrained and the size of the interaction zone increases.

1.7 Research aim

The first component of the present investigation aims to address several key issues regarding the cold spray nozzle design. It builds upon previous studies by exploring the potential benefits of using a constant diameter barrel section attached to the end of the nozzle for particle acceleration. To make the analysis more realistic, a constant friction has been assumed along the nozzle and barrel section walls. But first, a parametric investigation of the isentropic underexpanded nozzle flow is performed.

The research objectives for the numerical investigation of cold spray nozzles are as follows.

1. To perform a parametric study of the nozzle exit particle velocity using an isentropic underexpanded de-Laval nozzle

2. To solve the governing equations for compressible flow through a duct of varying cross section area
3. To compare the exit particle velocity achieved by acceleration through a constant diameter barrel and diverging section

The gas and particle dynamics between the nozzle and substrate during the steady cold spray process is the focus of study in the second component of the investigation. A numerical approach was chosen for this part of the study due to the difficulties associated with extracting accurate quantitative data from compressible flows (see Lourenco & Krothapalli (1998) and Krothapalli *et al.* (1999)). Previous simulations of the cold spray process have been based on limited validation and are restricted to particle injection in an overexpanded impinging jet. So far, the only way of estimating the change in particle velocity between the nozzle exit and substrate is via numerical simulation. This can be a computationally expensive process given the number of parameters that can be varied. Hence, it would also be desirable to develop a theoretical approach to estimating the particle impact speed and location.

In the present study, an underexpanded and overexpanded nozzle is deployed to accelerate the particles with the operating conditions set to those used in the validation cases. This not only establishes a degree of confidence in the accuracy of the gas phase simulations but also allows a direct comparison between both nozzles with similar exit gas speeds. The particle impact statistics are then extracted to provide information on the particle impact speed, angle and location. Next, the variation in particle velocity and drag during its flight through the supersonic impinging jet is examined. Using this information, a theoretical model is proposed which backed with the relevant experimental data can be used to approximate the particle impact speed.

The research objectives for the numerical investigation of steady cold spray impinging jet flow are as follows.

1. To validate underexpanded and overexpanded impinging jet simulations using existing experimental data
2. To extract the particle impact statistics and dynamics during steady cold spray process
3. To develop and assess a theoretical model for estimating the particle impact speed

The final part of the investigation looks into a novel unsteady cold spray process using a shock tube. As seen from the description given in Section.1.6, the process suffers from a number of disadvantages such as the very limited duration of cold spraying, the need to replace the shock tube after each run and the timing of particle injection to coincide with the passing of the moving shock. Nevertheless, monodisperse particles are injected in the wake of the shock to compare the impact speed produced by steady and unsteady cold spray processes. To simplify the mesh, a circular pipe is used on its own instead of being attached to a nozzle. It was found that this process also offers a mean of studying the shock formation process in underexpanded impinging jets. The shock speed can be selected such that either a shock diamond ($Ma_{sh} = 1.5$) or Mach disk ($Ma_{sh} = 1.8$) is reproduced in the impingement region characteristic of a moderately and highly underexpanded jet.

The research objectives for the numerical investigation of unsteady cold spray impinging jet flow are as follows.

1. To visualise the shock formation process during the unsteady cold spray process and compare its flow features with that of a steady supersonic impinging jet
2. To characterise the particle dynamic response as it travels across a transient shock structure

Chapter 2

Numerical method

This chapter describes the governing equations and numerical schemes used to model the gas and particle dynamics of both steady and transient cold spray processes. A description of the isentropic and non-isentropic theoretical models used to simulate the flow through the nozzle is presented later in Section.3.1. For the gas phase, the axisymmetric Euler equations are solved using an in house total variation diminishing (TVD) version of Roe’s approximate Riemann solver as proposed by Yee (1990). A total variation diminishing HLLC Riemann solver is also employed to compare the accuracy of the two numerical schemes. Section.2.2 discusses the basic principles behind Godunov’s scheme and the critical role played by solution of the Riemann problem. The exact solution is presented in Sections.2.2.1 and 2.2.2 followed by a description of the various approximate solutions in Section.2.3. Due to low particle loading during the cold spraying process, the particle phase is uncoupled from the gas phase and solved using a Lagrangian discrete particle model described in Section.2.4. The initial and boundary conditions as well as the discretisation of the governing equation in both space and time is discussed in Sections.2.5, 2.6, 2.7 and 2.8 respectively.

2.1 Governing equations of fluid motion

In the present study, the conservation form of the non-dimensionalised axisymmetric Euler equations is used to model the supersonic jet. The conservation form of the governing equations is chosen because formulations based on non-conservative variables fail at shock waves giving incorrect shock strength, location and speed. Hou & LeFloch (1994) showed that non-conservative schemes do not converge to the correct solution when flow discontinuities are present in the solution. Previous experimental (Dash *et al.* (1985)) and numerical (Prasad *et al.* (1994)) studies showed that the flow is inviscid

in the near field region of supersonic jets and can be accurately modelled using the Euler equations. According to Grinstein *et al.* (1986), the basic vortex dynamics in a compressible flow shear layer is essentially inviscid. These findings justify the modelling of supersonic jets using the Euler equations.

For reference, the conservation form of the non-dimensionalised (') Navier-Stokes equations in cylindrical coordinates are presented below. The Euler equations are obtained by assuming that the viscous and heat flux terms are zero.

$$\frac{\partial \mathbf{U}'}{\partial t} + \frac{\partial \mathbf{F}'}{\partial z} + \frac{\partial \mathbf{G}'}{\partial r} + \frac{1}{r} \mathbf{S}' - \frac{\partial \mathbf{F}'_v}{\partial z} - \frac{\partial \mathbf{G}'_v}{\partial r} - \frac{1}{r} \mathbf{S}'_v = 0 \quad (2.1)$$

$$\mathbf{U}' = \begin{bmatrix} \rho \\ \rho u \\ \rho v \\ E \end{bmatrix}, \quad \mathbf{F}' = \begin{bmatrix} \rho u \\ \rho u^2 + P \\ \rho uv \\ (E + P)u \end{bmatrix}, \quad \mathbf{G}' = \begin{bmatrix} \rho v \\ \rho uv \\ \rho v^2 + P \\ (E + P)v \end{bmatrix}, \quad \mathbf{S}' = \begin{bmatrix} \rho v \\ \rho uv \\ \rho v^2 \\ (E + P)v \end{bmatrix}$$

$$\mathbf{F}'_v = \begin{bmatrix} 0 \\ \tau_{zz} \\ \tau_{zr} \\ u\tau_{zz} + v\tau_{zr} - q_z \end{bmatrix}, \quad \mathbf{G}'_v = \begin{bmatrix} 0 \\ \tau_{rz} \\ \tau_{zz} \\ u\tau_{zr} + v\tau_{rr} - q_r \end{bmatrix},$$

$$\mathbf{S}'_v = \begin{bmatrix} 0 \\ \tau_{rr} - \tau_{\theta\theta} - \frac{2}{3} \frac{Ma}{Re} \frac{\partial}{\partial z} \left(\mu \frac{v}{r} \right) - \frac{2}{3} r \frac{Ma}{Re} \frac{\partial}{\partial r} \left(\mu \frac{v}{r} \right) \\ u\tau_{zr} + v\tau_{rr} - q_r - \bar{\tau} \end{bmatrix}$$

The viscous stresses and heat fluxes in cylindrical coordinates are given as

$$\begin{aligned} \tau_{zz} &= \frac{2}{3} \frac{Ma}{Re} \mu \left(2 \frac{\partial u}{\partial z} - \frac{\partial v}{\partial r} \right) \\ \tau_{rr} &= \frac{2}{3} \frac{Ma}{Re} \mu \left(-\frac{\partial u}{\partial z} + 2 \frac{\partial v}{\partial r} \right) \\ \tau_{\theta\theta} &= \frac{2}{3} \frac{Ma}{Re} \mu \left(-\frac{\partial u}{\partial z} - \frac{\partial v}{\partial r} + 2 \frac{\partial v}{\partial r} \right) \\ \tau_{zr} &= \tau_{rz} = \frac{Ma}{Re} \mu \left(\frac{\partial u}{\partial r} - \frac{\partial v}{\partial z} \right) \\ \bar{\tau} &= \frac{2}{3} \frac{Ma}{Re} \mu \frac{v^2}{r} + \frac{2}{3} \frac{Ma}{Re} r \frac{\partial}{\partial r} \left(\mu \frac{v^2}{r} \right) + \frac{2}{3} \frac{Ma}{Re} r \left(\mu \frac{uv}{r} \right) \\ q_z &= -\frac{Ma}{Re} \frac{\mu}{Pr(\gamma-1)} \frac{\partial T}{\partial z} \\ q_r &= -\frac{Ma}{Re} \frac{\mu}{Pr(\gamma-1)} \frac{\partial T}{\partial r} \end{aligned} \quad (2.2)$$

The above equations represent the conservation of mass, momentum and total energy during inviscid Newtonian fluid motion. The non-dimensional variables ρ , u , v , P , t and E represent the gas density, velocity components in the z and r axis direction, pressure, time and total internal energy respectively. For transient cold spray simulations, the length scale is the shock tube diameter D . The velocity and density scales is the speed of sound (c_a) and density (ρ_a) in the quiescent region. The time scale is $\frac{D}{c_a}$ and the pressure, viscosity and total energy scales are each defined as $\rho_a c_a^2$. For steady cold spray simulations, the velocity and density scales are defined with respect to the nozzle exit conditions and the nozzle exit diameter is used as the length scale.

The Mach number and Reynolds number based on the ambient condition (or nozzle exit condition with subscript e instead of a) are defined as:

$$Ma = \frac{u_a}{c_a} \qquad Re = \frac{\rho_a u_a D}{\mu_a} \qquad (2.3)$$

The dimensionless kinematic viscosity is given by the Sutherland's law

$$\mu = T^{3/2} \left(\frac{1 + 110/T_a}{T + 110/T_a} \right) \qquad (2.4)$$

The governing Navier-Stokes equations cannot be solved on their own as there are three only equations (conservation of mass, momentum and energy) with four unknown dependant variables ρ , P , \mathbf{V} and e . A fourth equation can be obtained from a thermodynamic state reaction for e . Assuming a calorically ideal (polytropic) gas, the pressure and total internal energy are related by the equation of state Equation.2.5. The temperature can be calculated from the non-dimensionalised ideal gas law assuming $\gamma = 1.4$.

$$P = (\gamma - 1)[E - 0.5\rho(u^2 + v^2)] \qquad T = \frac{\gamma P}{\rho} \qquad c = \sqrt{\gamma RT} \qquad (2.5)$$

Since the focus of the research is on compressible supersonic flow, the ratio of Ma/Re would be negligible as the Mach number and Reynolds number would be of the order of $O(1)$ and $O(10^6)$ respectively. Hence the numerical method is essentially solving the two dimensional Euler equations which makes it amenable to the Godunov schemes discussed in the next section.

2.2 Godunov schemes

Godunov (1954) proposed a conservative method for solving hyperbolic non-linear conservation laws such as the Euler equations. In this method, the conservative variables are considered as being piecewise constant across each cell during each time step and the time evolution is determined by the exact solution of the Riemann problem at the intercell boundaries. The development of Godunov type methods over the past four decades can be attributed to three factors.

1. The compressible Navier-Stokes equation reduces to a hyperbolic system, the Euler equations, when the effects of viscosity and heat conduction are removed
2. It is generally accepted that hyperbolic terms of partial differential equations (PDEs) governing fluid flows impose the most stringent requirements on discretisation techniques
3. The theory of hyperbolic systems is more advanced than that of complete fluid models such as the Navier-Stokes equations

Conservation laws are systems of partial differential equations that can be written in the form shown in Equation.2.6.a. By defining the Jacobian as $\mathbf{A} = \frac{d\mathbf{F}}{d\mathbf{U}}$ Equation.2.6.a can be rewritten as Equation.2.6.b. The system is linear when the entries a_{ij} of \mathbf{A} are constants and quasi-linear when \mathbf{A} is a function of \mathbf{U} , that is $\mathbf{A}(\mathbf{U})$. Quasi-linear systems are in general also systems of non-linear equations.

$$\frac{\partial \mathbf{U}}{\partial t} + \frac{\partial \mathbf{F}}{\partial x} = \mathbf{S} \quad \mathbf{U} = \begin{bmatrix} u_1 \\ u_2 \\ \vdots \\ u_m \end{bmatrix} \quad \mathbf{F} = \begin{bmatrix} f_1 \\ f_2 \\ \vdots \\ f_3 \end{bmatrix} \quad (2.6a)$$

$$\frac{\partial \mathbf{U}}{\partial t} + \mathbf{A} \frac{\partial \mathbf{U}}{\partial x} = \mathbf{S} \quad \mathbf{A} = \begin{bmatrix} \partial f_1 / \partial u_1 & \dots & \partial f_1 / \partial u_m \\ \partial f_2 / \partial u_1 & \dots & \partial f_2 / \partial u_m \\ \vdots & \ddots & \vdots \\ \partial f_m / \partial u_1 & \dots & \partial f_m / \partial u_m \end{bmatrix} = \begin{bmatrix} a_{11} & \dots & a_{1m} \\ a_{21} & \dots & a_{2m} \\ \vdots & \ddots & \vdots \\ a_{m1} & \dots & a_{mm} \end{bmatrix} \quad (2.6b)$$

A system is said to be hyperbolic if matrix \mathbf{A} has m real eigenvalues $\lambda_1 \dots \lambda_m$ and a corresponding set of linearly independent right eigenvectors $\mathbf{K}^1 \mathbf{K}^2 \dots \mathbf{K}^m$. The term \mathbf{S} may contain source terms due to heating, cooling and gravitational forces. There can also be *inhomogeneous* terms generated by the breakup of divergence terms when using

coordinate systems other than the Cartesian one. The Euler equations are a set of hyperbolic non linear conservation laws. Other examples include the two dimensional shallow water equations (Toro (2001)) and the artificial compressibility equations (Toro (1997)).

The key ingredient of Godunov schemes is the solution of the one-dimensional Riemann problem by either exact or approximate methods. The Riemann problem for the one-dimensional Euler equations is given by the Initial Value Problem (IVP):

$$\frac{\partial \mathbf{U}}{\partial t} + \frac{\partial \mathbf{F}}{\partial x} = 0 \quad \mathbf{U} = \begin{bmatrix} \rho \\ \rho u \\ E \end{bmatrix} \quad \mathbf{F} = \begin{bmatrix} \rho u \\ \rho u^2 + P \\ u(E + P) \end{bmatrix} \quad (2.7)$$

with the initial conditions

$$\mathbf{U}(x, 0) = \mathbf{U}_{IC}(x) = \begin{cases} \mathbf{U}_L & \text{if } x < 0 \\ \mathbf{U}_R & \text{if } x > 0 \end{cases}$$

where \mathbf{U}_L and \mathbf{U}_R are the initial solution vector on the left and right hand side of $x = 0$. Physically in the context of Euler equations, the Riemann problem is a generalisation of the shock-tube problem where two stationary gases are initially separated by a diaphragm. In a real shock tube, the viscous interaction between the boundary layer and end walls produces a highly complex flow field as discussed previously in Section.1.6.

Figure.2.1 shows the solution to the Riemann problem for the one dimensional Euler equations as a function of space and time. The left and right fans can either be shock or rarefaction waves depending on the initial conditions while the middle wave is always a contact wave travelling at a wave speed of $S^* = u^*$. The wave speeds are the eigenvalues of the matrix \mathbf{A} generated when the Euler equations are rewritten in the form of Equation.2.6b. For the one dimensional Euler equations, there are three waves separating four states: W_L, W_L^*, W_R^* and W_R where the primitive solution vector W is defined as $W = [\rho \ u \ P]^T$. An analysis of the eigenstructure of the Euler equations reveals that both the pressure (P^*) and velocity (u^*) between the left and right waves (denoted as the star region) are constant. The density however takes on different values on the left (ρ_L^*) and right (ρ_R^*) hand side of the contact wave.

Due to the piece-wise nature of the data within each control volume, this generates a local Riemann problem at each cell interface (i.e. $i - 1/2$ and $i + 1/2$) as shown in Figure.2.2. Godunov proposed two approaches for generating the solution at the next

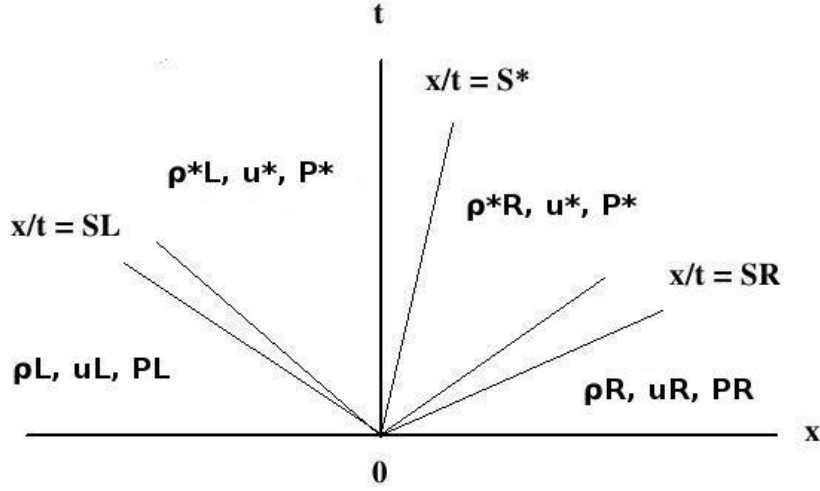


FIGURE 2.1: Solution structure of the Riemann problem for the one dimensional Euler equations.

time step. The first version of Godunov's method defines a new average \mathbf{U}_i^{n+1} using Equation.C.1.a. In this approach, the complete solution to the Riemann problem at each interface is integrated to obtain a new average \mathbf{U}_i^{n+1} at time Δt which is defined so that the waves generated at either interface do not intersect one another. In the second version, the new average \mathbf{U}_i^{n+1} is evaluated using Equation.C.1.b where the flux $\mathbf{F}_{i+1/2}$ is the solution to the Riemann problem along the line $x/t = 0$. The latter version is the one that is used for practical computations as the interfacial flux can be found using exact or approximate solutions to the Riemann problem.

$$\mathbf{U}_i^{n+1} = \frac{1}{\Delta x} \int_{x_{i-1/2}}^{x_{i+1/2}} \mathbf{U}(x, t^{n+1}) dx \quad (2.8a)$$

$$\mathbf{U}_i^{n+1} = \mathbf{U}_i^n + \frac{\Delta t}{\Delta x} [\mathbf{F}_{i-1/2}^n - \mathbf{F}_{i+1/2}^n] \quad (2.8b)$$

2.2.1 Solution to the Riemann problem

There are three steps involved in finding the exact solution to the Riemann problem along $\frac{x}{t} = 0$.

1. Calculate P^* and u^* by solving Equation.2.9 using a root-finding method

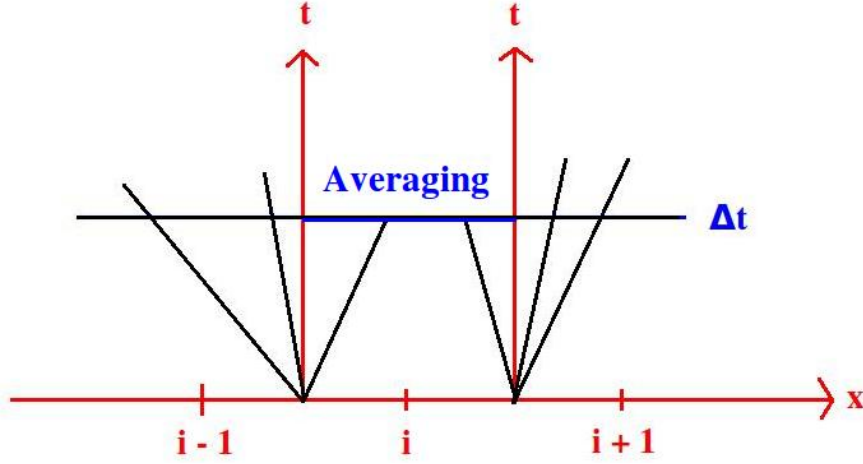


FIGURE 2.2: In the first version of Godunov's method, a new solution U_i^{n+1} is obtained by averaging the solution bounded by $i - 1/2$ and $i + 1/2$ at time Δt

2. Calculate the primitive variables within the star region and across any rarefaction or shock waves
3. Sample the solution of the complete wave structure and extract the solution at $W(x/t = 0)$ to calculate the intercell flux $\mathbf{F}_{i+1/2}$

Step.1 The solution of Equation.2.7 for the pressure P^* assuming an ideal gas is given by the root of the algebraic equation

$$f(P, W_L, W_R) = f_L(P, W_L) + f_R(P, W_R) + \Delta u = 0, \quad \Delta u = u_R - u_L \quad (2.9)$$

where the function f_L is given by

$$f_L(P, W_L) = \begin{cases} (P - P_L) \left[\frac{A_L}{P+B_L} \right]^{1/2} & \text{if } P > P_L \text{ (shock)} \\ \frac{2c_L}{\gamma-1} \left[\left(\frac{P}{P_L} \right)^{\frac{\gamma-1}{2\gamma}} - 1 \right] & \text{if } P < P_L \text{ (rarefaction)} \end{cases}$$

and the function f_R is given by

$$f_R(P, W_R) = \begin{cases} (P - P_R) \left[\frac{A_R}{P+B_R} \right]^{1/2} & \text{if } P > P_R \text{ (shock)} \\ \frac{2c_R}{\gamma-1} \left[\left(\frac{P}{P_R} \right)^{\frac{\gamma-1}{2\gamma}} - 1 \right] & \text{if } P < P_R \text{ (rarefaction)} \end{cases}$$

The data-dependent constants A_L, B_L, A_R, B_R are

$$\begin{aligned}
A_L &= \frac{2}{(\gamma + 1)\rho_L} & B_L &= \frac{\gamma - 1}{(\gamma + 1)P_L} \\
A_R &= \frac{2}{(\gamma + 1)\rho_R} & B_R &= \frac{\gamma - 1}{(\gamma + 1)P_R}
\end{aligned}$$

The unknown pressure P^* in the star region is found by solving the algebraic equation (Equation.2.9) using standard root finding techniques such as the Newton-Raphson method. The solution for the velocity u^* in the star region is then calculated using

$$u^* = \frac{1}{2}(u_L + u_R) + \frac{1}{2}(f_R(P^*) - f_L(P^*)) \quad (2.10)$$

Step.2 When the calculated pressure P^* is greater than the adjacent state a shock wave is formed otherwise a rarefaction wave occurs. Thus, two solutions are possible in the left and right star regions as shown in Figure.2.3 giving a total of four different possible solutions. The calculation of the density within the star regions for each case will be now be addressed.

Case A For a left shock wave ($P^* > P_L$), the density ρ_L^* and speed of the wave S_L is calculated using the Rankine-Hugoniot relations.

$$\rho_L^* = \rho_L \left[\frac{\frac{P^*}{P_L} + \frac{\gamma-1}{\gamma+1}}{\frac{\gamma-1}{\gamma+1} \frac{P^*}{P_L} + 1} \right] \quad S_L = u_L - c_L \left[\frac{\gamma+1}{2\gamma} \frac{P^*}{P_L} + \frac{\gamma-1}{2\gamma} \right]^{\frac{1}{2}} \quad (2.11)$$

Case B For a left rarefaction wave ($P^* < P_L$), the density ρ_L^* and speed of sound c_L^* are calculated using the isentropic relations

$$\rho_L^* = \rho_L \left(\frac{P^*}{P_L} \right)^{\frac{1}{\gamma}} \quad c_L^* = c_L \left(\frac{P^*}{P_L} \right)^{\frac{\gamma-1}{2\gamma}} \quad (2.12)$$

The solution within the rarefaction wave itself is given by

$$W_{Lfan} = \begin{cases} \rho = \rho_L \left[\frac{2}{\gamma+1} + \frac{\gamma-1}{(\gamma+1)c_L} \left(u_L - \frac{x}{t} \right) \right]^{\frac{2}{\gamma-1}} \\ u = \frac{2}{\gamma+1} \left[c_L + \frac{\gamma-1}{2} u_L + \frac{x}{t} \right] \\ P = P_L \left[\frac{2}{\gamma+1} + \frac{\gamma-1}{(\gamma+1)c_L} \left(u_L - \frac{x}{t} \right) \right]^{\frac{2\gamma}{\gamma-1}} \end{cases}$$

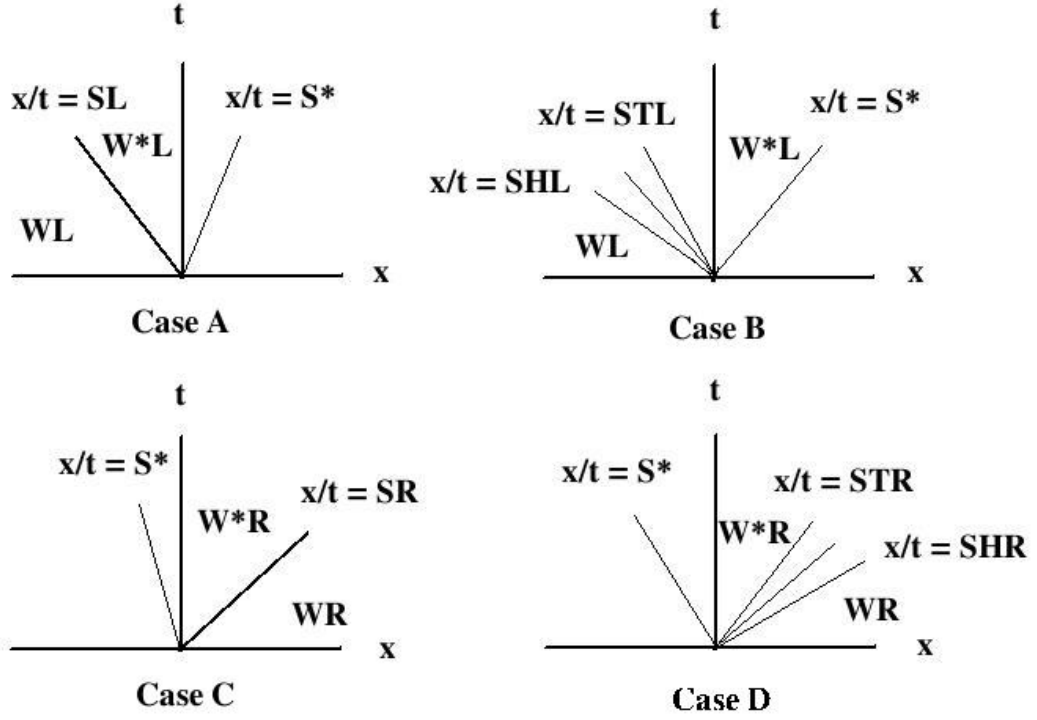


FIGURE 2.3: Possible solutions to the Riemann problem. Left star region (Cases A and B) and Right star region (Cases C and D).

The head (HL) and tail (TL) wave speeds encompassing the rarefaction wave are given by

$$S_{HL} = u_L - c_L \qquad S_{TL} = u^* - c_L^*$$

Case C For a right shock wave ($P^* > P_R$), the density ρ_R^* and speed of the wave S_R is calculated using the Rankine-Hugoniot relations.

$$\rho_R^* = \rho_R \left[\frac{\frac{P^*}{P_R} + \frac{\gamma-1}{\gamma+1}}{\frac{\gamma-1}{\gamma+1} \frac{P^*}{P_R} + 1} \right] \qquad S_R = u_R + c_R \left[\frac{\gamma+1}{2\gamma} \frac{P^*}{P_R} + \frac{\gamma-1}{2\gamma} \right]^{\frac{1}{2}} \quad (2.13)$$

Case D For a right rarefaction wave ($P^* < P_R$), the density ρ_R^* and speed of sound c_R^* are calculated using the isentropic relations

$$\rho_R^* = \rho_R \left(\frac{P^*}{P_R} \right)^{\frac{1}{\gamma}} \qquad c_R^* = c_R \left(\frac{P^*}{P_R} \right)^{\frac{\gamma-1}{2\gamma}} \quad (2.14)$$

The rarefaction wave is enclosed by the head (HR) and tail (TR) characteristics speeds

$$S_{HR} = u_R + c_R \qquad S_{TR} = u^* + c_R^*$$

To find the solution within the wave W_{Rfan} , the slope of the characteristic x/t is required

$$W_{Rfan} = \begin{cases} \rho = \rho_R \left[\frac{2}{\gamma+1} + \frac{\gamma-1}{(\gamma+1)c_R} \left(u_R - \frac{x}{t} \right) \right]^{\frac{2}{\gamma-1}} \\ u = \frac{2}{\gamma+1} \left[c_R + \frac{\gamma-1}{2} u_R + \frac{x}{t} \right] \\ P = P_R \left[\frac{2}{\gamma+1} + \frac{\gamma-1}{(\gamma+1)c_R} \left(u_R - \frac{x}{t} \right) \right]^{\frac{2\gamma}{\gamma-1}} \end{cases}$$

Step.3 Once the primitive solution vectors W_L , W_L^* , W_R^* and W_R are known, the solution along x/t can be determined via a sampling procedure. Consider the solution on the left of the contact wave $x/t < u^*$. When the left fan is a shock wave (Case A and B in Figure.2.3) there will be two constant states W_L and W_L^*

$$W(x, t) = \begin{cases} W_L^* & \text{if } S_L < \frac{x}{t} < S^* \\ W_L & \text{if } \frac{x}{t} < S_L \end{cases}$$

otherwise there will be three states W_L, W_{Lfan}, W_L^* for a rarefaction wave

$$W(x, t) = \begin{cases} W_L & \text{if } \frac{x}{t} < S_{HL} \\ W_{Lfan} & \text{if } S_{HL} < \frac{x}{t} < S_{TL} \\ W_L^* & \text{if } S_{TL} < \frac{x}{t} < S^* \end{cases}$$

Next consider the solution on the right of the contact wave $x/t > u^*$ (Case C and D in Figure.2.3). When the right wave is a shock wave there will be two constant states W_R, W_R^*

$$W(x, t) = \begin{cases} W_R^* & \text{if } S^* < \frac{x}{t} < S_R \\ W_R & \text{if } S_R < \frac{x}{t} \end{cases}$$

otherwise there will be three states W_R, W_{Rfan}, W_R^*

$$W(x, t) = \begin{cases} W_R & \text{if } S_{HR} < \frac{x}{t} \\ W_{Rfan} & \text{if } S_{TR} < \frac{x}{t} < S_{HR} \\ W_R^* & \text{if } S^* < \frac{x}{t} < S_{TR} \end{cases}$$

The fluxes $\mathbf{F}_{i+1/2}(x/t = 0)$ and $\mathbf{F}_{i-1/2}(x/t = 0)$ in Equation.C.1.b can now be evaluated to update the solution vector \mathbf{U}_i^{n+1} in Equation.C.1.a.

2.2.2 Multidimensional extension of the Riemann problem

For the two dimensional Euler equations in cylindrical coordinates, the discretised equation using Godunov method becomes

$$\mathbf{U}_{i,j}^{n+1} = \mathbf{U}_{i,j}^n + \frac{\Delta t}{\Delta z} [\mathbf{F}_{i-1/2,j}^n - \mathbf{F}_{i+1/2,j}^n] + \frac{\Delta t}{\Delta r} [\mathbf{G}_{i,j-1/2}^n + \mathbf{G}_{i,j+1/2}^n] + \frac{1}{r_{i,j}} \mathbf{S}_{i,j}^n \quad (2.15)$$

The intercell fluxes $\mathbf{F}_{i+1/2}$ and $\mathbf{G}_{j+1/2}$ are found by solving the split multidimensional Riemann problem. The x split Riemann problem becomes the IVP

$$\frac{\partial \mathbf{U}}{\partial t} + \frac{\partial \mathbf{F}}{\partial x} = 0 \quad \mathbf{U} = \begin{bmatrix} \rho \\ \rho u \\ \rho v \\ E \end{bmatrix} \quad \mathbf{F} = \begin{bmatrix} \rho u \\ \rho u^2 + P \\ \rho uv \\ u(E + P) \end{bmatrix} \quad (2.16)$$

with the initial conditions

$$\mathbf{U}(x, 0) = \mathbf{U}_{IC}(x) = \begin{cases} \mathbf{U}_L & \text{if } x < 0 \\ \mathbf{U}_R & \text{if } x > 0 \end{cases}$$

The solution shown in Figure.2.4 is nearly identical to that of the one-dimensional problem with the exception that the eigenvalues (see Appendix.A) $\lambda_x^2 = \lambda_x^4 = u$ generates two coincident contact waves. In the star region between the left and right waves, the solution for pressure and u component velocity remains constant as in the one dimensional case. The v component velocity changes across the contact waves and is equal to the initial left and right data values.

The y split Riemann problem becomes the IVP

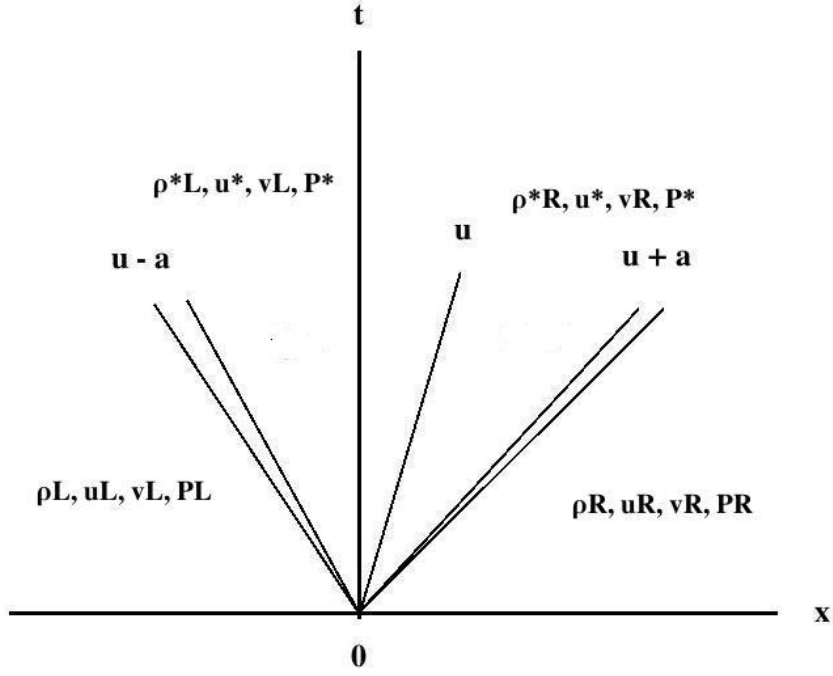


FIGURE 2.4: Solution structure for the split Riemann problem in the x direction.

$$\frac{\partial \mathbf{U}}{\partial t} + \frac{\partial \mathbf{G}}{\partial y} = 0 \quad \mathbf{U} = \begin{bmatrix} \rho \\ \rho v \\ \rho u \\ E \end{bmatrix} = \begin{bmatrix} \rho v \\ \rho v^2 + P \\ \rho u v \\ v(E + P) \end{bmatrix} \quad (2.17)$$

with initial conditions

$$\mathbf{U}(y, 0) = \mathbf{U}_{IC}(y) = \begin{cases} \mathbf{U}_L & \text{if } y < 0 \\ \mathbf{U}_R & \text{if } y > 0 \end{cases}$$

The solution is exactly the same as the previous solution with the variable u replaced by v and vice versa. The source term \mathbf{S} is evaluated directly using the values at the cell center.

2.3 Approximate Riemann solvers

To save computational time, approximate solutions to the Riemann problem have been developed. Approximate, non-iterative solutions can provide the necessary state information using one of two approaches. One approach is to find a direct approximation of the numerical flux ($\mathbf{F}_{i+1/2}$) employed in Godunov's method. Another approach is to approximate the solution structure ($W_{i+1/2}$) at the interface and then evaluate the flux (Toro & Chou (1993)). The Riemann solvers used in the present investigation adopts the former approach.

2.3.1 HLLC Riemann solver

Harten & Osher (1987) were one of the first to solve the Riemann problem approximately. The resulting solvers have since been referred to as the Harten, Lax and van Leer (HLL) Riemann solvers. The principal idea is to assume a solution structure that consists of two waves separating three states for one dimensional conservations laws. This is exact for hyperbolic systems with only two equations such as the one-dimensional shallow water equations. For larger systems such as the Euler equations or the two dimensional shallow water equations, the two wave assumption is incorrect as it ignores physical features such as contact waves, shear waves and material interfaces.

To overcome these shortcomings, a modified HLLC (C stands for for contact) Riemann solver was developed by Toro *et al.* (1994). A first order HLLC flux $\mathbf{F}_{i+1/2}$ for the solution of Equation.C.1b assumes three waves separating four states as shown in Figure.2.5. The extra state F_{2-4} between the coincident waves S_2 and S_4 is for the TVD modification of the first order flux later on.

$$\mathbf{F}_{i+1/2} = \begin{cases} \mathbf{F}_L & \text{if } x/t \leq S_L \\ \mathbf{F}_L^* = \mathbf{F}_L + S_L(\mathbf{U}_L^* - \mathbf{U}_L) & \text{if } S_L \leq x/t \leq S^* \\ \mathbf{F}_R^* = \mathbf{F}_R + S_R(\mathbf{U}_R^* - \mathbf{U}_R) & \text{if } S^* \leq x/t \leq S_R \\ \mathbf{F}_R & \text{if } S_R \leq x/t \end{cases}$$

where U_K^* is defined as

$$\mathbf{U}_K^* = \rho_K \frac{S_K - u_K}{S_K - S^*} \begin{bmatrix} 1 \\ v_K \\ S^* \\ \frac{E_K}{\rho_K} + (S^* - u_K) \left[S^* + \frac{P_K}{\rho_K(S_K - u_K)} \right] \end{bmatrix}, \quad (2.18)$$

The subscript K can be set to either L or R to distinguish the left i and right $i + 1$ cells. To calculate the fluxes for the HLLC Riemann solvers, the wave speeds S_K are needed.

$$\begin{cases} S_L = u_L - c_L & \text{if } P^* \leq P_L \\ S_L = u_L - c_L \left[\frac{\gamma+1}{2\gamma} \frac{P^*}{P_L} + \frac{\gamma-1}{2\gamma} \right]^{1/2} & \text{if } P^* \geq P_L \\ S^* = u^* \\ S_R = u_R + c_R & \text{if } P^* \leq P_R \\ S_R = u_R + c_R \left[\frac{\gamma+1}{2\gamma} \frac{P^*}{P_R} + \frac{\gamma-1}{2\gamma} \right]^{1/2} & \text{if } P^* \geq P_R \end{cases}$$

An adaptive non-iterative Riemann solver is used to predict the pressure P^* and velocity u^* in the star region. If the following conditions are satisfied, the primitive variable Riemann solver is used

$$\begin{aligned} P_{max}/P_{min} < Q_{user} \quad P_{min} < P^* < P_{max} \\ P_{PVRS} = \frac{1}{c_L + c_R} [c_R P_L + c_L P_R c_L P_R (u_L - u_R)] \end{aligned} \quad (2.19)$$

where $P_{min} = \min(P_L, P_R)$, $P_{max} = \max(P_L, P_R)$ and $P^* = P_{PVRS}$. Extensive testing suggest that a value $Q_{user} = 2$ is adequate for robust and efficient schemes. The velocity in the star region is given by:

$$u^* = \frac{1}{c_L + c_R} [c_L u_L + c_R u_R + P_R - P_L] \quad (2.20)$$

If $P_{PVRS} < P_{min}$, the two-rarefaction Riemann solver is used which assumes a rarefaction wave for the left and right travelling waves shown in Figure.2.4.

$$P^* = \frac{1}{2} \left\{ P_L \left[1 + \frac{\gamma-1}{2c_L} (u_L - u^*) \right]^{1/z} + P_R \left[1 + \frac{\gamma-1}{2c_R} (u^* - u_R) \right]^{1/z} \right\} \quad (2.21)$$

$$u^* = \frac{P_{LR} u_L / c_L + u_R / c_R + 2(P_{LR} - 1) / (\gamma - 1)}{P_{LR} / c_L + 1 / c_R} \quad (2.22)$$

where $P_{LR} = \frac{P_L}{P_R} \frac{\gamma-1}{2\gamma}$ and $z = \frac{\gamma-1}{2\gamma}$.

If ($P_{PVRS} > P_{min}$) the two-shock Riemann solver is used which assumes a shock wave for the left and right travelling waves shown in Figure.2.4.

$$P^* = \frac{g_L(P_{PVRS})P_L + g_R(P_{PVRS})P_R - (u_R - u_L)}{g_L(P_{PVRS}) + g_R(P_{PVRS})} \quad (2.23)$$

$$u^* = \frac{1}{2}(u_L + u_R) + \frac{1}{2} [(P^* - P_R)g_R(P_{PVRS}) - (P^* - P_L)g_L(P_{PVRS})] \quad (2.24)$$

where $g_K(P) = \sqrt{\left(\frac{2}{\rho_K(\gamma+1)}\right) / \left(P + P_K \frac{\gamma-1}{\gamma+1}\right)}$

According to Godunov's theorem (Godunov (1954)), although Godunov schemes using first order fluxes like those of Equation.2.18 are monotonous, they are inaccurate to be of practical interest. Higher order schemes, on the other hand, produce undesired spurious oscillations near the vicinity of high gradients. Ideally schemes should possess the oscillation-free property of monotone schemes while retaining the accuracy of high order methods. The total variation diminishing version of the HLLC method meets both of these requirements. For a discussion on the nature of the TVD property and how it is achieved, the reader should refer to Appendix.B. In the case of scalar conservation laws such as the advection equation, the TVD property is enforced in a rigorous and mathematical manner. The extension to non-linear systems is strictly speaking empirical but found to work well in practice.

Here, the Weighted Average Flux (WAF) approach is used to obtain a second-order extension of the HLLC flux. This flux is the integral average of the physical flux across the full solution of the local Riemann problem. By definition

$$\mathbf{F}_{i+1/2} = \frac{1}{\Delta x} \int_{x_i}^{x_{i+1}} \mathbf{F}(U_{i+1/2}(x, \Delta t/2)) dx \quad (2.25)$$

Because there are four wave speeds separating five states as shown in Figure.2.5 (an extra state is included between the coincident waves S_2 and S_4 for the purpose of achieving TVD property), the integral becomes

$$\mathbf{F}_{i+1/2} = \beta_1 F_L + \beta_2 F_L^* + \beta_3 F_{2-4} + \beta_4 F_R^* + \beta_5 F_R \quad (2.26)$$

where F_L , F_L^* , F_R^* and F_R can be readily found using Equation.2.18, N is the number of waves in the solution of the Riemann problem and β_k is the normalised length of segments $A_{k-1}A_k$

$$\beta_k = \frac{|A_{k-1}A_k|}{\Delta x} = f(\phi_k, Co_k)$$

The expressions for calculating the normalised lengths varies depending on the magnitude of the WAF limiter ϕ_k and Co_k . The WAF limiter function ($\phi_{1,2,3,4}$) used in the current study is that proposed by van Albada *et al.* (1982).

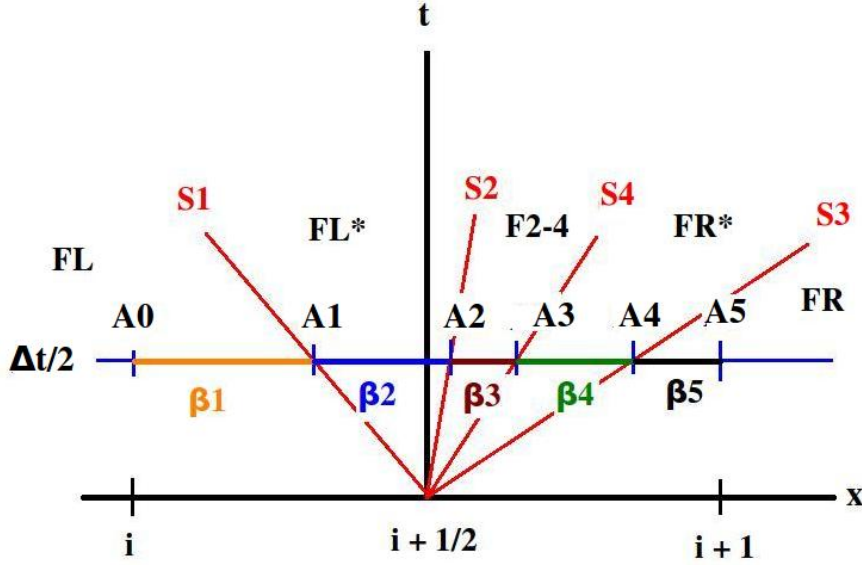


FIGURE 2.5: Evaluation of the WAF flux for the case where $\phi_2 < \phi_4$. Note waves S_2 and S_4 are actually coincident but plotted separately to indicate state 2-4.

$$\phi_k(r_k, Co_k) = \begin{cases} 1 & \text{if } r_k \leq 0 \\ 1 - \frac{(1 - |Co_k|)r_k(1+r_k)}{1+r_k^2} & \text{if } r_k \geq 0 \end{cases}$$

$$\phi_k(r_k, Co_k) = \begin{cases} 1 & \text{if } r_k \leq 0 \\ 1 - \frac{(1 - |Co_k|)r_k(1+r_k)}{1+r_k^2} & \text{if } r_k \geq 0 \end{cases}$$

The variable r_k is defined as the ratio

$$r_k = \left\{ \begin{array}{l} \frac{\Delta q_{i-1/2}^k}{\Delta q_{i+1/2}^k} \quad \text{if } Co_k > 0 \\ \frac{\Delta q_{i+3/2}^k}{\Delta q_{i+1/2}^k} \quad \text{if } Co_k < 0 \end{array} \right\} k = 1 \dots 4.$$

The Courant number Co_k for wave speed S_k is given by

$$Co_k = \frac{\Delta t S_k}{\Delta x} \quad S_1 = S_L \quad S_2 = S_4 = S^* \quad S_3 = S_R \quad (2.27)$$

For the purpose of applying a TVD constraint to non-linear systems, a useful though empirical observation is that the solution may be characterised by jumps in a single quantity q (usually density) across each wave: $\Delta q^1 = \rho_L^* - \rho_L$, $\Delta q^2 = \rho_R^* - \rho_L^*$, $\Delta q^3 = \rho_R - \rho_R^*$ and $\Delta q^4 = v_R - v_L$. Note that the solution structure varies depending on the magnitude of ϕ_2 relative to ϕ_4 . If $\phi_2 < \phi_4$, the solutions are as shown in Figure.2.5.

Otherwise, the waves S_2 and S_4 are interchanged and this changes the normalised length $(\beta_{2,3,4})$.

For cases where $\phi_2 < \phi_4$, the primitive variables in flux F_{2-4} is given by

$$\rho = \rho_R \quad u = u_R \quad v = v_L \quad P = P_R$$

and the normalised lengths becomes

$$\begin{aligned} \beta_1 &= \frac{1}{2}(Co_1\phi_1 + 1) & \beta_2 &= \frac{1}{2}(Co_2\phi_2 - Co_1\phi_1) & \beta_3 &= \frac{1}{2}(Co_4\phi_4 - Co_2\phi_2) \\ & & \beta_4 &= \frac{1}{2}(Co_3\phi_3 - Co_4\phi_4) & \beta_5 &= \frac{1}{2}(1 - Co_3\phi_3) \end{aligned} \quad (2.28)$$

Otherwise, if $\phi_2 > \phi_4$ the flux F_{4-2} is given by substitution of

$$\rho = \rho_L \quad u = u_L \quad v = v_R \quad P = P_L$$

and the normalised length becomes

$$\begin{aligned} \beta_1 &= \frac{1}{2}(Co_1\phi_1 + 1) & \beta_2 &= \frac{1}{2}(Co_4\phi_4 - Co_1\phi_1) & \beta_3 &= \frac{1}{2}(Co_2\phi_2 - Co_4\phi_4) \\ & & \beta_4 &= \frac{1}{2}(Co_3\phi_3 - Co_2\phi_2) & \beta_5 &= \frac{1}{2}(1 - Co_3\phi_3) \end{aligned} \quad (2.29)$$

The calculation of the flux $\mathbf{G}_{j+1/2}^k$ follows exactly the same procedure except with u replaced by v and vice versa.

2.3.2 Roe's Riemann solver

The most commonly used approximate Riemann solver is the one proposed by Roe (1980). Roe solved the one dimensional Riemann problem for the Euler equations (Equation.2.30) by assuming that the Jacobian matrix is constant $\tilde{\mathbf{A}}(\mathbf{U}_L, \mathbf{U}_R)$. The exact Riemann problem is replaced by an approximate Riemann problem which can then be solved exactly. The linearised system reads

$$\frac{\partial \mathbf{U}}{\partial t} + \tilde{\mathbf{A}} \frac{\partial \mathbf{U}}{\partial x} = 0 \quad (2.30)$$

with initial conditions

$$\mathbf{U}(x, 0) = \mathbf{U}_{IC}(x) = \begin{cases} \mathbf{U}_L & \text{if } x < 0 \\ \mathbf{U}_R & \text{if } x > 0 \end{cases}$$

For a general hyperbolic system, Roe's Jacobian matrix $\tilde{\mathbf{A}}$ must satisfy the following properties:

1. Hyperbolicity of the system: $\tilde{\mathbf{A}}$ is required to have real eigenvalues $\tilde{\lambda}_i(\mathbf{U}_L, \mathbf{U}_R)$ and a complete set of linearly independent right eigenvectors

$$\tilde{\lambda}_1 < \tilde{\lambda}_2 < \dots < \tilde{\lambda}_m \quad \tilde{\mathbf{K}}^1, \tilde{\mathbf{K}}^2, \dots, \tilde{\mathbf{K}}^m$$

2. Consistency with the exact Jacobian $\tilde{\mathbf{A}}(\mathbf{U}, \mathbf{U}) = \mathbf{A}(\mathbf{U})$
3. Conservation across discontinuities

$$\mathbf{F}(\mathbf{U}_R) - \mathbf{F}(\mathbf{U}_L) = \tilde{\mathbf{A}}(\mathbf{U}_R - \mathbf{U}_L)$$

Property (1) is an obvious requirement; the approximate problem should preserve the mathematical character of the original non-linear system. Property (2) ensures consistency with the conservation laws by satisfying the integral form of Equation.2.7 expressed as $\int_{x_L}^{x_R} \mathbf{U}(x, \Delta t) dx = x_R \mathbf{U}_R - x_L \mathbf{U}_L + \Delta T(\mathbf{F}_L - \mathbf{F}_R)$ and shown in Figure.2.6. Property (3) ensures conservation and exact recognition of discontinuities. If the data $\mathbf{U}_L, \mathbf{U}_R$ are connected by a single isolated discontinuity, the approximate Riemann solver would recognise this wave exactly. The construction of matrices satisfying all three properties can be complicated and computationally expensive to implement. For the Euler equations, Roe proposed a relatively simple way of constructing matrix $\tilde{\mathbf{A}}$.

The structure of the solution to the linearised Riemann problem in the $x - t$ plane is shown in Figure.2.7. It consists of m waves emanating from the origin; one for each eigenvalue $\tilde{\lambda}_i$. Each wave carries a discontinuity in \mathbf{U} propagating at a wave speed of $\tilde{\lambda}_i$. Naturally, the solution to the left of the $\tilde{\lambda}_1$ wave is the initial solution vector \mathbf{U}_L and that to the right of the $\tilde{\lambda}_m$ wave is the initial solution vector \mathbf{U}_R . The task at hand is to find the solution between these two waves. To do this, it is useful to first transform the dependant variables \mathbf{U} into the characteristic variable $\mathbf{W} = \tilde{\mathbf{K}}^{-1} \mathbf{U}$ where $\tilde{\mathbf{K}}$ is the diagonalisation matrix such that $\tilde{\mathbf{A}} = \tilde{\mathbf{K}} \tilde{\Lambda} \tilde{\mathbf{K}}^{-1}$. The diagonal matrix $\tilde{\Lambda}$ consists of the eigenvalues of matrix $\tilde{\mathbf{A}}$ (See Appendix.A).

Multiplication of Equation.2.7 by $\tilde{\mathbf{K}}^{-1}$ gives the canonical or characteristic form of the linearised system:

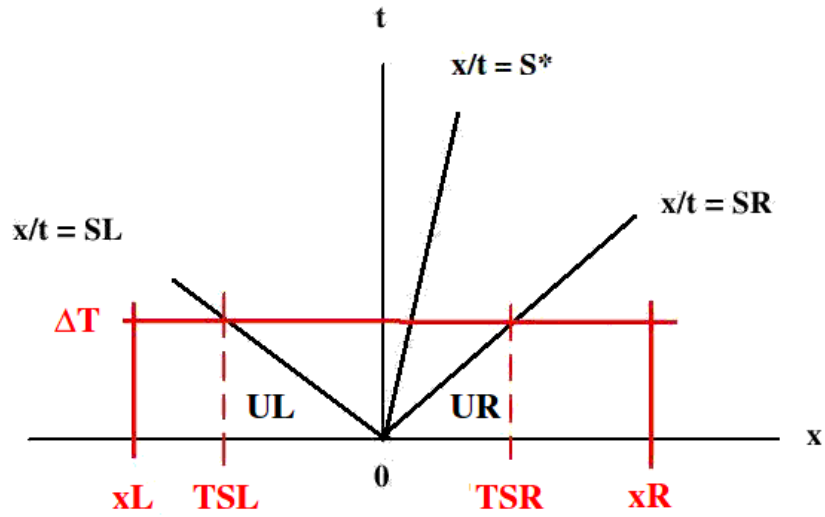


FIGURE 2.6: Control volume $[x_L, x_R] \times [0, \Delta t]$ on the $x - t$ plane. S_L and S_R are the fastest wave speeds arising from the solution to the Riemann problem

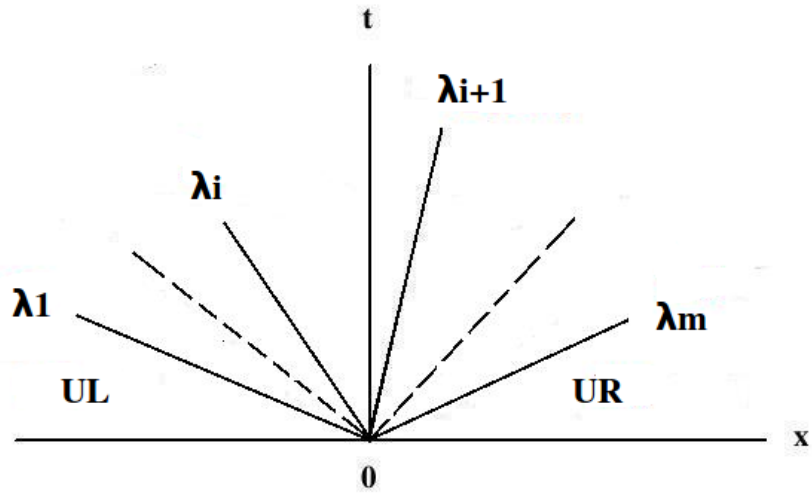


FIGURE 2.7: Solution structure for linear hyperbolic systems with constant coefficients.

$$\frac{\partial \mathbf{W}}{\partial t} + \tilde{\mathbf{A}} \frac{\partial \mathbf{W}}{\partial x} = 0 \quad (2.31)$$

When expanded in full, this system becomes:

$$\begin{bmatrix} w_1 \\ w_2 \\ \vdots \\ w_m \end{bmatrix}_t + \begin{bmatrix} \tilde{\lambda}_1 & \dots & 0 \\ 0 & \dots & 0 \\ \vdots & \ddots & \vdots \\ 0 & \dots & \tilde{\lambda}_m \end{bmatrix} \begin{bmatrix} w_1 \\ w_2 \\ \vdots \\ w_m \end{bmatrix}_x = 0$$

Clearly this a PDE involving a single unknown variable $w_i(x, t)$. The system has been decoupled and is identical to the linear advection equation for which the exact solution is:

$$\begin{aligned} \frac{\partial w_i}{\partial t} + \tilde{\lambda}_i \frac{\partial w_i}{\partial x} &= 0 \\ w_i(x, t) &= w_i^0(x - \tilde{\lambda}_i t) \quad \text{for } i = 1 \dots m \end{aligned} \quad (2.33)$$

The original matrix \mathbf{U} can now be obtained using the transformation $\mathbf{U} = \tilde{\mathbf{K}}\mathbf{W}$.

$$\mathbf{U}(x, t) = \sum_{i=1}^m w_i^0(x - \tilde{\lambda}_i t) \tilde{\mathbf{K}}^i \quad (2.34)$$

Equation.2.34 can be interpreted as the superposition of m waves, each of which is advected independently without a change in shape. Each wave has the initial shape w_i^0 and propagates with speed $\tilde{\lambda}_i$. The solution at a given point (x, t) is thus given by Equation.2.35

$$\mathbf{U}_{i+1/2}(x/t) = \sum_{i=1}^I \epsilon_i \tilde{\mathbf{K}}^i + \sum_{i=I+1}^m \alpha_i \tilde{\mathbf{K}}^i \quad (2.35)$$

where I is an integer such that $\tilde{\lambda}_I \leq x/t = 0 \leq \tilde{\lambda}_{I+1}$ and the constants ϵ_i and α_i represent the initial left and right conditions for wave i . The solution along $x/t = 0$ can be obtained from manipulation of Equation.2.35

$$\begin{aligned} \mathbf{U}_{i+1/2}(x/t = 0) &= \mathbf{U}_i^n + \sum_{i=1}^I (\epsilon_i - \alpha_i) \tilde{\mathbf{K}}^i \\ \mathbf{U}_{i+1/2}(x/t = 0) &= \mathbf{U}_{i+1}^n - \sum_{i=I+1}^m (\epsilon_i - \alpha_i) \tilde{\mathbf{K}}^i \end{aligned} \quad (2.36)$$

The above two equations can also be combined into a single equation of the form

$$\mathbf{U}_{i+1/2}(x/t = 0) = \frac{1}{2}(\mathbf{U}_i^n + \mathbf{U}_{i+1}^n) - \frac{1}{2} \sum_{i=1}^m \text{sign}(\tilde{\lambda}_i)(\epsilon_i - \alpha_i) \tilde{\mathbf{K}}^i \quad (2.37)$$

The intercell flux required to solve Equation.C.1b can be now be readily obtained from the relation $\tilde{\mathbf{A}}\tilde{\mathbf{K}} = \tilde{\lambda}_i\tilde{\mathbf{K}}$

$$\mathbf{F}_{i+1/2}(x/t = 0) = \frac{1}{2}(\mathbf{F}_i^n + \mathbf{F}_{i+1}^n) - \frac{1}{2} \sum_{i=1}^m |\tilde{\lambda}_i|(\epsilon_i - \alpha_i) \tilde{\mathbf{K}}^i$$

or as

$$\mathbf{F}_{i+1/2}(x/t = 0) = \frac{1}{2}(\mathbf{F}_i^n + \mathbf{F}_{i+1}^n) - \frac{1}{2} \sum_{i=1}^m |\tilde{\mathbf{A}}|(\epsilon_i - \alpha_i) \tilde{\mathbf{K}}^i \quad (2.38)$$

The large body of experience accumulated by researchers over the past four decades has produced several Jacobian matrices which satisfy all three properties presented at the beginning of this section. To achieve total variation diminishing properties for the intercell flux given in the form of Equation.2.38, Yee (1990) proposed the following expression.

$$\mathbf{F}_{i+1/2} = \frac{1}{2}(\mathbf{F}_{i+1} + \mathbf{F}_i + \mathbf{K}_{i+1/2}\varphi_{i+1/2}) \quad (2.39)$$

$$(2.40)$$

For a spatially second-order upwind TVD scheme, $\varphi_{i+1/2,j}$ is a 4 x 1 matrix with elements are written as

$$\varphi_{i+1/2}^l = \frac{1}{2}|\lambda_{i+1/2}^l|(\phi_{i+1}^l + \phi_i^l) - |\lambda_{i+1/2}^l + \zeta_{i+1/2}^l|\Gamma_{i+1/2}^l \quad (2.41)$$

- The element $\Gamma_{i+1/2}^l = \mathbf{K}_{i+1/2}^{-1}(\mathbf{U}_{i+1} - \mathbf{U}_i)$ is the forward difference of the local characteristic variables in the z direction
- $\lambda_{i+1/2}^l$ represent the eigenvalue of the Jacobian of matrix $\tilde{\mathbf{A}}_{i+1/2}$. They are $\lambda_{i+1/2}^1 = u - c$, $\lambda_{i+1/2}^2 = u$, $\lambda_{i+1/2}^3 = u + c$ and $\lambda_{i+1/2}^4 = u$.
- $\mathbf{K}_{i+1/2}^{-1}$ is a 4 x 4 matrix whose rows are the left eigenvectors of $\tilde{\mathbf{A}}_{i+1/2}$ (See Appendix.A)

- The 'extra eigenvalues' are given as:

$$\zeta_{i+1/2}^l = \frac{1}{2} |\lambda_{i+1/2}^l| \begin{cases} \frac{\phi_{i+1}^l - \phi_i^l}{\Gamma_{i+1/2}^l} & \text{if } \Gamma_{i+1/2}^l \neq 0 \\ 0 & \text{if } \Gamma_{i+1/2}^l = 0 \end{cases}$$

- The limiter function can be expressed in several ways

$$\begin{aligned} \phi_i^l &= \text{minmod}(\Gamma_{i+1/2}^l, \Gamma_{i-1/2}^l) \\ \phi_i^l &= (\Gamma_{i+1/2}^l \Gamma_{i-1/2}^l + |\Gamma_{i-1/2}^l \Gamma_{i+1/2}^l|) / (\Gamma_{i+1/2}^l + \Gamma_{i-1/2}^l) \\ \text{minmod}(a, b) &= \text{sign}(a, \max(0, \min(|a|, b \times \text{sign}(a)))) \end{aligned} \quad (2.42)$$

The same analogy applies for the flux $\mathbf{G}_{j+1/2} = \frac{1}{2}(\mathbf{G}_{j+1} + \mathbf{G}_j + \mathbf{K}_{j+1/2} \varphi_{j+1/2})$ with eigenvalues of $\lambda_{j+1/2}^1 = v - c$, $\lambda_{j+1/2}^2 = v$, $\lambda_{j+1/2}^3 = v + c$ and $\lambda_{j+1/2}^4 = v$.

2.4 Particle dynamics

A Lagrangian description of the particle motion is employed. The assumptions made in this approach are as follows:

1. The particles do not interact or collide with each other
2. Rotational motion of the particles are ignored
3. The coupling between the gas and particulate phase is removed on account of low particle loading during the spraying process
4. The tiny bow shock prior to each particle due to large velocity lag is not modelled.
5. The particles are solid spheres with uniform diameter and constant density

The drag acting on a spherical particle in the axial direction is written as

$$F_D = m_p \frac{du_p}{dt} = \frac{1}{2} \rho C_D (u - u_p) |u - u_p| A_p \quad (2.43)$$

After substituting the expression for the volume ($4/3\pi r^3$) and surface area ($4\pi r^2$) of a sphere, Equation.2.43 may be rewritten as

$$\frac{du_p}{dt} = \frac{3}{4} \left(\frac{\rho}{\rho_p D_p} \right) C_D (u - u_p) |u - u_p|$$

When recast in dimensionless form, Equation.2.44 becomes

$$\frac{du'_p}{dt'} = \frac{3}{4} \left(\frac{D_e \rho'_e}{\rho_p D_p} \right) C_D (u' - u'_p) |u' - u'_p|$$

where the ' denotes dimensionless values.

Denoting each particle I location by (z_{pI}, r_{pI}) , the complete set of laws governing particle motion are

$$\frac{d\mathbf{U}'_p}{dt} = \mathbf{I}'_p \quad (2.44)$$

where

$$\mathbf{U}'_p = \begin{bmatrix} z'_{pI} \\ r'_{pI} \\ u'_{pI} \\ v'_{pI} \end{bmatrix}, \quad \mathbf{I}'_p = \begin{bmatrix} u'_{pI} \\ v'_{pI} \\ \frac{3}{4} \left(\frac{D_e \rho'_e}{\rho_p D_p} \right) C_D (u'_I - u'_{pI}) |u'_I - u'_{pI}| \\ \frac{3}{4} \left(\frac{D_e \rho'_e}{\rho_p D_p} \right) C_D (v'_I - v'_{pI}) |v'_I - v'_{pI}| \end{bmatrix}$$

Each particle is labelled by the subscript I ($I = 1, 2, 3, \dots$). The non-dimensional variables u'_p and v'_p represent the particle velocity components in the z' and r' axis. For the transient cold spray simulation, the length scale is the shock tube diameter D , the velocity scale is the speed of sound a_a in the quiescent region and the fluid time scale is $\frac{D}{a_a}$. It's convenient to express the particle properties in terms of the Stokes number which is the ratio of the particle relaxation time and the fluid time scale. The definition of the Stokes number in a compressible flow is often defined by the response time of a particle across a normal shock Tedeschi *et al.* (1999) and will be discussed later in Section.3.2.

The drag coefficient is estimated using empirical formulas with the particle Reynolds number defined as $Re_I = \frac{\rho_I |u_I - u_{pI}| d_p}{\mu_I}$ (Carlson & Hoglund (1973)). The dimensional kinematic viscosity is calculated using Sutherland's law (Equation.2.4). Note that the velocity can either be the axial or radial depending on which direction the equation is being integrated.

$$C_{D_I} = \begin{cases} \frac{24}{Re_I} (1 + 1/6 Re_I^{2/3}) & \text{if } Re_I < 1000 \\ 0.44 & \text{if } Re_I > 1000 \end{cases}$$

Due to the high speed nature of the flow, there may be regions in the flow where the mean free path of the gas molecules are of the same order as the particle diameter. This ratio may be described by the particle Knudsen number Kn which is related to the particle Reynolds number and Mach number by

$$Kn_I = \frac{\Lambda}{D_p} = \sqrt{\frac{\gamma \pi}{2}} \frac{Ma_I}{Re_I}$$

To account for rarefaction effects over a wide range of Knudsen numbers, a modified drag coefficient is given by the same authors as

$$C_{D_I} = C_{D_I} \left[1 + \exp \left(\frac{-0.427}{Ma_I^{4.63}} - \frac{3}{Re_I} \right) \right] \quad (2.45)$$

where the Mach number $\frac{|u_I - u_{pI}|}{a_I}$ is based on the local velocity difference between the particle and gas. In principle the particle flow field is solved tracking each particle using the above equations. To save computational time, a large but tractable number of particles is included in the simulations. The gas velocity and density at a given particle

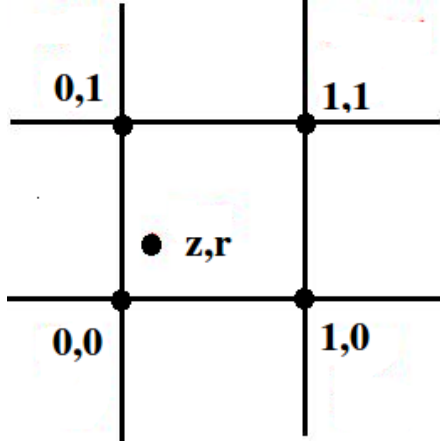


FIGURE 2.8: Bilinear interpolation of surrounding points.

location is obtained by applying a bilinear interpolation to the nearest four cell centers. The relative displacements z and r of the interpolated point is measured with respect to the bottom left node $(0, 0)$ as shown in Figure.2.8. The quantity $f(z, r)$ is given by the expression:

$$\begin{aligned}
 f(z, r) &= b_1 + b_2z + b_3r + b_4zr & (2.46) \\
 b_1 &= f(0, 0) \\
 b_2 &= f(1, 0) - f(0, 0) \\
 b_3 &= f(0, 1) - f(0, 0) \\
 b_4 &= f(0, 0) - f(1, 0) - f(0, 1) + f(1, 1)
 \end{aligned}$$

The rate of injection of the particles and the size distribution used in both steady and transient cold spray simulations are discussed in the next section.

2.5 Initial conditions

In order to simulate the transient cold spray process using a shock tube, a moving planar shock is passed through a constant diameter pipe into the ambient conditions. A schematic representation of the setup of the simulation is shown in the top of Figure.2.9. The gas flow is dictated by the shock speed Ma_{shock} and the distance between the pipe exit and impingement plate s/D . For a transient cold spray simulation, the length scale is the shock tube diameter D , the velocity and density scales are the speed of sound a_a and density ρ_a in the quiescent flow, the time scale is $\frac{D}{a_a}$ and the pressure and total energy scales are both defined as $\rho_a a_a^2$.

The non-dimensionalised ambient flow conditions are given by:

$$\rho'_a = \frac{\rho}{\rho_a} = 1 \quad P'_a = \frac{P_a}{\rho_a a_a^2} = \frac{1}{\gamma} \quad u'_a = \frac{u}{a_a} = 0 \quad v'_a = \frac{v}{a_a} = 0 \quad (2.47)$$

where $a_a = \sqrt{T_a} = \sqrt{\frac{\gamma P_a}{\rho_a}}$ assuming an ideal gas.

The physical post shock conditions are calculated using the shock relation for a moving frame of reference (White (1999)) travelling with the shock at speed Ma_{shock} .

$$\begin{aligned} \rho_P &= \frac{\rho_a(\gamma + 1)Ma_{shock}^2}{(\gamma - 1)Ma_{shock}^2 + 2} \\ P_P &= \frac{P_a}{\gamma + 1} (2\gamma Ma_{shock}^2 - (\gamma - 1)) \\ T_P &= T_a \left[2 + (\gamma - 1)Ma_{shock}^2 \frac{2\gamma Ma_{shock}^2 - (\gamma - 1)}{(\gamma + 1)^2 Ma_{shock}^2} \right] \\ u_P &= a_a Ma_{shock} - a_p \sqrt{\frac{(\gamma - 1)Ma_{shock}^2 + 2}{2\gamma Ma_{shock}^2 - (\gamma - 1)}} \\ v_P &= 0 \end{aligned}$$

When nondimensionalised with respect to ambient conditions, they become:

$$\begin{aligned} \rho'_P &= \frac{(\gamma + 1)Ma_{shock}^2}{(\gamma - 1)Ma_{shock}^2 + 2} \\ P'_P &= \frac{1}{\gamma(\gamma + 1)} (2\gamma Ma_{shock}^2 - (\gamma - 1)) \\ u'_P &= Ma_{shock} - \sqrt{\frac{T_P}{T_a}} \times \frac{(\gamma - 1)Ma_{shock}^2 + 2}{2\gamma Ma_{shock}^2 - (\gamma - 1)} \\ v'_P &= 0 \end{aligned} \quad (2.48)$$

For a steady jet cold spray simulation, the flow conditions at the nozzle exit are fixed during the course of the simulation. The flow variables are defined with respect to the nozzle exit conditions and the nozzle exit diameter is used as the length scale. Thus, the non-dimensionalised nozzle exit flow conditions are:

$$\rho'_e = \frac{\rho}{\rho_e} = 1 \quad P'_e = \frac{P}{\rho_e a_e^2} = \frac{1}{\gamma} \quad u'_e = \frac{u}{a_e} = Ma \quad v'_e = \frac{v}{a_e} = Ma_e * \tan(\theta) \quad (2.49)$$

where θ is the nozzle divergence angle relative to the axial axis. The initial ambient conditions are expressed as

$$\rho'_a = \frac{1}{\rho_r} \quad P'_a = \frac{P}{\rho_a a_a^2} = \frac{1}{P_r} \quad u'_a = \frac{u}{a_e} = 0 \quad v'_a = \frac{v}{a_e} = 0 \quad (2.50)$$

where ρ_r and P_r are the density, temperature and pressure ratios across the nozzle exit calculated assuming isentropic flow through the nozzle.

$$\begin{aligned} \frac{P_0}{P_e} &= \left(1 + \frac{1}{2}(\gamma - 1)Ma_e^2\right)^{\frac{\gamma}{\gamma-1}} \\ \frac{\rho_0}{\rho_e} &= \left(1 + \frac{1}{2}(\gamma - 1)Ma_e^2\right)^{\frac{1}{\gamma-1}} \\ \frac{A_e}{A_t} &= \frac{1}{Ma_e} \left[\frac{1 + \frac{1}{2}(\gamma - 1)Ma_e^2}{\frac{1}{2}(\gamma + 1)} \right]^{\frac{1}{2} \frac{\gamma+1}{\gamma-1}} \end{aligned}$$

In the steady cold spray simulation, 10000 particles are randomly injected across the nozzle exit after the supersonic impinging gas jet has reached a steady state solution. The particle injection point is varied using Equation.2.51 where RN is a randomly generated number between 0 and 1. The injection velocity assumes that each particle has been released from rest at the nozzle throat and accelerated along a diverging length of 10 cm. The term $\frac{D_t}{D_e}$ in Equation.2.51 comes from the assumption that the particles travel in a rectilinear path inside the diverging section and does not spread beyond the throat diameter. In the unsteady cold spray simulation, four particles are released from rest across the pipe exit at $r/D_e = 0.1, 0.2, 0.3$ and 0.4 after the passing of the planar shock.

$$r_{pI} = 0.5 \times \frac{D_t}{D_e} \times RN \quad (2.51)$$

The particle diameter ranges between 1.5 and 50 μm . This is because a smaller value would cause the denominator in Equation.2.44 to approach zero and produces an infinite particle acceleration.

2.6 Boundary conditions

Numerical solutions to hyperbolic systems of differential equations such as the Euler equations are obtained over a finite domain. The time evolution of the system is governed not only by the interior region but also by waves entering and leaving the boundaries. There are three main types of nonreflecting boundary conditions which fall under the category of characteristic methods, farfield asymptotic solutions and buffer zone techniques.

A characteristic analysis of the Euler equations to derive the nonreflecting boundary conditions was presented by Thompson (1987b) and Thompson (1990). In this analysis, the boundary equations are written in the characteristic form and a specific boundary condition is imposed by assigning a value to the characteristic waves entering or leaving the boundary. Due to the one-dimensional formulation, they perform best when the outgoing wave is normal to the boundary. The farfield asymptotic boundary conditions are based on the asymptotic solution of the governing fluid equations as shown by Tam & Webb (1993). Such boundary conditions have limited application due to the difficulties of obtaining asymptotic solutions for complex flows.

The buffer zone technique is a group of boundary conditions based on damping methods. Here, the computational domain is extended to include a buffer region in which the solution is damped by the application of low-pass filters, grid stretching or numerical damping (Wasistho *et al.* (1997) and Freund (1997)). The buffer zone technique is the easiest one to implement but the inclusion of artificial damping within the zone means that the solution is not physical. The addition of extra grid points within the buffer zone adds to the computational costs as well. Another approach is to accelerate the flow to supersonic speeds at the end of the buffer zone, thus eliminating the need for a nonreflecting boundary condition as proposed by Ta'asan & Nark (1995).

A more complicated formulation based on the numerical damping approach is the Perfectly Matched Layer (PML) method. Again, extra damping regions are added around the existing computational domain in which the outgoing waves are damped. The first PML boundary condition for the split Euler equations was proposed by Hu (1996). A second application of the PML technique was given by Arbabanel *et al.* (1996). In both formulations, exponentially growing solutions at the boundaries were observed under certain flow conditions and required the inclusion of filtering and artificial damping to maintain stable solutions.

In the present investigation, a unified treatment of the nonreflecting boundary conditions for systems of hyperbolic equations proposed by Thompson (1987b) and Thompson (1990) is chosen. For the x_1 boundary, the boundary equations are written as:

$$\begin{aligned}
\frac{\partial \rho}{\partial t} + d_1 + \frac{\partial \rho u_2}{\partial x_2} &= 0 \\
\frac{\partial e}{\partial t} + \frac{1}{2} \left(\sum_{k=1}^2 u_k^2 \right) d_1 + \frac{d_5}{\gamma - 1} + \rho u_1 d_2 - \rho u_2 d_3 + \frac{\partial [(e + P)u_2]}{\partial x_2} &= 0 \\
\frac{\partial(\rho u_1)}{\partial t} + u_1 d_1 + \rho d_2 + \frac{\partial(\rho u_2 u_1)}{\partial x_2} &= 0 \\
\frac{\partial(\rho u_2)}{\partial t} + u_2 d_1 - \rho d_3 + \frac{\partial(\rho u_2 u_2)}{\partial x_2} + \frac{\partial P}{\partial x_2} &= 0
\end{aligned} \tag{2.52}$$

where

$$\begin{aligned}
\xi_1 &= \lambda_1 \left(\frac{\partial \rho}{\partial x_1} - \frac{1}{c^2} \frac{\partial P}{\partial x_1} \right) & d_1 &= \xi_1 + \frac{\rho}{2c} (\xi_4 + \xi_5) \\
\xi_3 &= -\lambda_3 \frac{\partial u_2}{\partial x_1} & d_2 &= \frac{1}{2} (\xi_4 - \xi_5) \\
\xi_4 &= \lambda_4 \left(\frac{\partial u_1}{\partial x_1} + \frac{1}{\rho c} \frac{\partial P}{\partial x_1} \right) & d_3 &= -\xi_3 \\
\xi_5 &= \lambda_5 \left(-\frac{\partial u_1}{\partial x_1} + \frac{1}{\rho c} \frac{\partial P}{\partial x_1} \right) & d_5 &= \frac{\rho c}{2} (\xi_4 + \xi_5)
\end{aligned} \tag{2.53}$$

Let the solution domain in the x_1 direction be defined by $a_1 \leq x_1 \leq b_1$. For all interior points $a_1 < x_1 < b_1$, the Euler equations are solved using standard Godunov schemes. At $x_1 = a_1$ and $x_1 = b_1$, the boundary equations solved. The boundaries of interest for the present investigation are the slip wall boundary condition and the nonreflecting boundary condition imposed on the farfield.

For a slip wall, the normal velocity must be zero. The initial data must have zero normal velocity at the walls and the purpose of the boundary condition is to keep them fixed at all times. The quantities $\xi_{4,5}$ are calculated using Equation.2.53 but $\xi_{1,2,3}$ must be chosen to force u_2 to be zero. The list of boundary conditions are

$x_1 = a_1(u_1 = 0)$	$x_1 = b_1(u_1 = 0)$
$\xi_1 = \xi_2 = \xi_3 = 0$	$\xi_1 = \xi_2 = \xi_3 = 0$
$\xi_5 = \lambda_5 \left(-\frac{\partial u_1}{\partial x_1} + \frac{1}{\rho c} \frac{\partial P}{\partial x_1} \right)$	$\xi_4 = \lambda_4 \left(\frac{\partial u_1}{\partial x_1} + \frac{1}{\rho a} \frac{\partial P}{\partial x_1} \right)$
$\xi_4 = \xi_5$	$\xi_5 = \xi_4$

(2.54)

For the nonreflecting boundary conditions, the quantities ξ are calculated using Equation.2.53 provided the waves λ_i are leaving the left ($x_1 = a$) and right ($x_1 = b$) boundaries. Otherwise, $\xi_i = 0$ assuming there is no gravitational forces.

The same approach applies in the x_2 direction, where the boundary equations are written as:

$$\begin{aligned}
& \frac{\partial \rho}{\partial t} + d_1 + \frac{\partial \rho u_2}{\partial x_2} = 0 \\
\frac{\partial e}{\partial t} + \frac{1}{2} \left(\sum_{k=1}^2 u_k^2 \right) d_1 + \frac{d_5}{\gamma - 1} + \rho u_1 d_2 + \rho u_2 d_3 + \frac{\partial[(e + P)u_2]}{\partial x_2} \\
& \frac{\partial(\rho u_1)}{\partial t} + u_1 d_1 + \rho d_2 + \frac{\partial(\rho u_1 u_1)}{\partial x_1} + \frac{\partial P}{\partial x_1} = 0 \\
& \frac{\partial(\rho u_2)}{\partial t} + u_2 d_1 + \rho d_3 + \frac{\partial(\rho u_1 u_2)}{\partial x_1} = 0
\end{aligned}$$
(2.55)

The quantity ζ_i replaces ξ_i when imposing the boundary conditions in the x_2 direction using Equation.2.54.

$\zeta_2 = \lambda_2 \left(\frac{\partial \rho}{\partial x_2} - \frac{1}{c^2} \frac{\partial P}{\partial x_2} \right)$	$d_1 = \zeta_2 + \frac{\rho}{2c} (\zeta_4 + \zeta_5)$
$\zeta_3 = \lambda_3 \frac{\partial u_1}{\partial x_2}$	$d_2 = \zeta_3$
$\zeta_4 = \lambda_4 \left(\frac{\partial u_2}{\partial x_2} + \frac{1}{\rho c} \frac{\partial P}{\partial x_2} \right)$	$d_3 = \frac{1}{2} (\zeta_4 - \zeta_5)$
$\zeta_5 = \lambda_5 \left(-\frac{\partial u_2}{\partial x_2} + \frac{1}{\rho c} \frac{\partial P}{\partial x_2} \right)$	$d_5 = \frac{\rho c}{2} (\zeta_4 + \zeta_5)$

(2.56)

2.7 Spatial discretization

The calculation of the spatial derivatives warrants some discussion. Of the many approximations available, the finite difference schemes are the simplest and have been used here. The accuracy of the finite difference scheme is described by its order of convergence (the power of Δx at which its error vanishes in the limit as $\Delta x \rightarrow 0$). The global order of convergence is often one greater than the order of convergence of the finite difference scheme used for the interior points. This is because when same order scheme is used for both the interior and boundary points, it can sometimes lead to an unstable solution. Hence, the global order of convergence is that of the finite difference scheme used at the interior points.

A globally fourth order accurate scheme can be achieved using the finite difference schemes given in Equation.2.57. Let the control volume be defined by $a_1 \leq x_1 \leq b_1$ where $0 \leq i \leq N_1$. Assuming a uniform grid with spacing of $\Delta x_1 = \frac{b_1 - a_1}{N_1}$, the following approximations are used for the x_1 spatial derivatives at the interior points (i), left boundary ($1, 0$) and right boundary ($N - 1, N$).

$$\begin{aligned}
 \frac{\partial f}{\partial x_1} \Big|_i &= \frac{1}{12\Delta x_1} [8(f_{i+1} - f_{i-1}) - (f_{i+2} - f_{i-2})] \quad \text{for } i = 2 \dots N_1 - 2 \\
 \frac{\partial f}{\partial x_1} \Big|_0 &= \frac{1}{6\Delta x_1} [18(f_1 - f_0) - 9(f_2 - f_0) + 2(f_3 - f_0)] \\
 \frac{\partial f}{\partial x_1} \Big|_1 &= \frac{1}{6\Delta x_1} [2(f_1 - f_0) + 6(f_2 - f_1) - (f_3 - f_1)] \\
 \frac{\partial f}{\partial x_1} \Big|_{N_1-1} &= \frac{1}{6\Delta x_1} [2(f_{N_1} - f_{N_1-1}) + 6(f_{N_1-1} - f_{N_1-2}) - (f_{N_1-1} - f_{N_1-3})] \\
 \frac{\partial f}{\partial x_1} \Big|_{N_1} &= \frac{1}{6\Delta x_1} [18(f_{N_1} - f_{N_1-1}) - 9(f_{N_1} - f_{N_1-2}) + 2(f_{N_1} - f_{N_1-3})]
 \end{aligned} \tag{2.57}$$

At the x_1 boundaries, the transverse derivatives ($\frac{\partial}{\partial x_2}, \frac{\partial}{\partial x_3}$) are evaluated using the same approximations as the interior points as these quantities do not require information external to the control volume. The normal derivatives ($\frac{\partial}{\partial x_1}$) included in the quantities ξ_i are approximated using first order one-sided finite difference schemes. Complications arise at the corner points where two or three coordinate directions require boundary conditions simultaneously. Given that the flow is two dimensional (axisymmetric), a characteristic analysis of the x_2 direction is required to obtain the quantity ζ_i (see Equation.2.56). The x_2 derivatives are then replaced by appropriate linear com-

binations of ζ_i and ξ whose values are determined using either one-sided derivative or boundary conditions depending on the direction of the characteristic waves.

2.8 Temporal discretization

The governing equation is discretised in time as well as in space and the integration time step Δt must be less than an upper limit which varies during the course of the simulation. The constraints are that the solution must be stable and accurate. Having found the derivative at all grid points $\frac{\partial \mathbf{U}}{\partial t}$, the integrations between time t^n to time t^{n+1} can be done using a suitable ordinary differential equation solver. The accuracy of the time integration method is also described by its order of convergence (the power of Δt at which its error vanishes in the limit as $\Delta t \rightarrow 0$).

For time dependent simulations such as the transient cold spray process, the accuracy of the numerical solution is described by the global convergence rate. If we let $\Delta x_k \rightarrow 0$ and $\Delta t \rightarrow 0$ while keeping $\frac{\Delta x_k}{\Delta t}$ constant, then $\Delta x_k \propto \Delta t$ and the norm of the error of the solution at any fixed time goes to zero at some power of Δt ; this power is defined as the global order of convergence. When the spatial and temporal derivative approximations have different orders of convergence, the global rate order of convergence is the lesser of the two. Hence, it would be desirable to match the orders of convergence of both for optimum accuracy and efficiency. An exception to the matching rule can be made when the purpose of the simulation is to achieve a steady state solution as in the steady cold spray process.

Having defined the initial and boundary conditions, the governing equation can be solved using the cell centered Godunov method (see Section.2.2.2):

$$\left(\frac{\partial \mathbf{U}}{\partial t}\right)_{i,j} = \mathbf{U}_{i,j}^n + \frac{\Delta t}{\Delta z} [\mathbf{F}_{i-1/2,j}^n - \mathbf{F}_{i+1/2,j}^n] + \frac{\Delta t}{\Delta r} [\mathbf{G}_{i,j-1/2}^n + \mathbf{G}_{i,j+1/2}^n] + \frac{\mathbf{S}_{i,j}^n}{r_{i,j}} \quad (2.58)$$

Eq.2.59 is an ordinary differential equation in time and can be solved using a fourth-order Runge-Kutta scheme to match the order of convergence of the spatial derivatives.

$$\begin{aligned} \mathbf{U}^1 &= \mathbf{U}^n + \frac{1}{2} \Delta t \frac{d\mathbf{U}^n}{dt} \\ \mathbf{U}^2 &= \mathbf{U}^n + \frac{1}{2} \Delta t \frac{d\mathbf{U}^1}{dt} \\ \mathbf{U}^3 &= \mathbf{U}^n + \Delta t \frac{d\mathbf{U}^2}{dt} \\ \mathbf{U}^{n+1} &= \mathbf{U}^n + \frac{1}{6} \Delta t \left(\frac{d\mathbf{U}^n}{dt} + 2 \frac{d\mathbf{U}^1}{dt} + 2 \frac{d\mathbf{U}^2}{dt} + \frac{d\mathbf{U}^3}{dt} \right) \end{aligned} \quad (2.59)$$

The time step stability condition is determined by:

$$\Delta t = Co / \left(\frac{\Delta z}{\max(|u| + c)} + \frac{\Delta r}{\max(|v| + c)} \right) \quad Co \leq 2.06 \quad (2.60)$$

where the Courant number (Co) may be take any value less than 2.06 (Thompson (1987a)). The particle location and velocity is updated after solving the gas phase at each time step.

Summary

This concludes the discussion of the numerical methods used in the present investigation of both steady and transient cold spray processes. An assessment of the accuracy of the WAF-TVD-HLLC solver and Yee's improvement of Roe's Riemann solver is presented in Sections.3.2 and 3.3 respectively. The solvers were implemented in C++ using object orientated programming and executed on the clusters at the Victorian Partnership for Advanced Computing. The steady cold spray simulations typically take one to two days to reach convergence whereas the unsteady cold spray simulations can take up to five days. The data for each flow condition (2~5 GB) was downloaded and analysed on the local server at the Laboratory for Turbulence Research in Aerospace and Combustion.

Chapter 3

Results and discussion

The numerical data collected for the purpose of the present investigation are presented in this chapter. Section.3.1 presents a parametric study of the effects of the nozzle chamber pressure, temperature and geometry on the particle velocity at the nozzle exit. The attachment of a barrel section to the end of the nozzle is used to examine the changes in particle exit velocity. Section.3.2 presents the data extracted from simulations of the steady cold spray process in the region between the nozzle exit and substrate. The particle impact statistics are calculated followed by an examination of the particle dynamics during its flight between the nozzle exit and substrate. Section.3.3 investigates an unsteady cold spray process produced by the impingement of a planar shock issuing from a pipe. The flow morphology is visualised using a numerical schlieren technique and is complemented with streamwise and spanwise data. Particles are injected across the pipe exit to assess their response in transient high speed gas flows.

3.1 Cold spray nozzle dynamics

The first component of the present investigation aims to address several key issues regarding the cold spray nozzle design. It builds upon previous studies by exploring the potential benefits of attaching a constant diameter barrel section to the end of the nozzle to enhance the particle acceleration. To make the analysis more realistic, constant friction has been assumed along the nozzle and barrel section walls. But first, a parametric investigation of the isentropic underexpanded nozzle onto which the barrel is attached is performed.

The research objectives of this study are three fold.

1. To perform a parametric study of the nozzle exit particle velocity using an isen-

tropic underexpanded de-Laval nozzle

2. To solve the governing equations for compressible flow through a duct of varying cross section area
3. To compare the exit particle velocity achieved by acceleration through a constant diameter barrel and diverging section

The pressure requirement for a supersonic cold spray nozzle is analysed in Section.3.1.1. A parametric study of the isentropic nozzle performance is given in Section.3.1.2 followed by an assessment of using a barrel section to accelerate the particles in Section.3.1.3. The results from both sections are discussed in Section.3.1.5.

3.1.1 Cold spray nozzle design

Before modelling the flow through a cold spray nozzle, the first thing to check is that the nozzle is operating in the supersonic regime. The key to determining whether a de-Laval nozzle is supersonic or not is to identify the chamber pressure for which a normal shock occurs at the nozzle exit (see Case *f* of Figure.1.2). To calculate this pressure, one needs to first estimate the supersonic Mach number at the nozzle exit (Ma_e) using the empirical relations given below.

$$Ma_e \simeq \begin{cases} 1 + 1.2(A_e/A_t - 1)^{1/2} & \text{if } 1.0 < A_e/A_t < 2.9 \\ [216A_e/A_t - 254(A_e/A_t)^{2/3}]^{1/5} & \text{if } 2.9 < A_e/A_t < \infty \end{cases}$$

This value is also the speed of the gas prior to a normal shock at the nozzle exit. The pressure of the gas before the shock (P_e) can be calculated using the normal shock relations and assuming sea level post shock condition.

$$\frac{P_e}{P_a} = \frac{1}{\gamma + 1} [2\gamma Ma_e^2 - (\gamma - 1)] \quad (3.1)$$

The nozzle chamber pressure (P_0) required to produce this exit pressure can now be found by assuming isentropic gas flow up until the nozzle exit.

$$\frac{P_0}{P_e} = \left[1 + \frac{1}{2}(\gamma - 1)Ma_e^2 \right]^{\frac{\gamma}{\gamma - 1}} \quad (3.2)$$

Figure.3.1 plots the chamber pressure required for shocked (with a normal shock in the diverging section) and supersonic nozzle flow along with the corresponding exit

Mach number over a wide range of expansion ratios (A_e/A_t). The exit gas Mach number for an underexpanded and overexpanded nozzle is identical given that they have the same expansion ratio. The pressure requirement for a subsonic nozzle is shown in Figure.3.2 for comparison.

The effect of increasing the chamber temperature on the nozzle exit gas velocity is shown in Figure.3.3 for both shocked and supersonic nozzles. Although the exit Mach number remains unchanged for nozzles of the same expansion ratio, the physical velocity is a function of the local temperature ($u = \sqrt{\gamma RT}$) which in turn is governed by the chamber temperature. Note that in these graphs, the nozzle chamber temperature is increasing as the graphs translates upwards. The effect of the chamber temperature on a choked subsonic nozzle exit is also shown.

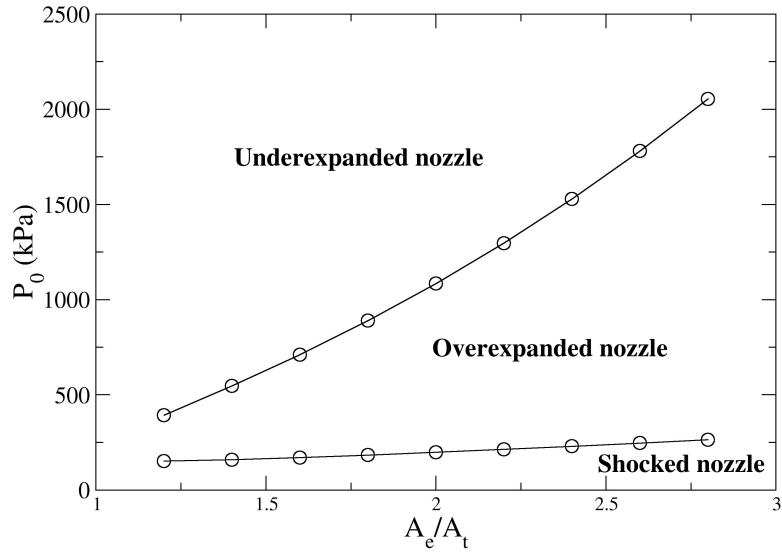
In supersonic nozzle flow, the pressure gradient along the diverging section of the nozzle is always favourable and hence no flow separation can occur. However, if there happens to be a shock in the diverging section, flow separation may occur along the nozzle walls due to pressure increase across the shock as discussed in Section.3.1. A large nozzle divergence angle increases the flow Mach number prior to a shock which in turn dictates the amount of pressure recovery across it. An expression for the divergence angle assuming a linear variation in nozzle diameter is defined as

$$\theta = \tan^{-1} \left(\frac{R_e - R_t}{L_D} \right) \quad (3.3)$$

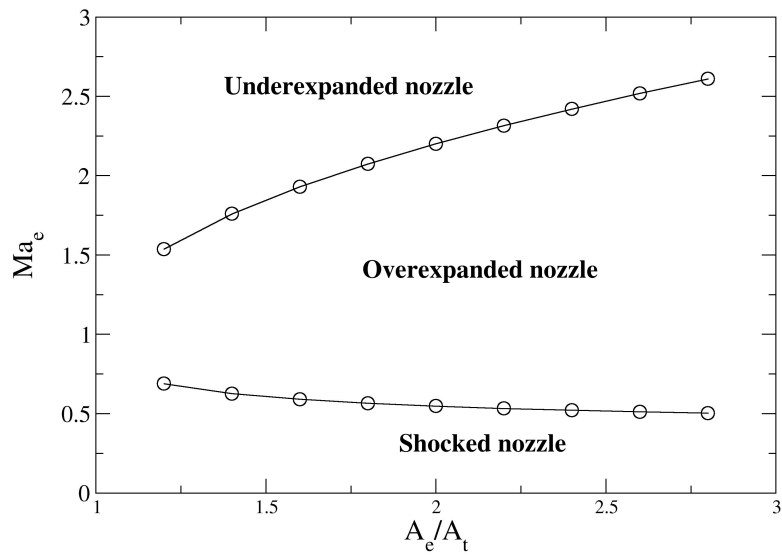
where R and L_D are the nozzle radius and diverging length respectively. When expressed in terms of the nozzle expansion ratio A_e/A_t , the expression becomes:

$$\begin{aligned} \theta &= \tan^{-1} \left(\frac{R_e/r_t - 1}{L_D} R_t \right) \\ \theta &= \tan^{-1} \left(\frac{\sqrt{A_e/A_t} - 1}{L_D} R_t \right) \\ \theta &= \tan^{-1} \left((\sqrt{A_e/A_t} - 1) \frac{R_t}{L_D} \right) \end{aligned} \quad (3.4)$$

This relationship is plotted in Figure.3.4 in terms of the nozzle 'slenderness ratio' (R_t/L_d).



(a) Chamber pressure.



(b) Exit Mach number

FIGURE 3.1: (a) Pressure requirement and (b) exit Mach number for flow through a shocked and supersonic de-Laval nozzle.

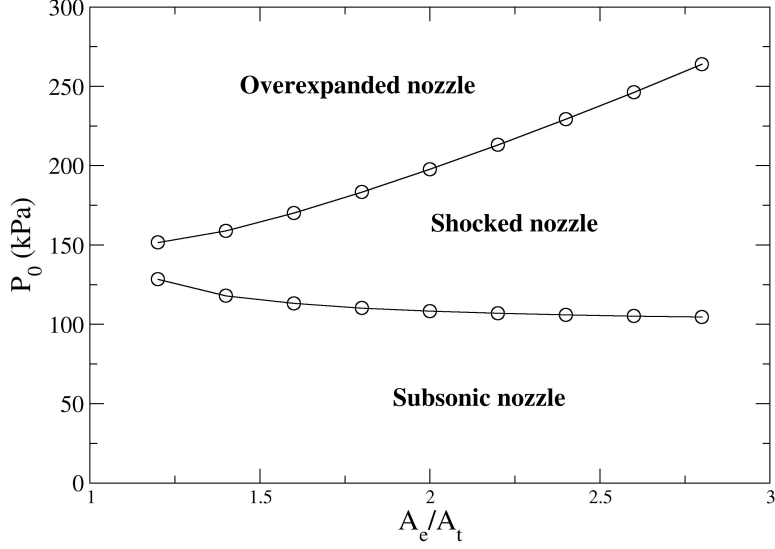


FIGURE 3.2: Pressure requirement for flow through a subsonic and supersonic de-Laval nozzle.

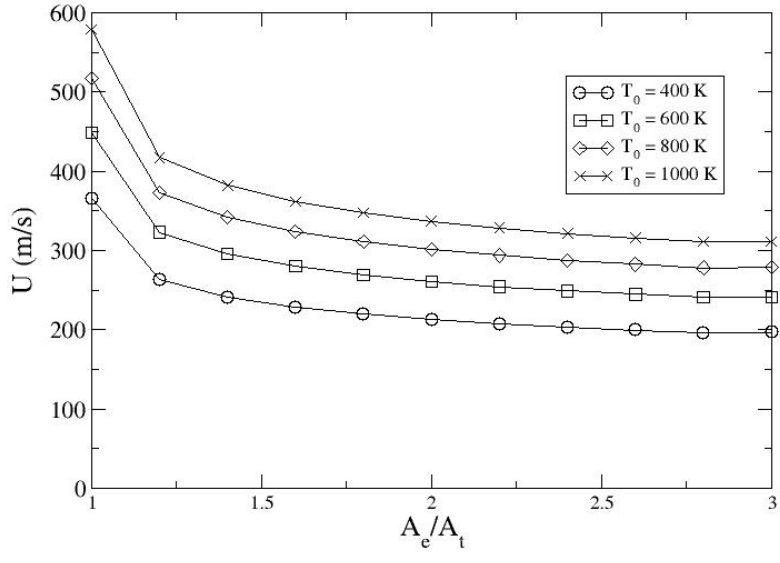
3.1.2 Parametric study of isentropic nozzle performance

One measure of cold spray nozzle performance is the maximum attainable particle velocity at the nozzle exit (Jodoin (2002) and Grujicic *et al.* (2003)). In order to calculate the particle velocity at the exit a nozzle, the drag law is used to estimate the forces acting on a particle coupled with the one dimensional isentropic relations for modelling the gas dynamics. This model makes a number of assumptions such as the gas being isentropic and the particle being perfectly spherical. To solve the governing equation, a time marching scheme is used to track the particle velocity as it travels along the nozzle for a given set of initial condition. The drag acting on the particle is expressed as:

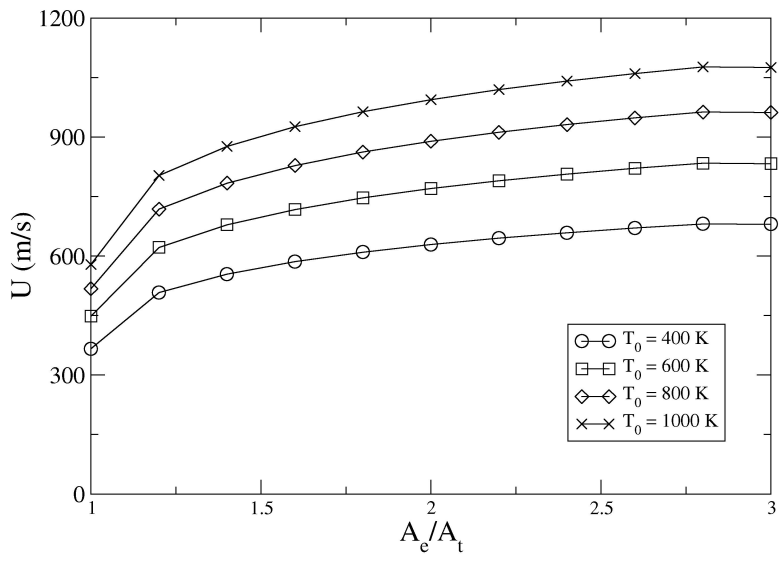
$$F_D = m_p \frac{du_p}{dt} = \frac{1}{2} \rho C_D (u - u_p) |u - u_p| A_p \quad (3.5)$$

Substituting the expression for the volume ($\frac{4}{3}\pi r_p^3$) and surface area ($4\pi r_p^2$) of a sphere, the above equation can be rewritten as

$$\frac{du_p}{dt} = \frac{3}{4} \left(\frac{\rho}{\rho_p D_p} \right) C_D (u - u_p) |u - u_p| \quad (3.6)$$



(a) Shocked nozzle.



(b) Supersonic nozzle

FIGURE 3.3: Gas velocity at the nozzle exit for flow through a (a) shocked and (b) supersonic de-Laval nozzle.

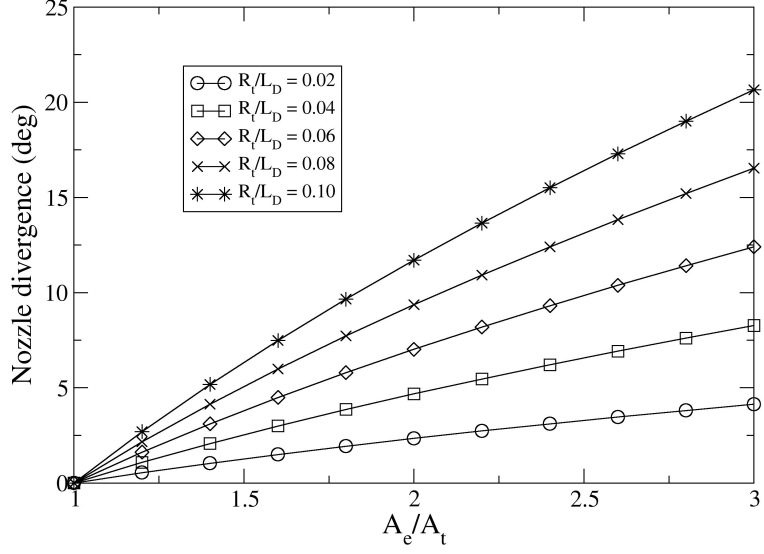


FIGURE 3.4: Nozzle divergence angle assuming a linear variation in nozzle diameter between the throat and exit.

Given the initial particle velocity, Equation.3.6 can be solved using a time marching scheme of the form

$$u_p^{n+1} = u_p^n + \frac{3}{4} \left(\frac{\rho^n \Delta t}{\rho_p D_p} \right) C_D (u^n - u_p^n) |u - u_p| \quad (3.7)$$

By definition of the particle acceleration, the particle axial location is defined by

$$x_p^{n+1} = x_p^n + \Delta t u_p^n \quad (3.8)$$

and the scheme continues marching until the particle reaches the nozzle exit.

The local gas velocity and density can be calculated using the isentropic relations and the nozzle chamber conditions

$$\begin{aligned} \rho^n &= \rho_0 / \left(1 + \frac{1}{2}(\gamma - 1)Ma^2 \right)^{\frac{1}{\gamma-1}} \\ u^n &= Ma \sqrt{\gamma R (T_0 / (1 + \frac{\gamma-1}{2}(\gamma-1)Ma^2))} \end{aligned} \quad (3.9)$$

The local Mach number is given by the expansion ratio (see Section.3.1.1). For a sphere experiencing compressibility effects, the drag coefficient is defined by Carlson & Hoglund (1973) as

$$C_{D0} = \begin{cases} \frac{24}{Re_p}(1 + 1/6Re_p^{2/3}) & \text{if } Re_p < 1000 \\ 0.44 & \text{if } Re_p > 1000 \end{cases} \quad (3.10a)$$

$$C_D = C_{D0} \left[1 + exp \left(\frac{-0.427}{Ma_p^{4.63}} - \frac{3}{Re_p} \right) \right] \quad (3.10b)$$

where the particle Reynolds and Mach numbers are defined as $Re_p = \frac{\rho|u-u_p|d_p}{\mu}$ and $\frac{|u-u_p|}{\sqrt{\gamma RT}}$ respectively.

Before extracting any data from the isentropic model, the effect of the initial particle velocity using an integration time step of 1×10^{-6} is examined in Figure.3.5. It can be seen that an increase in the initial velocity has little effect on the nozzle exit particle velocity as its diameter is increased. The next step is to validate the accuracy of the model by comparing the calculated particle velocity with the experimental measurements shown in Figure.3.6. The nozzle conditions are listed above the figures and the particles, in this case Copper, are injected from rest at the nozzle inlet. The incorporation of compressibility effects in the drag coefficient is evident from the higher particle velocities at the nozzle exit and a closer fit to the experimental data. Both graphs show a steady increase in the exit particle velocity as the nozzle chamber heats up. Although a validation of the non-isentropic model derived in Section.3.1.3 would have been instructional, the nozzle wall roughness was not specified in Phani *et al.* (2008) to allow a direct comparison.

For the preliminary study on cold spray nozzles, an Aluminium particle ($\rho_p = 2700$ kg/m³) is injected from rest into the Nitrogen carrier gas at the nozzle throat and accelerated along a diverging section with a linearly increasing diameter. The nozzle is underexpanded ($P_e/P_a > 1.0$) with an expansion ratio of 1.6 and diverging length of 10 cm. For the converging nozzle (Kinetic Metallization process), a particle is injected at the nozzle throat (exit) with a constant diameter barrel attached at the end. The effect of the nozzle chamber temperature and pressure are shown in Figures.3.7 and 3.8 respectively. The effect of a change in the nozzle diverging length (de-Laval nozzle) and barrel length (converging nozzle) is plotted in Figure.3.9. Finally, the influence of the particle density and nozzle expansion ratio is highlighted in Figure.3.10. The particle sizes used in this study are $D_p = 5, 10, 15, 20, 25, 30, 35, 40, 45$ and $50 \mu\text{m}$.

$$T_0 = 800 \text{ K} ; P_0 = 2.1 \text{ MPa} ; A_e/A_t = 1.6 ; L_D = 10 \text{ cm}$$

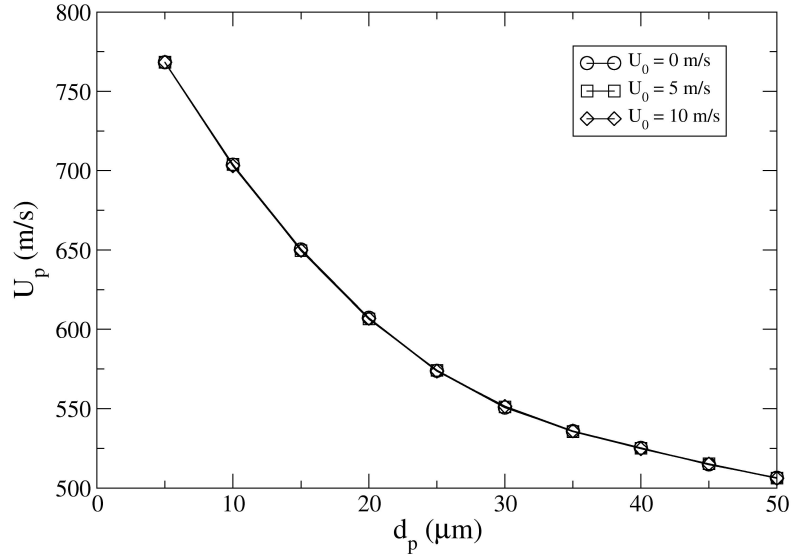


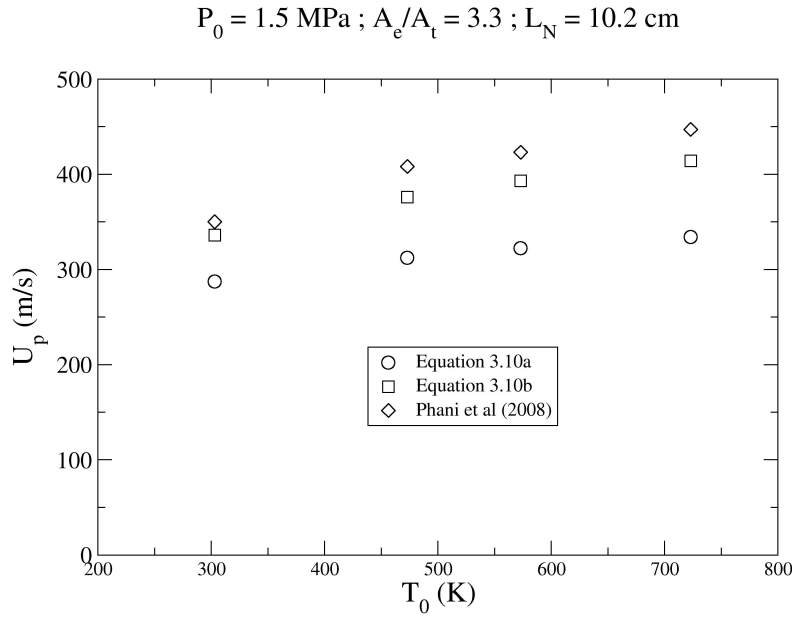
FIGURE 3.5: Effect of the initial particle velocity on the calculated velocity at the nozzle exit.

3.1.3 Effect of attaching a barrel section to the nozzle

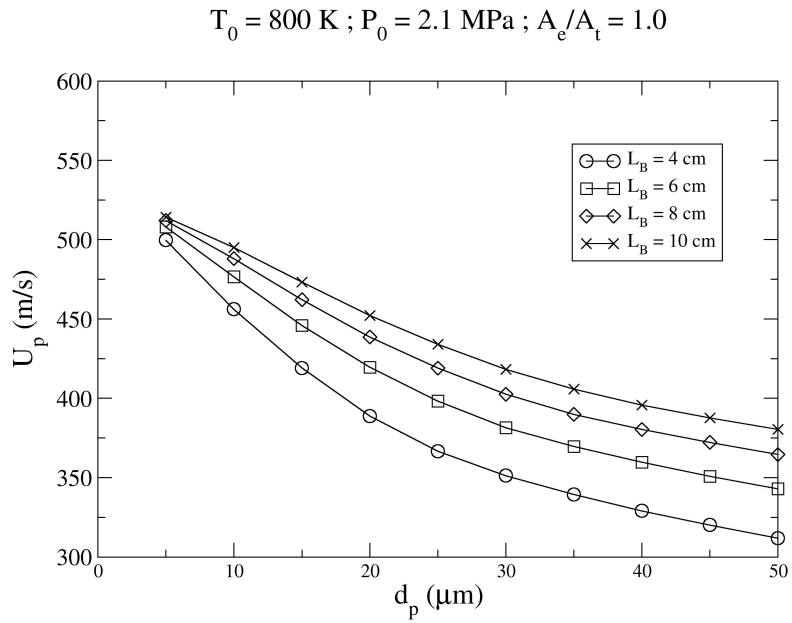
In principle, a sufficiently long nozzle will allow the particle to eventually catch up to the speed of the gas. This is usually done by increasing the nozzle diverging length but here we attach a constant diameter barrel section to the nozzle as shown in Figure.3.11. In this case, the particles are injected at the start of the barrel section (end of the nozzle) and are exposed to the nozzle exit gas velocity during their acceleration. This approach could be more efficient than injecting at the throat where the gas has yet to reach its maximum speed. To compensate for the length of the barrel, the gas can be rapidly expanded through a short nozzle section. As the streamwise pressure gradient is favourable in a supersonic nozzle, no flow separation will occur along the walls of the diverging section (White (1999)) and the effect of the thickening boundary layer will be minimal due to the short nozzle length (Alkhimov & Kosarev (2003)).

In order to calculate the particle acceleration through a constant diameter barrel section, a number of simplifying assumptions are made.

1. Steady one dimensional flow through the barrel section with no work or potential energy changes
2. Negligible heat transfer along the nozzle wall which is at the adiabatic wall tem-



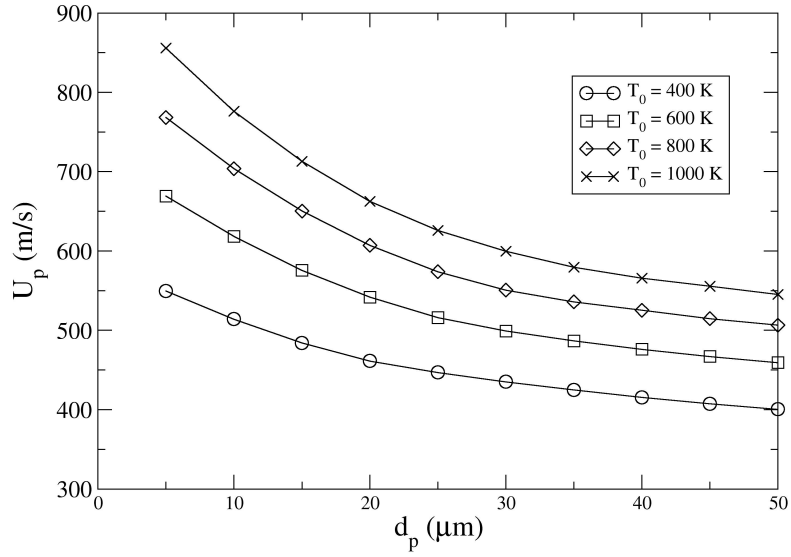
(a) $P_0 = 1.5 \text{ MPa}$.



(b) $P_0 = 2.0 \text{ MPa}$.

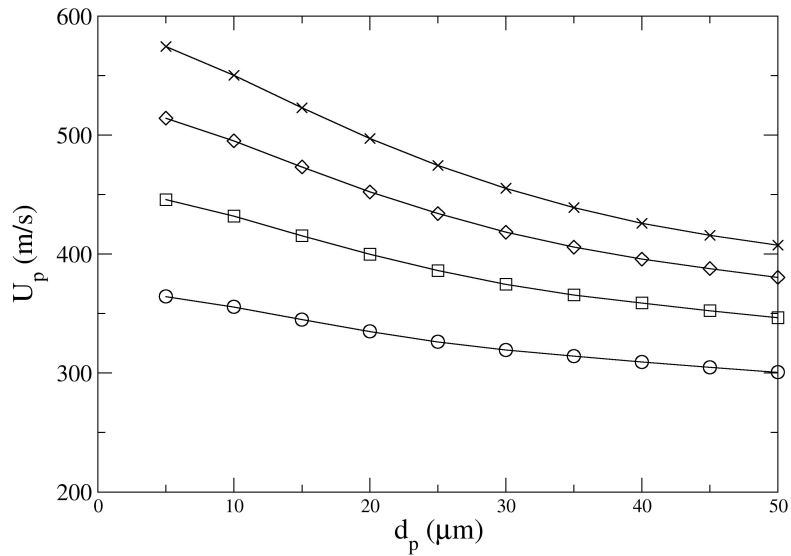
FIGURE 3.6: Comparison of calculated Copper particle ($D_p = 33\mu\text{m}$ and $\rho_p = 8910 \text{ kg/m}^3$) velocities at the nozzle exit with experimental values by Phani *et al.* (2008).

$P_0 = 2.1 \text{ MPa} ; A_e/A_t = 1.6 ; L_D = 10 \text{ cm}$



(a) Cold spray nozzle.

$P_0 = 2.1 \text{ MPa} ; A_e/A_t = 1.0 ; L_B = 10 \text{ cm}$



(b) Kinetic metallization nozzle

FIGURE 3.7: Effect of the nozzle chamber temperature on the particle velocity at the exit of an isentropic cold spray nozzle.

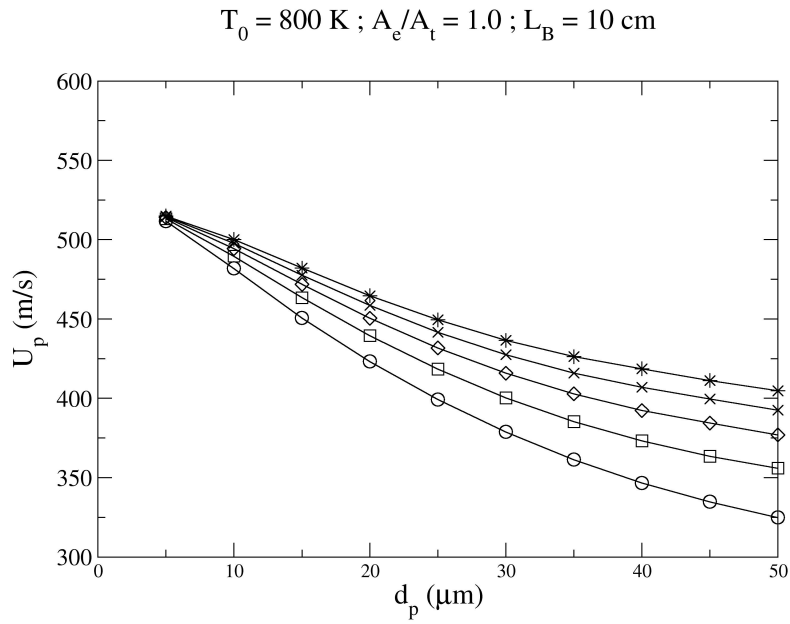
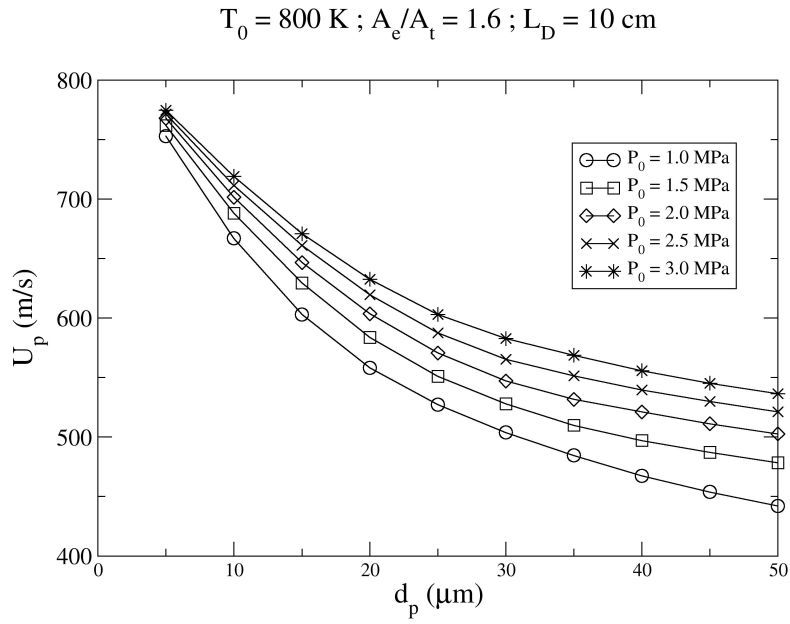
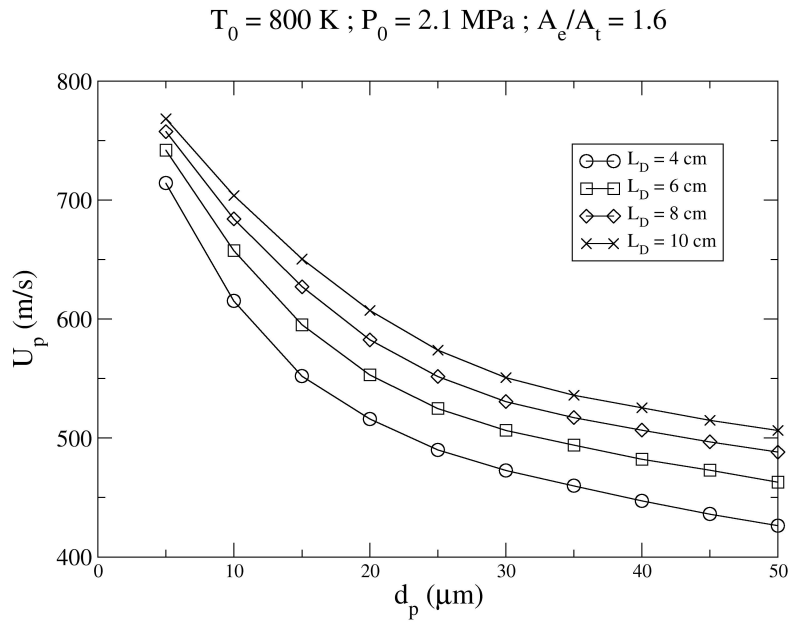
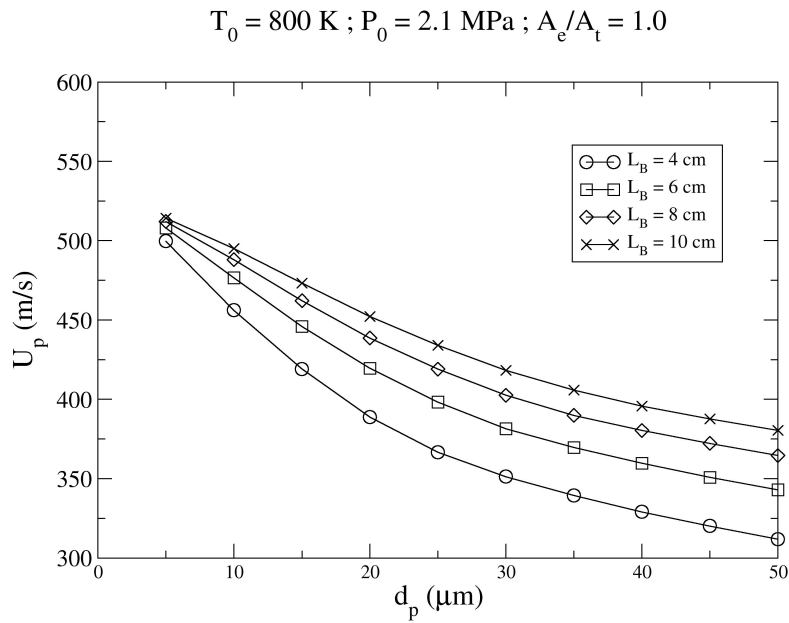


FIGURE 3.8: Effect of the nozzle chamber pressure on the particle velocity at the exit of an isentropic cold spray nozzle.



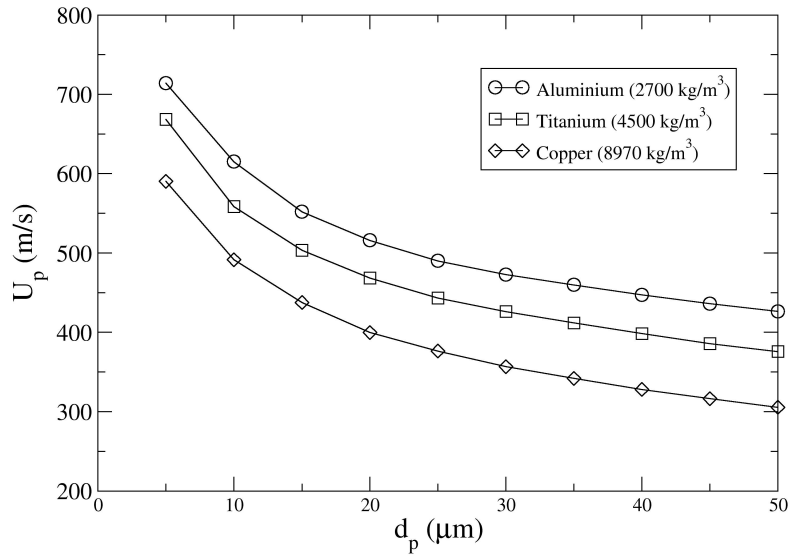
(a) Cold spray nozzle.



(b) Kinetic metallization nozzle

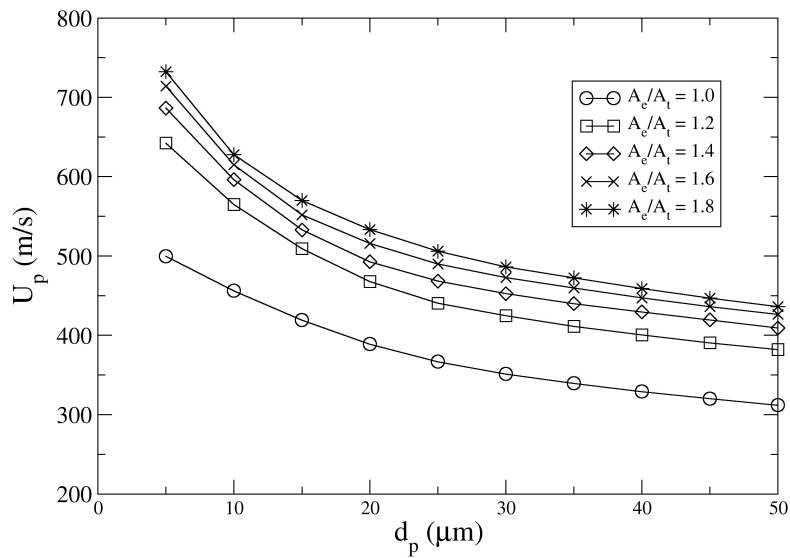
FIGURE 3.9: Effect of the (a) diverging and (b) barrel length on the particle velocity at the exit of an isentropic cold spray nozzle.

$T_0 = 800 \text{ K}$; $P_0 = 2.1 \text{ MPa}$; $A_e/A_t = 1.6$; $L_D = 10 \text{ cm}$



(a) Effect of particle density.

$T_0 = 800 \text{ K}$; $P_0 = 2.1 \text{ MPa}$; $L_B = 10 \text{ cm}$; $L_D = 10 \text{ cm}$



(b) Effect of nozzle expansion ratio.

FIGURE 3.10: Effect of the particle density and nozzle expansion ratio on the particle velocity at the exit of an isentropic cold spray nozzle.

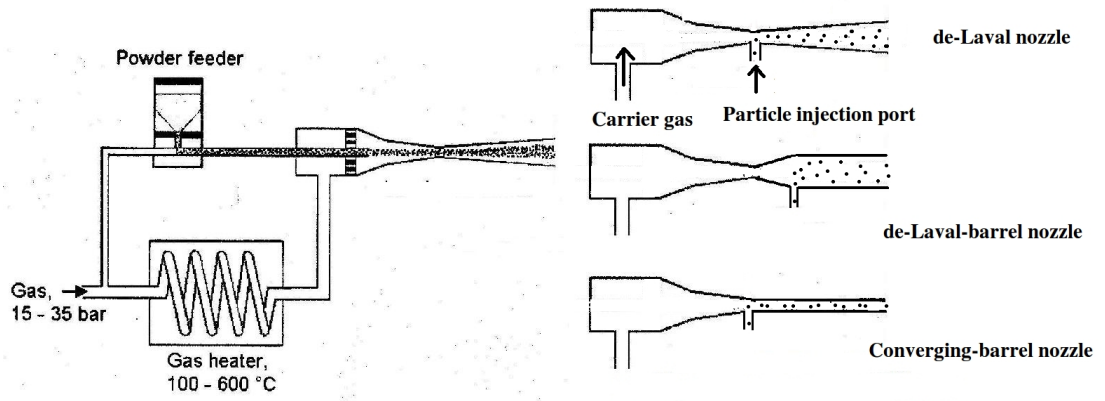


FIGURE 3.11: Schematic representation of cold spray nozzles with and without a barrel attached section at the end. (Adapted from Sandia National laboratory website)

perature

3. Constant wall friction along the diverging and barrel sections u
4. Supersonic wall friction factor is approximately half the subsonic value for a given Reynolds number (Shapiro (1953))
5. Decrease in the effective nozzle cross section area due to the presence of a boundary layer is minimal

When a barrel section is attached to a nozzle, the flow analysis is analogous to that of a turbulent pipe flow problem (White (1999)) except with larger changes in kinetic energy, enthalpy and pressure. The key parameter is the inlet Mach number which tends to approach a value of one downstream. Because the maximum entropy occurs at $Ma = 1.0$, the second law of thermodynamics requires that the flow approach sonic conditions from either subsonic or supersonic inlet conditions. It can be shown for a barrel with an inlet speed of Ma_{inlet} that the distance required (L_{crit}) by friction to drive the flow to sonic conditions is given by:

$$\frac{fL_{crit}}{D} = \frac{1 - Ma_{inlet}^2}{\gamma Ma_{inlet}} + \frac{\gamma + 1}{2Ma_{inlet}} \ln \left(\frac{(\gamma + 1)Ma_{inlet}^2}{2 + (\gamma - 1)Ma_{inlet}^2} \right) \quad (3.11)$$

For barrels with a supersonic inlet, the exit conditions will be supersonic if the barrel length is shorter than the critical length. If the barrel length exceeds the critical length, the flow upstream will adjust itself so that the flow at the exit is at sonic conditions. Similarly for barrels attached to a choked converging nozzle, the nozzle

throat (exit) conditions will be adjusted so that the flow at the barrel exit is at sonic conditions.

In practice, an average friction factor f is assumed along the length of the barrel. The friction factor may be estimated from the Moody chart (Figure.3.12) using the average Reynolds number ($Re = \frac{\rho V D}{\mu}$) and wall roughness ratio ($\frac{\epsilon}{D}$). Experimental measurements by Shapiro (1953) indicate that the friction factor for supersonic duct flow is half the magnitude of an incompressible flow with the same Reynolds number. The supersonic nozzle used in the present investigation has an expansion ratio of 1.6 which gives an average gas speed of around 650 m/s in the barrel section. A rough estimate for the Reynolds number assuming this gas speed and a diameter of 1 cm is somewhere of the order of 5×10^6 . Reading off the Moody chart, this results in a barrel with a compressible friction factor of about 0.004.

In order to estimate the local non-isentropic gas velocity and density in the barrel section, Equation.3.11 is recast into the following form in which the local gas Mach number (Ma) varies with distance from the barrel inlet (x).

$$\frac{f(L_{crit} - x)}{D} = \frac{1 - Ma^2}{\gamma Ma} + \frac{\gamma + 1}{2Ma} \ln \left(\frac{(\gamma + 1)Ma^2}{2 + (\gamma - 1)Ma^2} \right) \quad (3.12)$$

For the present study, the barrel inlet flow conditions are defined by those at the exit of the underexpanded de-Laval nozzle. As the gas travels downstream from the inlet, the variable $\frac{f(L_{crit}-x)}{D}$ is reduced and the local Mach number is obtained by linear interpolation of tabulated values of Equation.3.12. The gas velocity and density is needed to estimate the particle drag (Equation.3.7) and these can be calculated with respect to the barrel sonic conditions (s) using Equation.3.13. For example, to extract the physical value of the local density $\rho = \rho_e \frac{\rho/\rho_{sonic}}{\rho_e/\rho_{sonic}}$, the variable ρ_e and the ratios ρ/ρ_{sonic} and ρ_e/ρ_{sonic} are needed. The former is defined by the nozzle exit density while the latter ratios can be calculated using Equation.3.13 given the local Mach number (Ma).

$$\frac{\rho}{\rho_{sonic}} = \frac{u_{sonic}}{u} = \sqrt{\frac{\gamma + 1}{Ma(2 + (\gamma - 1)Ma^2)}} \quad (3.13)$$

The variation in particle velocity along a constant diameter barrel section attached to a supersonic nozzle with an expansion ratio of 1.6 and throat diameter of 1 cm is

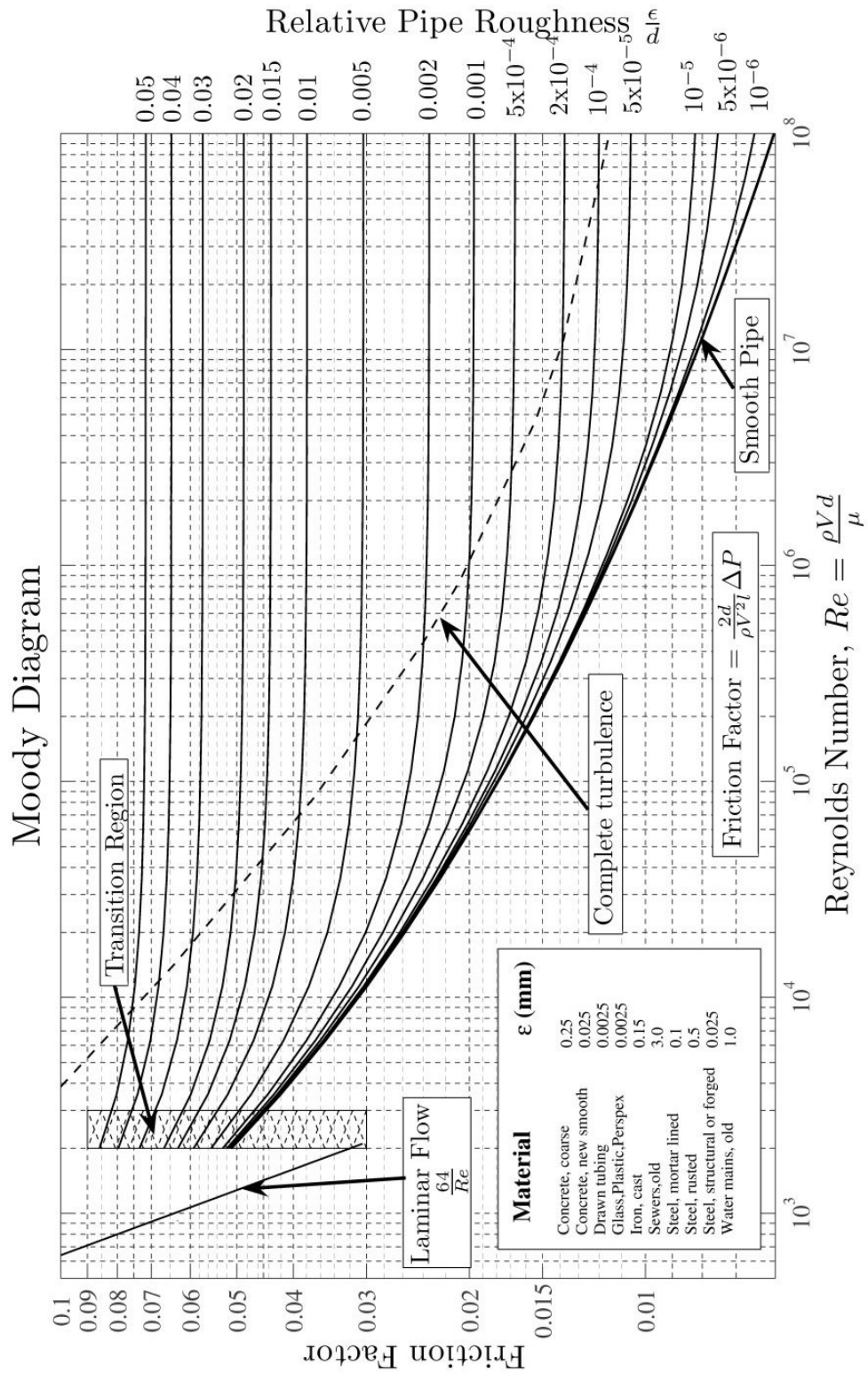


FIGURE 3.12: The Moody chart for pipe flow with smooth and rough walls.

$$P_0 = 2.1 \text{ MPa} ; T_0 = 800 \text{ K} ; A_e/A_t = 1.6$$

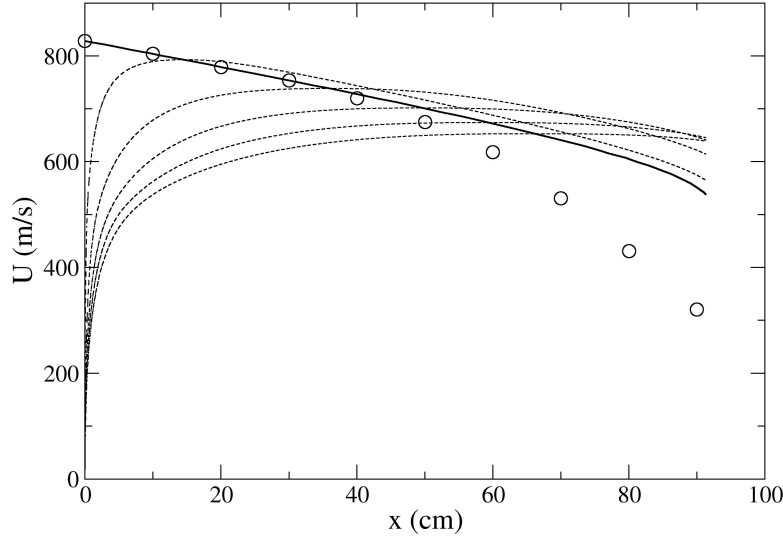
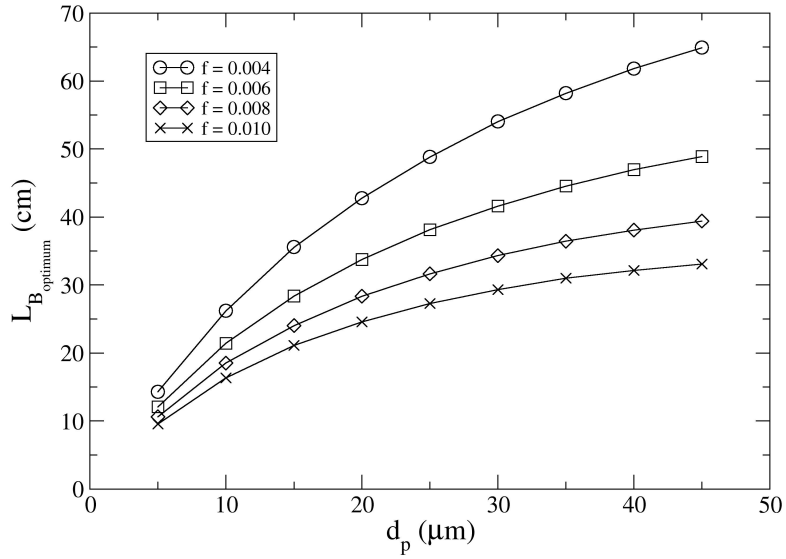


FIGURE 3.13: Supersonic particle velocity variation through a barrel section with $f = 0.004$. The solid line represents the gas velocity and the broken lines represent the particle velocities. The arrow indicates the direction of increasing particle diameters of 5, 15, 25, 35 and 45 μm . The circles represent the gas velocity computed using FLUENT.

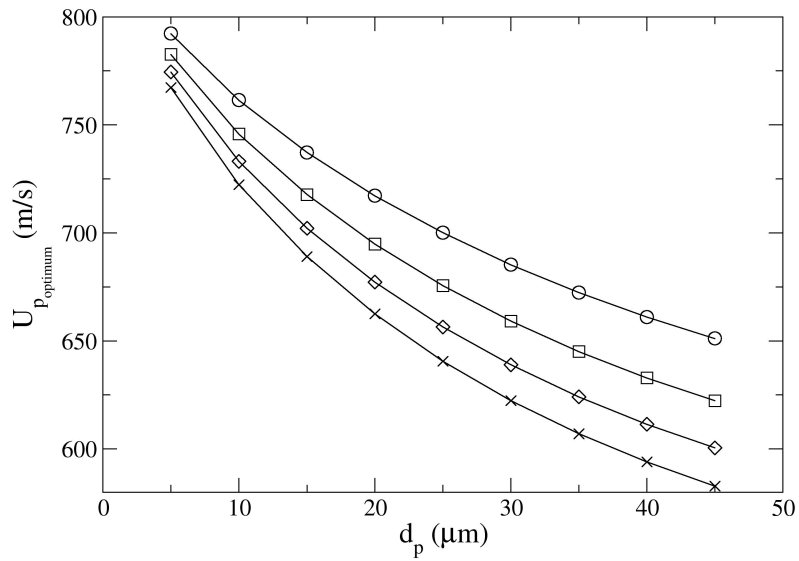
shown in Figure.3.13. The barrel inlet conditions are calculated assuming isentropic flow through the nozzle and a barrel length of $L_{crit} = 90 \text{ cm}$. The theoretical gas velocity was compared with data computed using FLUENT. It can be seen that the deviation between the theoretical and computational results becomes apparent after a distance of $x/D \simeq 60$. This observation supports the theoretical results of Alkhimov & Kosarev (2003) which states that nozzles with a diameter to length ratio (D/L) of less than approximately 0.02 experience merging of the boundary layers at the exit. Consequently, the assumption of a constant diameter barrel section is no longer valid for x/D greater than 60 and the particle velocity calculation beyond this point becomes less reliable. Nevertheless, Figure.3.13 displays a trend that as the particle size increases, its maximum velocity occurs further downstream from the inlet. The distance between the barrel inlet and this point is defined as the optimum barrel length and is plotted in Figure.3.14 for different particle sizes. This length will later be used to compare the particle acceleration through the barrel and diverging sections. The particle sizes used in this study are $D_p = 5, 10, 15, 20, 25, 30, 35, 40$ and $45 \mu\text{m}$.

$P_0 = 2.1 \text{ MPa} ; T_0 = 800 \text{ K} ; A_e/A_t = 1.6$



(a) Optimum barrel length.

$P_0 = 2.1 \text{ MPa} ; T_0 = 800 \text{ K} ; A_e/A_t = 1.6$



(b) Maximum particle velocity.

FIGURE 3.14: (a) Optimum barrel length required to achieve (b) maximum particle velocity through a barrel attached to a supersonic nozzle with $A_e/A_t = 1.6$.

3.1.4 Particle acceleration through the nozzle diverging section

To model the non-isentropic gas flow in the diverging section of the nozzle, Equation.3.11 is no longer applicable as it doesn't account for streamwise variation in the barrel cross sectional area. The governing equations for compressible flow through a duct of variable area are derived in Appendix.C.

$$\begin{aligned}
 \left(\frac{A}{A_t} \right) &= \left[Ma^{A_1/2} \left(\frac{1+k_2Ma^2}{1+k_2} \right)^{B_1/k_2} \left(\frac{k_3Ma^2-k_1}{k_3-k_1} \right)^{C_1/k_3} \right]^{2k_1} \\
 \frac{\rho}{\rho_t} &= \left(\frac{1+k_2Ma^2}{1+k_2} \right)^{A_2/k_2} \left(\frac{k_3Ma^2-k_1}{k_3-k_1} \right)^{B_2/k_2} \\
 \frac{u}{u_t} &= Ma \sqrt{\frac{1+k_2}{1+k_2Ma^2}}
 \end{aligned} \tag{3.14}$$

where D_e and D_t are the nozzle exit and throat diameters and L_d is the diverging length with the following constants.

$$\begin{aligned}
 k_1 &= \frac{D_e - D_t}{L_d} & k_2 &= \frac{\gamma - 1}{2} & k_3 &= \gamma f \\
 A_1 &= -\frac{1}{k_1} & B_1 &= \frac{k_2(k_2 + k_1)}{4(k_1k_2 + k_3)} & C_1 &= \frac{k_3(k_3 - k_1)}{4k_1(k_3 + k_2k_1)} \\
 A_2 &= \frac{-k_2(k_1 - k_3)}{2(k_1k_2 + k_3)} & B_2 &= \frac{k_3(k_1 - k_3)}{2(k_3 + k_1k_2)} \\
 A_3 &= 2(1 - \gamma) & B_3 &= k_2^2
 \end{aligned} \tag{3.15}$$

As a particle travels along the diverging section, the nozzle expansion ratio increases and the Mach number is obtained using linear interpolation of tabulated values of Equation.3.12. The remaining flow variables needed to solve Equation.3.7 can be calculated using Equation.3.13 once the local Mach number is known. Figure.3.15 shows the acceleration of air through a diverging section with an expansion ratio of 1.6, throat diameter of 1.0 cm and diverging length of 10 cm. It can be seen that an increase in nozzle wall friction produces a substantial decrease in the exit gas velocity when compared to an isentropic nozzle. To clarify this further, Figure.3.16 plots the effect of the diverging length and friction factor on the exit gas velocity. As the diverging section shortens, the exit gas velocity approaches an isentropic value of 821 m/s. This observation justifies an earlier assumption which states that the barrel inlet conditions can

be approximated using the isentropic relations provided that the diverging section of the de-Laval nozzle is short (see Section.3.1.3).

In order to delineate the benefits of attaching a barrel section to a de-Laval nozzle, a particle is accelerated through a diverging and barrel section of equal length defined by the optimum barrel length shown in Figure.3.14. For example, a particle with a diameter of 30 μm would be accelerated through a 50 cm long diverging and barrel section as this corresponds to the optimum barrel length assuming $f = 0.004$. For a nozzle with a barrel attached at the end, the particle is injected at the start of the barrel section (see Figure.3.11) and for one without, the injection occurs at the nozzle throat. The results shown in Figures.3.17 and 3.18 are for an isentropic barrel section (i.e. constant nozzle exit velocity) and those in Figures.3.19 and 3.20 are for a non-isentropic barrel section. With an expansion ratio of 1.6, the nozzle throat and exit diameters (also the barrel diameter) are 1.0 and 1.3 cm respectively.

It would also be interesting to see what effect a barrel section has attached to the end of a converging nozzle. For reasons discussed previously, the throat of the converging nozzle will no longer be choked as the gas accelerates from subsonic to sonic speed in the barrel section. Equations.3.12 and 3.13 are used to estimate the local gas velocity and density but with subsonic Mach numbers corresponding to the variable $\frac{f(L_{crit}-x)}{D}$. Figure.3.21 plots the gas and particle velocity through a 10 cm long barrel attached to what should have been an underexpanded converging nozzle. The barrel friction factor is assumed to be higher ($f = 0.008$) considering that the average gas velocity is substantially lower than the one attached to the de-Laval nozzle. Since the maximum velocity occurs at the barrel exit, the optimum barrel length is fixed at 10 cm for all particle sizes. In order to examine the effect of the nozzle chamber conditions, a barrel with a diameter of 1 cm is used in both isentropic (i.e. constant Mach number of unity in the barrel) and non-isentropic calculations shown in Figures.3.22 and 3.23 respectively.

3.1.5 Discussion of results

The data generated in the previous section will now be examined in the context of nozzle design and performance. First, a comparison between the gas velocity produced by a supersonic and choked subsonic nozzle is presented. Next, the effect of the nozzle chamber conditions and geometry on the maximum particle velocity achieved during

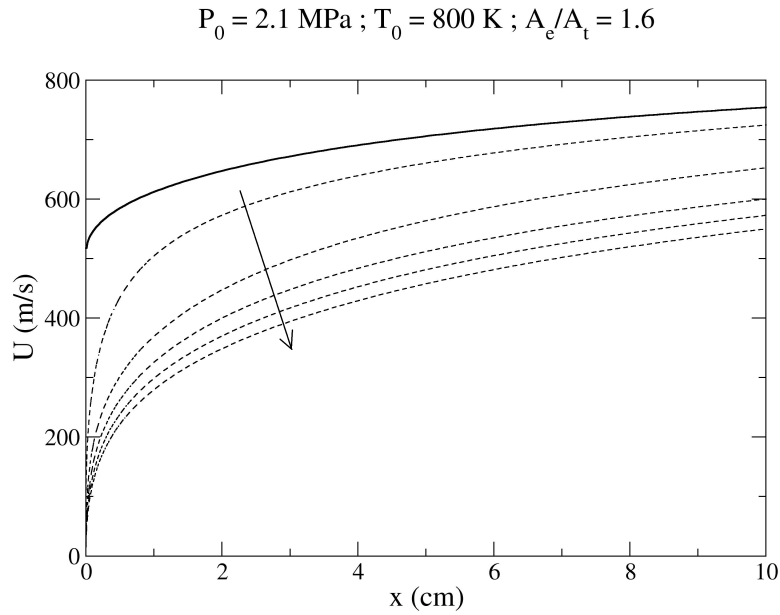


FIGURE 3.15: Gas velocity variation through a supersonic diverging section with $A_e/A_t = 1.6$. The solid line represents an isentropic flow ($f = 0.0$) and the arrow indicates the direction of increasing friction factors of $f = 0.004, 0.006, 0.008$ and 0.010 .

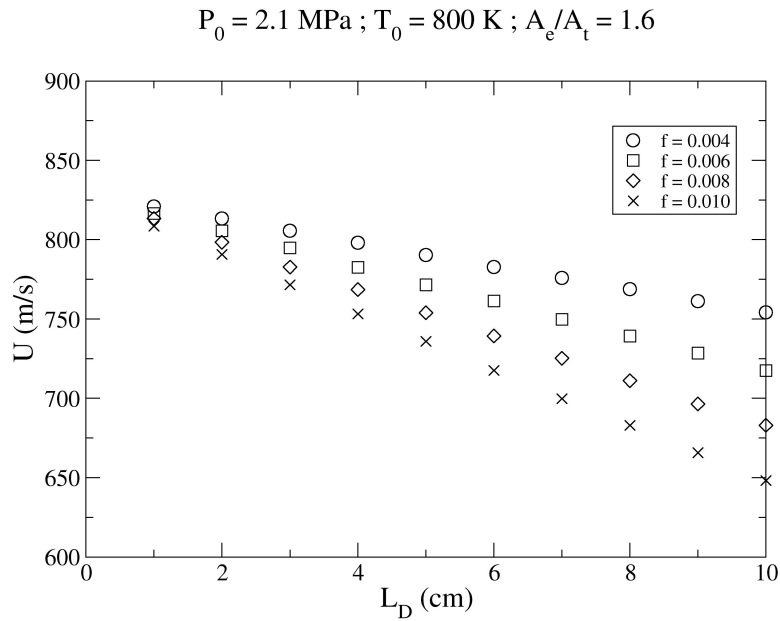


FIGURE 3.16: Exit gas velocity as a function of nozzle diverging length (L_D) for an expansion ratio of $A_e/A_t = 1.6$.

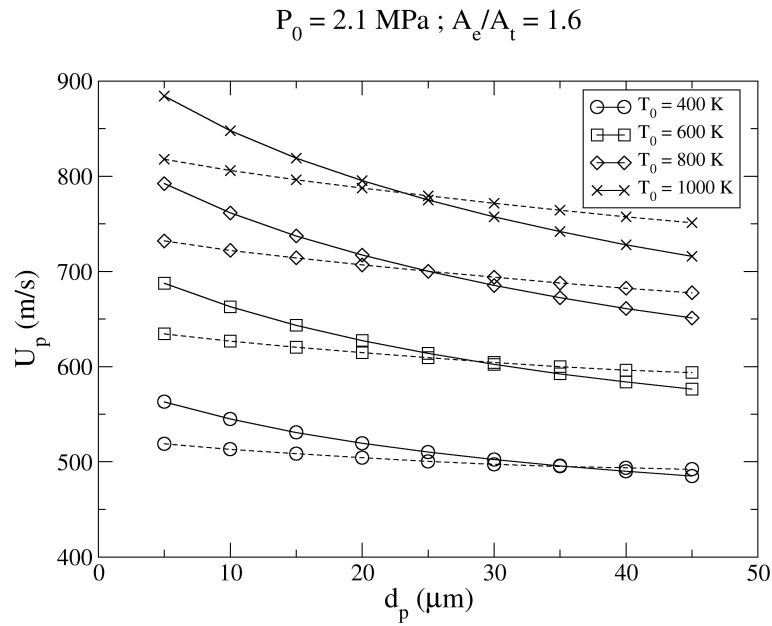


FIGURE 3.17: Effect of the nozzle chamber temperature on the particle velocity at the exit of a de-Laval nozzle. Solid and dashed lines represent cases with and without a non-isentropic barrel section ($f = 0.004$) respectively.

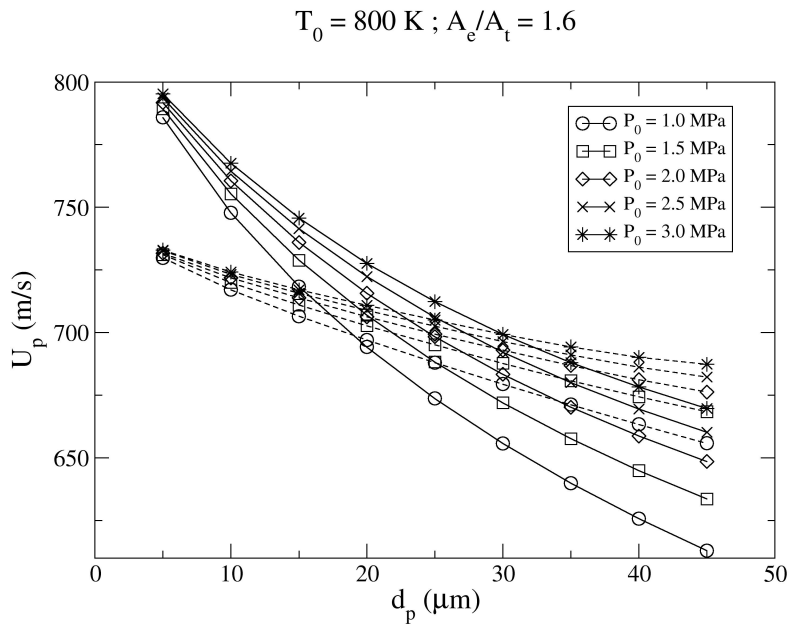


FIGURE 3.18: Effect of the nozzle chamber pressure on the particle velocity at the exit of a de-Laval nozzle. Solid and dashed lines represent cases with and without a non-isentropic barrel section ($f = 0.004$) respectively.

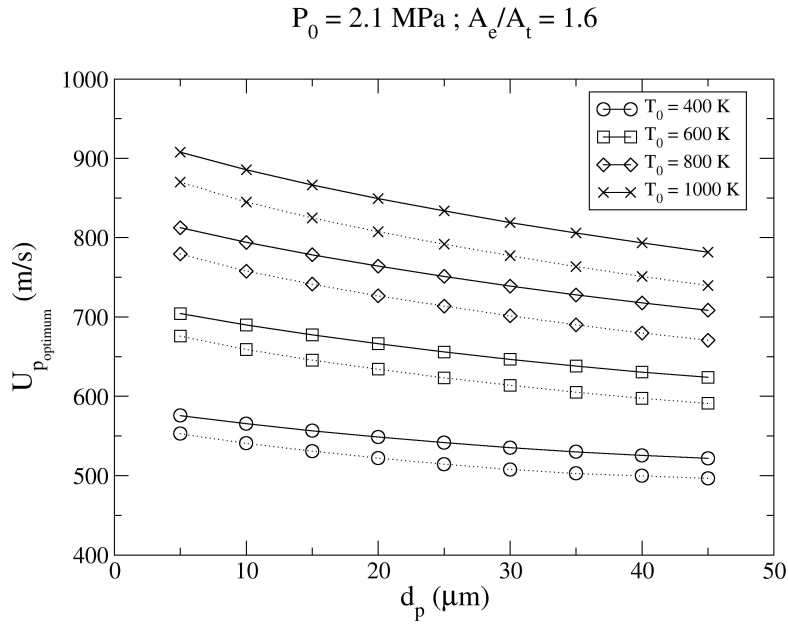


FIGURE 3.19: Effect of the nozzle chamber temperature on the particle velocity at the exit of a de-Laval nozzle. Solid and dashed lines represent cases with and without an isentropic barrel section ($f = 0.0$) respectively

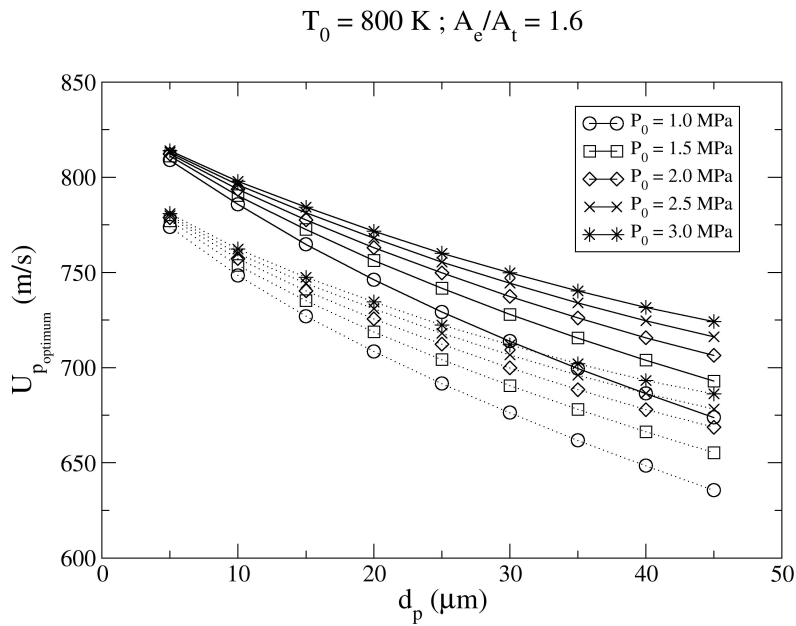


FIGURE 3.20: Effect of the nozzle chamber pressure on the particle velocity at the exit of a de-Laval nozzle. Solid and dashed lines represent cases with and without an isentropic barrel section ($f = 0.0$) respectively

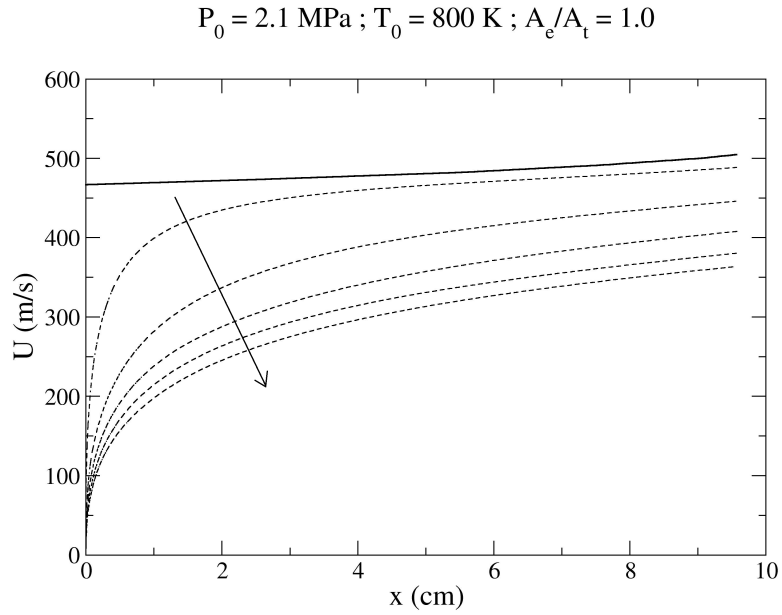


FIGURE 3.21: Subsonic particle velocity variation through a barrel with $f = 0.008$. The solid line represents the gas velocity and the broken lines represent the particle velocities. The arrow indicates the direction of increasing particle diameters of 5, 15, 25, 35 and 45 μm .

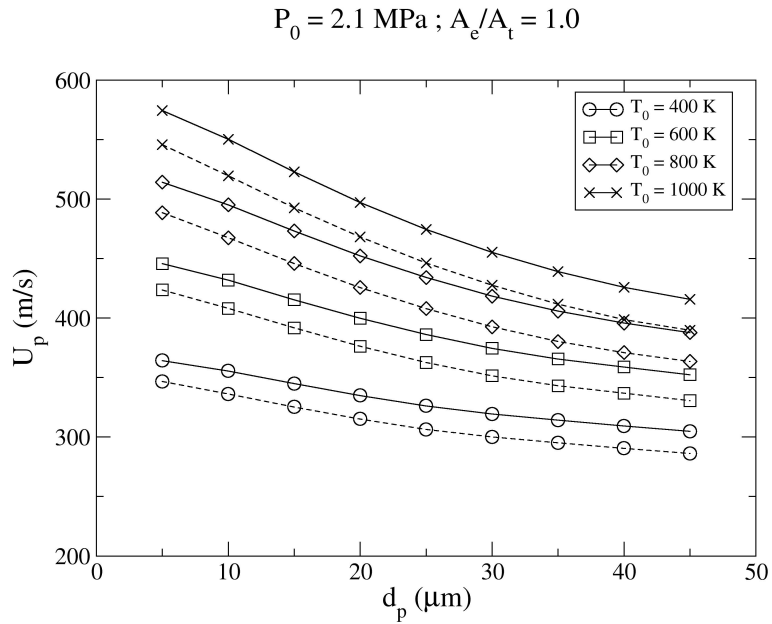


FIGURE 3.22: Effect of the nozzle chamber temperature on the particle velocity at the exit of a converging nozzle with a barrel attached. Solid and dashed lines represent cases with an isentropic ($f = 0.0$) and non-isentropic ($f = 0.008$) barrel section respectively.

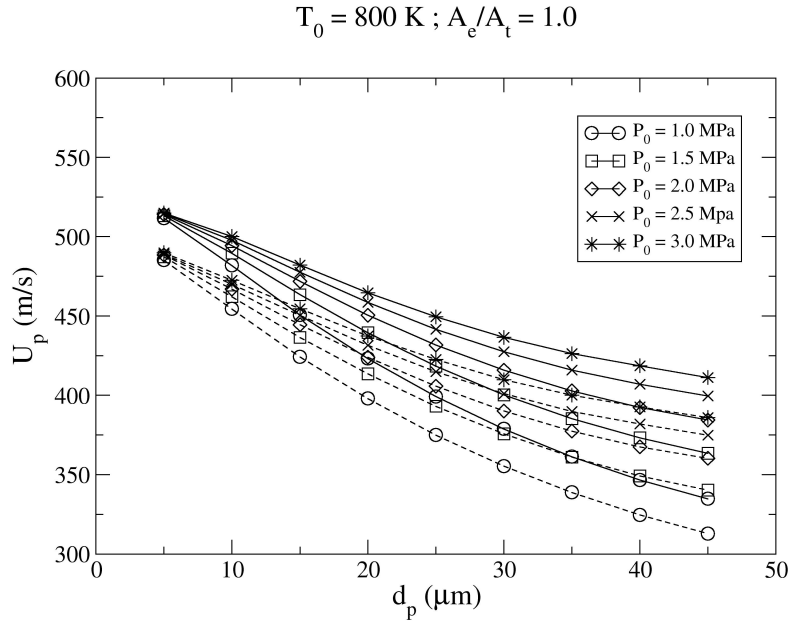


FIGURE 3.23: Effect of the nozzle chamber pressure on the particle velocity at the exit of a converging nozzle with a barrel attached. Solid and dashed lines represent cases with an isentropic ($f = 0.0$) and non-isentropic ($f = 0.008$) barrel section respectively.

both cold spray and kinetic metallization processes is commented upon. Finally, the benefits of attaching a barrel section to the end of a cold spray nozzle is discussed. The inclusion of wall friction in the theoretical model is seen to generate substantial differences from the isentropic model.

Cold spray nozzle design

Figure.3.1 delineates the nozzle chamber pressure required for shocked (i.e with a normal shock at the exit) and supersonic nozzle flow as well as the corresponding Mach number at the nozzle exit. The plot also highlights the rapid increase in chamber pressure required to produce an underexpanded nozzle with a large expansion ratio. On the other hand, only 0.2 MPa is required in the nozzle chamber to produce an overexpanded jet. Hence, it is comes as no surprise that the majority of nozzles employed in cold spray have been overexpanded (see Section.1.1). Figure.3.2 shows that below a chamber pressure of 100 kPa, the nozzle is subsonic throughout regardless of the expansion ratio.

The effect of the nozzle chamber temperature on the nozzle exit gas velocity is shown in Figure.3.3 for both shocked and supersonic nozzle flow. Although the exit Mach number remains unchanged for nozzles of the same expansion ratio, the physical

velocity ($u = \sqrt{\gamma RT}$) is a function of the local temperature which in turn is governed by the chamber temperature. It can be seen that despite the presence of a standing shock at the nozzle exit, the velocity of the gas leaving the nozzle can still be quite high given sufficient nozzle chamber temperature. The major difference between the shocked and supersonic nozzle is that the gas velocity decreases with increasing expansion ratio in the former case while increasing with the expansion ratio in the latter case. Hence, the increase in gas velocity due to the use of a supersonic nozzle becomes apparent for large nozzle expansion ratios. The nozzle divergence angle assuming a linear variation in diameter between the throat and exit is plotted in Figure.3.4. It highlights the effect of the nozzle 'slenderness ratio' on the divergence angle at large expansion ratios.

Parametric study of nozzle performance

For the parametric study, an Aluminium particle ($\rho_p = 2700 \text{ kg/m}^3$) is injected from rest into the de-Laval nozzle throat. For the kinetic metallization process, the particle is injected at the converging nozzle exit and accelerated through a constant diameter barrel section as shown in Figure.3.11. The main parameters being investigated are the nozzle chamber pressure and temperature, the nozzle length and expansion ratio.

For an underexpanded isentropic nozzle, the effect of the nozzle chamber temperature and pressure on the exit particle velocity are shown in Figures.3.7 and 3.8 respectively. In agreement with Dykhuizen & Smith (1998), both plots shows that the particle velocity at the nozzle exit decreases with increasing particle size. One thing to note is that an increase in the nozzle chamber temperature appears to be slightly less effective in boosting the velocity of large particles than it is for smaller ones. This observation is reversed by increasing nozzle chamber pressure. For particles in the range of $5 \mu\text{m} < D_p < 20 \mu\text{m}$, an increase in the nozzle chamber pressure has little effect on the exit velocity. However, once the particle diameter exceeds $20 \mu\text{m}$, the increase in pressure starts to have a significant impact on the exit velocity.

The consequences of increasing the nozzle diverging length is plotted in Figure.3.9 and it has a similar effect to that of the nozzle chamber pressure. The difference is that it takes a diverging section only twice as long to produce the same amount of increase in particle velocity as a threefold increase in the chamber pressure. Finally, the influence of the particle density and nozzle expansion ratio is shown in Figure.3.10. Among three of the most commonly used coating materials, Aluminium, which has the

lowest density, produces the highest exit velocity. The gain in particle velocity due to acceleration through a nozzle diverging section is evident compared to that through a constant diameter barrel section attached to a converging nozzle.

Effect of a barrel extention

For a de-Laval nozzle with a barrel section attached, the optimum barrel length and the corresponding maximum particle velocity are plotted in Figure.3.14. As the particle size increases so does the optimum length. For a barrel with $f = 0.004$, the optimum barrel needs to be over half a meter long for a particle diameter of $30 \mu\text{m}$! On the other hand, a barrel with a higher wall friction requires a shorter optimum barrel length which results in a lower maximum velocity. As the friction increases, the optimum barrel length curve begins to approach an asymptotic value for large particles. This value corresponds to the critical barrel length for a given wall friction factor and inlet speed. If the barrel were any longer, a normal shock would form upstream to adjust the flow at the exit to sonic conditions. It should be emphasised that the results for larger particles ($D_p > 40 \mu\text{m}$ and $L_D > 60 \text{ cm}$) are not as accurate due to the merging of boundary layers along the barrel and diverging sections (Alkhimov & Kosarev (2003)).

The effect of the nozzle chamber temperature and pressure on nozzles with and without a non-isentropic barrel are shown in Figures.3.17 and 3.18 respectively. The gain in particle speed due to the addition of a barrel section decreases with increasing particle size up until it becomes detrimental. However, the critical particle size ($D_p \simeq 20\text{-}25 \mu\text{m}$) for which the addition of a barrel section becomes disadvantageous can be increased by lowering the nozzle chamber temperature and increasing the pressure. On the other hand, the benefit of attaching an isentropic barrel to the nozzle is clearly delineated by the uniform increase in the exit particle velocity as shown in Figures.3.19 and 3.20. This suggests that a low friction barrel section is conducive to enhancing the overall exit velocity. This is also highlighted in the case of the converging nozzle (Figures.3.22 and 3.23) where an increase in barrel wall friction resulted in a uniform decrease in the exit particle velocity. It can also be seen that the influence of the nozzle chamber conditions are qualitatively similar for both de-Laval and converging nozzles; an increase in the nozzle chamber pressure is more effective at boosting the velocity of large particles.

Practical implications

A comprehensive study of an underexpanded cold spray nozzle has been performed in which the particle acceleration is achieved using a diverging section and a barrel section attached to the end of a de-Laval (cold spray) and converging (kinetic metallization) nozzle. The following trends have been established in relation to the particle velocity at the nozzle exit.

1. An increase in the nozzle chamber pressure and diverging length is conducive to increasing the velocity of large particles
2. An increase in the nozzle chamber temperature diminishes in effect for large particles
3. The optimum barrel length for a de-Laval-barrel nozzle increases with particle size and decreasing wall friction
4. The acceleration of particles using a de-Laval-barrel nozzle is more effective for smaller particles while a diverging section is preferred for larger particles
5. The critical particle size for which the de-Laval-barrel nozzle becomes detrimental can be varied through adjustment of the nozzle chamber conditions
6. A low friction barrel section is required to boost the velocity of a wide range of particle sizes
7. The effect of the nozzle chamber conditions are qualitatively similar for both de-Laval and converging nozzles

This concludes the parametric study of the particle and gas dynamics in the cold spray nozzle. The non-dimensionalised results and observations presented here can also be applied to an overexpanded nozzle of similar nozzle expansion ratio, chamber temperature and wall friction. The next section will look at the gas and particle dynamics outside the supersonic nozzle which may be either underexpanded or overexpanded.

3.2 Steady cold spray process

The gas and particle dynamics between the nozzle and substrate during the steady cold spray process is the focus of study in the second component of the investigation. A numerical approach was chosen for this part of the study due to the difficulties associated with extracting accurate quantitative data from compressible flows (see Lourenco & Krothapalli (1998) and Mitchell *et al.* (2009)). Previous simulations of the cold spray process have been based on limited validation and are restricted to particle injection in an overexpanded impinging jet. So far, the only way of estimating the change in particle velocity between the nozzle exit and substrate is via numerical simulation. This can be a computationally expensive process given the number of parameters that can be varied. Hence, it would also be desirable to have a theoretical model for estimating the particle impact speed.

In the present study, an underexpanded and overexpanded nozzle is deployed to accelerate the particles with operating conditions set to those used in the validation cases. This not only establishes a degree of confidence in the accuracy of the gas phase simulations but also allows a direct comparison between two supersonic nozzles with similar exit gas speeds. The particle impact statistics are extracted along the substrate to provide information on the particle impact speed, angle and location. Next, the variation in particle velocity and drag during its flight through both supersonic impinging jets is examined. Using this information, a theoretical model is proposed which backed with the sufficient experimental data can be used to approximate the particle impact speed.

The research objectives for the second component of the numerical investigation on cold spray are three fold.

1. To validate underexpanded and overexpanded impinging jet simulations using existing experimental data
2. To extract the particle impact statistics and dynamics during steady cold spray process
3. To develop and assess a theoretical model for estimating the particle impact speed

This chapter presents data extracted from simulations of the steady cold spray impinging jet flow. An assessment of the accuracy of the gas phase is performed in

TABLE 3.1: Validation cases

Case	Reference	PR	Ma_e	θ	s/D_e
A	Henderson <i>et al.</i> (2005)	2.1	1.0	0	2.1
B	Xu <i>et al.</i> (2006)	0.63	2.1	0	3.0
C	Lamont & Hunt (1980)	1.2	2.2	15	2.0
D	Lamont & Hunt (1980)	2.0	2.2	15	2.0

Section.3.2.1 using velocity and pressure measurements of supersonic impinging jets. The particle impact statistics are presented in Section.3.2.2 followed by an examination of the gas and particle dynamics between the nozzle exit and substrate in Section.3.2.3. Finally, a theoretical approach is proposed in Section.3.2.4 which may be used to estimate the particle impact speed without the need to run a full simulation.

3.2.1 Numerical validation

Before performing any simulations, it is important to first establish the accuracy of the numerical method (Yee’s TVD scheme in Section.2.3.2) using either exact solutions or more often the case, relevant experimental data. A description of the experimental setup used to obtain the benchmark data is included for every validation case. Particle Image Velocimetry was used to extract the centerline velocity profile of an underexpanded and overexpanded impinging jet issued from a converging (Case *A*) and de-Laval (Case *B*) nozzle respectively. The pressure distribution along the impingement plate of a supersonic underexpanded impinging jet (Case *C* and *D*) is also used in the numerical validation. The flow condition of the four validation cases are summarised in Table.3.1.

Planar Particle Image Velocimetry measurements

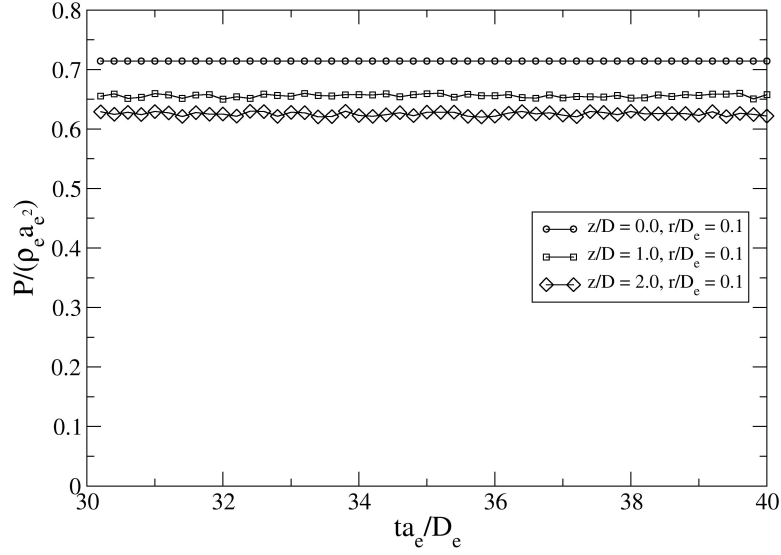
An experimental investigation into the relationship between the unsteady flow structures and the production of acoustic tones was performed by Henderson *et al.* (2005). The converging nozzle used is operating at a pressure ratio of ($PR = \frac{P_e}{P_a} = 2$), making it just strongly underexpanded (see Section.1.3). For the PIV data acquisition, the flow is seeded with 0.6 mm olive oil droplets produced by a TSI model 9306 Six-jet Atomiser. The seed injection point is located upstream of the nozzle and distributed across the entire cross section of the settling chamber. A Vicount 5000 smoke generator is used to seed the ambient air with 0.2-0.3 μm smoke particles. The particle sizes are determined from manufacturer specifications. An 80mm field of view is used for standoff distances less than 75 mm (i.e. impinging jet at $s/D_e = 2.0$) and a 136 mm field of view is used

for longer distances (i.e. free jet). For the 80 mm field of view, the particle displacement ranges between 0 and 17 pixels resulting in a error of 1.2 % for a maximum measured velocity of 550 m/s.

The PIV images are processed using PIVROC, a NASA GRC-developed code (Wernet (1999)). The processing is correlation based and allows for subregion image shifting as well as multi-pass correlation to improve the spatial resolution of the velocity vectors. The first pass of the correlation uses a subregion size of 64 x 64 pixels with 50 % overlap. The second pass uses a 32 x 32 pixel subregion size also with 50 % overlap. The resulting spatial resolutions of the velocity vector fields are 0.6 mm and 1.06 mm for the 80 mm and 136 mm field of view respectively. Despite the use of a novel processing algorithm, particle lag still occurs in regions of high velocity gradients such as in the vicinity of shocks. A careful study of the particle behavior in supersonic flows was conducted by Rossiter (1964). The particle relaxation time is found to be a strong function of the particle diameter and shock strength. Consequently, it is expected that the location of strong shocks will be smeared. Similar lagging will occur in other regions of the jet such as the wall jet region though to a lesser extent.

The convergence criteria of each simulation is defined by a pressure residual value of $P_{RMS} = \sum_i^N | \frac{P_i^n - P_i^{n+1}}{N} | = 0.0001$. Once the pressure residual history falls below this value the simulation terminates and the particles are injected across the nozzle exit. Figure.3.24 shows the pressure fluctuation at various locations in an underexpanded impinging jet. It can be seen that once the residual is less than 0.0001, there is minimal variation in pressure at several locations within the jet. The pressure at the nozzle exit $z/D_e = 0$ is fixed at $\frac{1}{\gamma} = 1/1.4 = 0.714$ by definition of the initial boundary conditions (see Section.2.5).

A grid and domain independence study for validation case *A* is shown in Figure.3.25. A uniform computational grid ($\Delta = \Delta_z = \Delta_r$) is employed in all simulations. An increase in the computational domain size (Figure.2.9) and grid resolution results in minimal changes in the jet centerline velocity profile and suggests that the solution is independent of both. The corresponding velocity contour plot clearly delineates the bow shock across which the gas eventually comes to rest at the substrate. The agreement between the experimental and numerical data is good though the calculated maximum velocity is slightly higher in the numerical simulation with the Mach disk located closer to the nozzle exit. Near the impingement region, the presence of a recirculation region



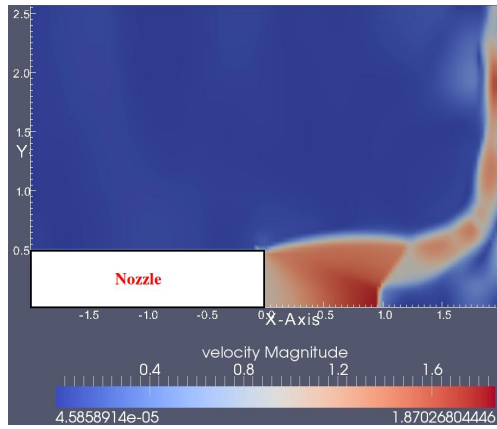
(a) Pressure residual history.

FIGURE 3.24: Pressure history of an underexpanded impinging jet operating at $PR = 2.1$ and $s/D_e = 2.08$ (Case A).

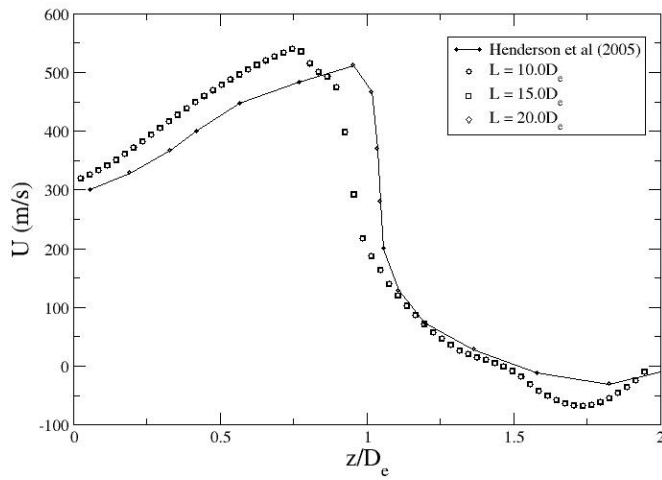
can be inferred from the negative axial velocity between $z/D_e \simeq 1.4$ and 2.0.

The experimental data for an overexpanded impinging jet is very limited and to date only Xu *et al.* (2006) has attempted to extract the planar velocity field using Particle Image Velocimetry. The ambient air is seeded with Ti_2O_3 particles with a mean diameter of 140 nm, a value which the authors argue is sufficient for capturing the shock locations. A piece of transparent glass is used to improve the resolution in the impingement region by minimising the amount of laser reflections otherwise observed using a steel plate. The nozzle used had a throat and exit diameter of 4.5 and 6 mm respectively. The experimental exit Mach number is 1.831 but the calculated value assuming isentropic flow is slightly higher at 2.1. The difference may be the result of boundary layer effects along the walls as discussed previously in Section.3.11. In the simulation, the isentropic value is assumed with a nozzle exit divergence angle of zero.

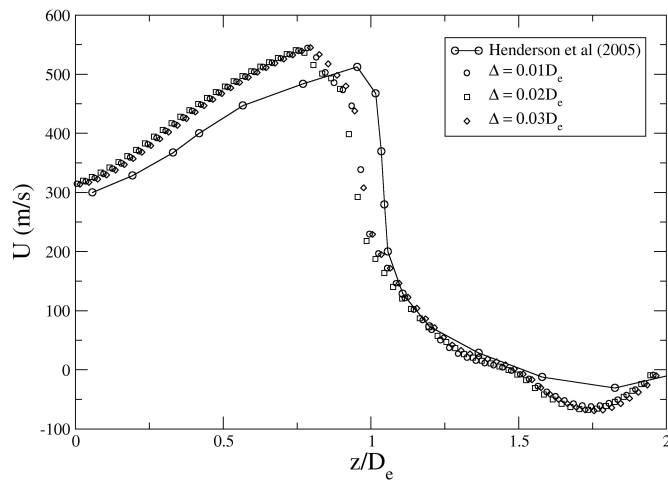
The results of a grid and domain independence study for validation case *B* is shown in Figure.3.26. An increase in the computational domain size and grid resolution resulted in minimal changes in the jet centerline velocity profile and shows that the solution is independent of both. The velocity contour plot shows a Mach reflection (re-



(a) Velocity (Ma) contour plot.

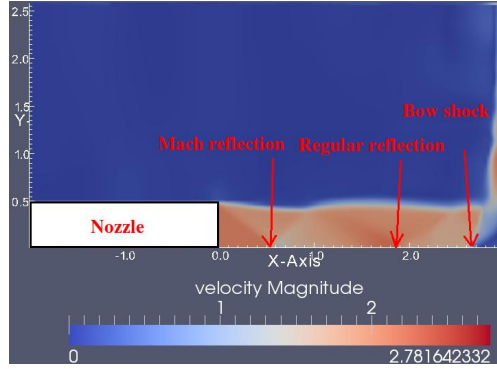


(b) Domain independence test with $\Delta = 0.01D_e$.

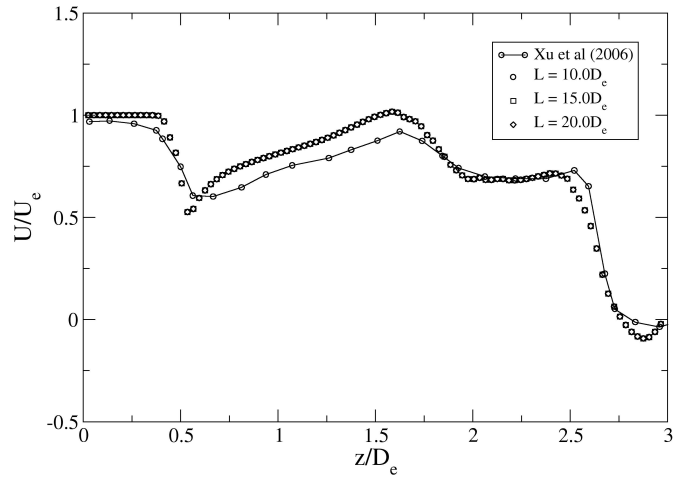


(c) Grid independence test with $L = 10.0D_e$.

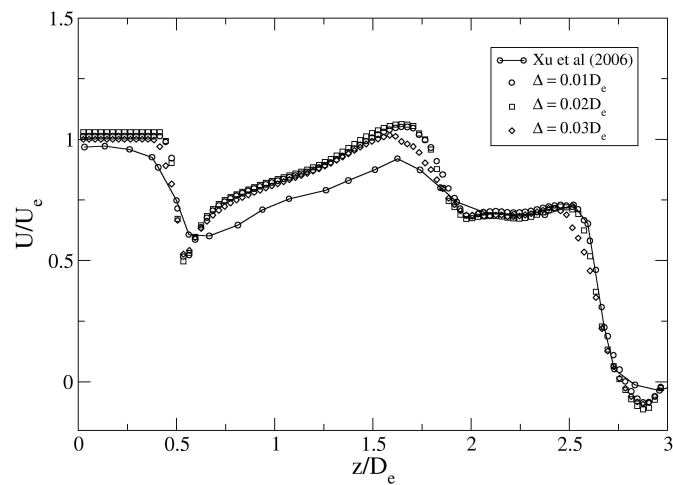
FIGURE 3.25: Validation of Yee's TVD scheme for Case A.



(a) Velocity (Ma) contour plot.



(b) Domain independence test with $\Delta = 0.01D_e$.



(c) Grid independence test with $L = 10.0D_e$.

FIGURE 3.26: Validation of Yee's TVD scheme for Case B .

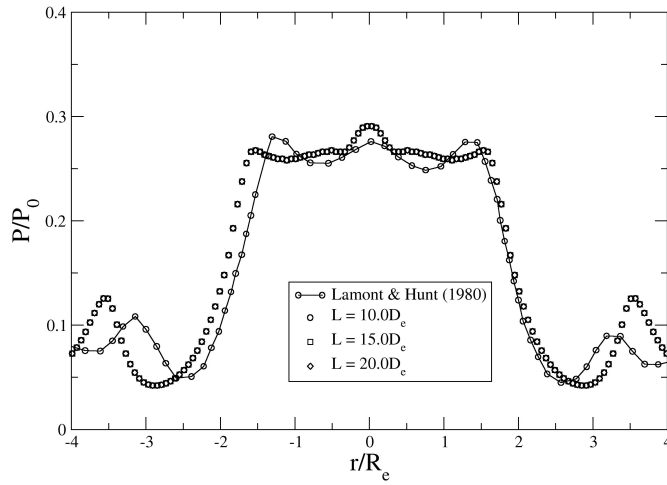
fer to Figure.1.7 for a description) being responsible for the rapid drop in gas velocity at $z/D_e \sim 0.5$. This is followed by an increase in velocity up until the regular reflection at $z/D_e \sim 1.5$. The velocity then plateaus before coming to rest at the impingement plate after passing through the bow shock. The difference between the experimental and numerical data may be attributed to the assumption of a zero nozzle divergence angle and the definition of an isentropic nozzle exit Mach number.

Pressure distributions along the impingement surface

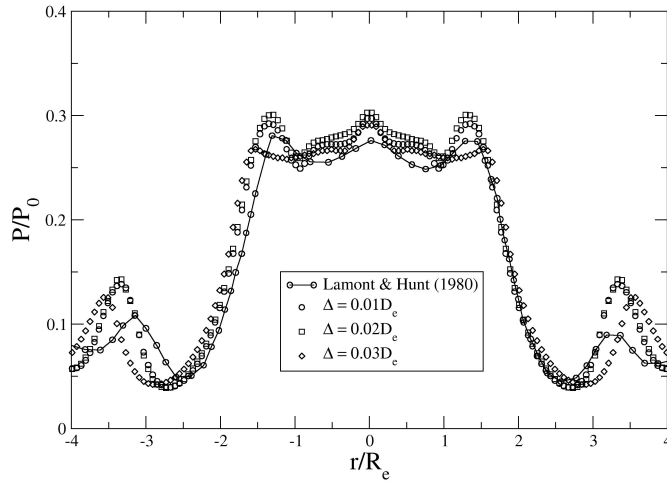
Lamont & Hunt (1980) performed an extensive experimental study of underexpanded jet impingement. The design of the rig deserves some attention as it is believed to influence the variation in surface pressure distribution. The compressed air is supplied to the nozzles using the same configuration as the Carling & Hunt (1974) experiment . The nozzle is connected to a 30 bar main which incorporates a control valve and a settling chamber. It is found that the acoustic reflection from the base of the settling chamber produces unsteadiness in the impinging jet flow for certain flow conditions. Hence, the base of the chamber is covered with a layer of cotton padding to act as a sound absorber. The impingement plate is a circular disk 300 mm in diameter (ten times the nozzle exit diameter) with forty seven pressure tappings arranged along the diameter. The pressure is measured using a 35 bar Druck strain-gauge transducer mounted in a Scanivalve unit.

Flow instability has been frequently reported in supersonic impinging jets as discussed previously in Section.1.4). It often manifests itself in the motion of the shock waves and fluctuation in the surface pressure distribution. For a pressure ratio of $PR = 1.2$, there are some signs of unsteadiness at $s/D_e = 1.5$ but not at other stand off distances. For a higher pressure ratio of $PR = 2.0$, the standoff distances $s/D_e = 2, 2.44$ and 3 all produced considerable oscillations in the position of the Mach disk. If the unsteadiness is indeed a phenomenon inherent in the flow, rather than being dependent on the setup of the experimental rig, the pressure distributions presented here are only meaningful in the averaged sense.

The surface pressure distribution for a moderately and highly underexpanded impinging jet are both plotted in Figure.3.28. An increase in the computational domain size and grid resolution resulted in minimal changes in the surface pressure distribution and shows that the solution is independent of both. The computed pressure distribu-



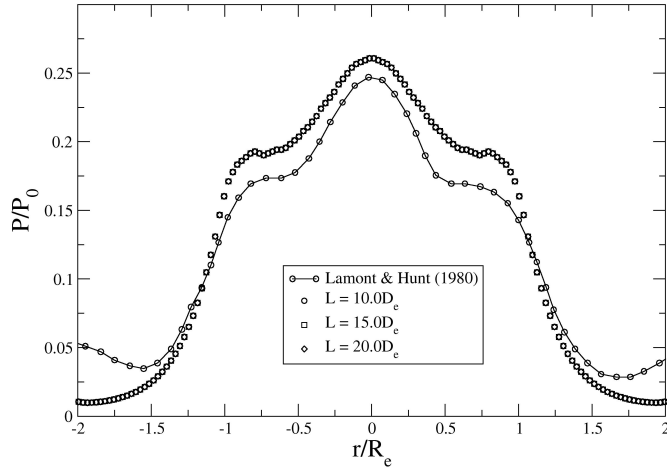
(a) Domain independence test with $\Delta = 0.01D_e$.



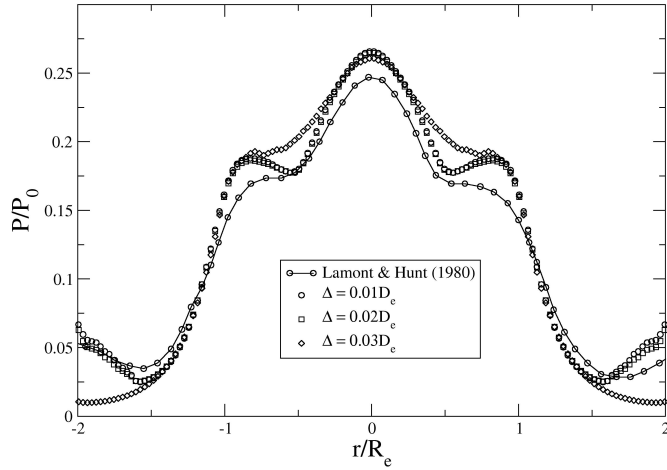
(b) Grid independence test with $L = 10.0D_e$.

FIGURE 3.27: Validation of Yee's TVD scheme for Case C.

tion along the plate is generated by reflecting one half of the axisymmetric solution across the jet centerline. On the other hand, the experimental profiles are obtained along the entire plate length and exhibits a slight asymmetry. The agreement between the two distributions is good with the annular pressure peak suggesting the presence of a recirculation bubble (refer to Figure.1.9 for flow field schematic). This is because the adverse pressure gradient near the pressure peaks encourages flow separation along the plate. As the chamber pressure is increased, the profile transforms into a single peak with a 'shoulder' on either side. The bubble would have completely disappeared once the pressure gradient becomes favorable along the plate.



(a) Domain independence test with $\Delta = 0.01D_e$.



(b) Grid independence test with $L = 10.0D_e$.

FIGURE 3.28: Validation of Yee's TVD scheme for Case *D*.

The validation of the HLLC TVD scheme produced almost identical velocity and pressure profiles and has not been included for the sake of brevity. It should be pointed out that the Yee's TVD Riemann solver will be used to model the steady and unsteady cold spray processes for the remainder of the investigation.

3.2.2 Particle impact statistics

The underexpanded and overexpanded nozzles employed in the steady cold spray simulations are identical to those of Cases *B* and *C*. The exit diameter is 6.0 mm for both nozzles with a standoff distance of 12 and 18 mm for the underexpanded and overexpanded nozzle respectively. The particle is released from rest at the throat and

accelerated along a diverging length of 10 cm. Once the exit velocity is calculated using the one dimensional drag law, the particles are randomly injected across the nozzle exit according to Equation.2.51. The gas phase has already been validated in the previous section and shown to agree favorably with the limited experimental data available. For the data presented in this section, a grid size of $0.01D_e$ and domain length of $L_{crit} = 10D_e$ is used to generate the steady gas flow field. Unfortunately, no experimental data could be found for a particle-laden supersonic impinging jet. The only information that can be used to assess the accuracy of the Lagrangian particle tracking model is the particle velocity measured at the nozzle exit using a commercial laser diagnostic system (Phani *et al.* (2008)). It has been shown in Section.3.1.2 that the inclusion of compressibility effects in the calculation of the drag coefficient resulted in a better agreement with experimental data. Hence, the modified drag coefficient is used for all cold spray simulations.

This section presents the impact velocity and location statistics for cold spray simulations using Aluminium particles. As was done in the parametric study of the cold spray nozzle, a single Aluminium particle is injected from rest at the nozzle throat and the exit velocity is determined assuming isentropic gas flow. A two-dimensional drag law is used to track the particle flight between the nozzle and substrate using the local gas information provided by the compressible flow solver. As soon as the particle reaches the substrate, its impact velocity and location information is stored and another particle is injected at the throat until a total of 10000 particles are injected. Depending on the particle size and the injection point, the time taken by each particle to reach the substrate will vary. All plots have been non-dimensionalised and the physical value of the particle speed and displacement can be easily estimated using the speed of sound at the nozzle exit (248 m/s for the underexpanded and 255 m/s for the overexpanded jet) and the nozzle exit diameter of 6 mm.

To get an appreciation of the spanwise variation in particle impact statistics, the speed of the colliding particles is shown in Figure.3.29a-b as a function of the radial distance from the nozzle centerline and replotted in Figure.3.29c-d as a function of the particle size. In an underexpanded jet, the particle impact velocity is highest at the jet centerline and near the edge of the injection boundary with the minimum occurring at $r/D_e \simeq 0.2$. In an overexpanded jet, the particle impact velocity steadily increases as it is injected further away from the jet centerline. When the same data is plotted as a

function of particle size, a 'bandwidth' in the impact velocity is observed in the sense that there is a distinct range of velocity values for each particle size. In both jets, the maximum 'bandwidth' occurs for particles around $10\ \mu\text{m}$ in diameter which happen to have the highest impact speeds as well. The maximum impact speed is greater in an overexpanded jet because the particles decelerate over a shorter distance between the bow shock and substrate (see Figure.3.26).

The particle impact angles are plotted in Figure.3.30 in both the spanwise direction and as a function of diameter. Across the jet impingement region, the small impact angles suggest that the majority of particles tend to travel in a recitilinear path. It can be seen in Figure.3.30c-d that any particles larger than $10\ \mu\text{m}$ in diameter is guaranteed to hit the substrate almost perpendicularly. This justifies the use of Equation.2.51 for injecting particles greater than $10\ \mu\text{m}$ in diameter. The particles with the largest impact angles are small in diameter and appears to have have been deflected along the wall jet. This is because the impingement angle ($\theta_p = \tan^{-1}(v/u)$) increases as the radial velocity exceeds the axial velocity. To demonstrate this, the trajectories of a 5 and $10\ \mu\text{m}$ particle injected at $r/D_e = 0.1, 0.2, 0.3$ and 0.4 across the nozzle exit are plotted in Figure.3.31. The $10\ \mu\text{m}$ particles penetrate straight through the supersonic impinging jet as expected while the $5\ \mu\text{m}$ particle injected at $r/D_e = 0.2$ is deflected away from the substrate and carried along the wall jet.

3.2.3 Particle dynamics

From the impact data, it is clear that the smaller particles produce on average higher impact speeds which varies depending on their injection location. To find out why this is so, the variation in particle velocity and acceleration as it travels between the nozzle exit and substrate are extracted. The particle acceleration ($\frac{du}{dt} \times \frac{D_e}{a_c^2}$) serves as an indication of the drag per particle unit mass as defined by Equation.2.43. In both jets, a particle is injected at $r/D_e = 0.2$ across the nozzle exit and is tracked until it reaches the substrate. Figure.3.32 shows that the drag acting on the particle increases significantly after it passes through the Mach disk (bow shock) located at $z/D_e \sim 1.3$ and 2.7 for the underexpanded and overexpanded jet respectively. Among the two particle sizes used, the $5\ \mu\text{m}$ particle traveling in an underexpanded jet experiences the greatest drag force per unit mass and consequently is decelerated the most after crossing the bow shock. Because the distance between the bow shock and substrate

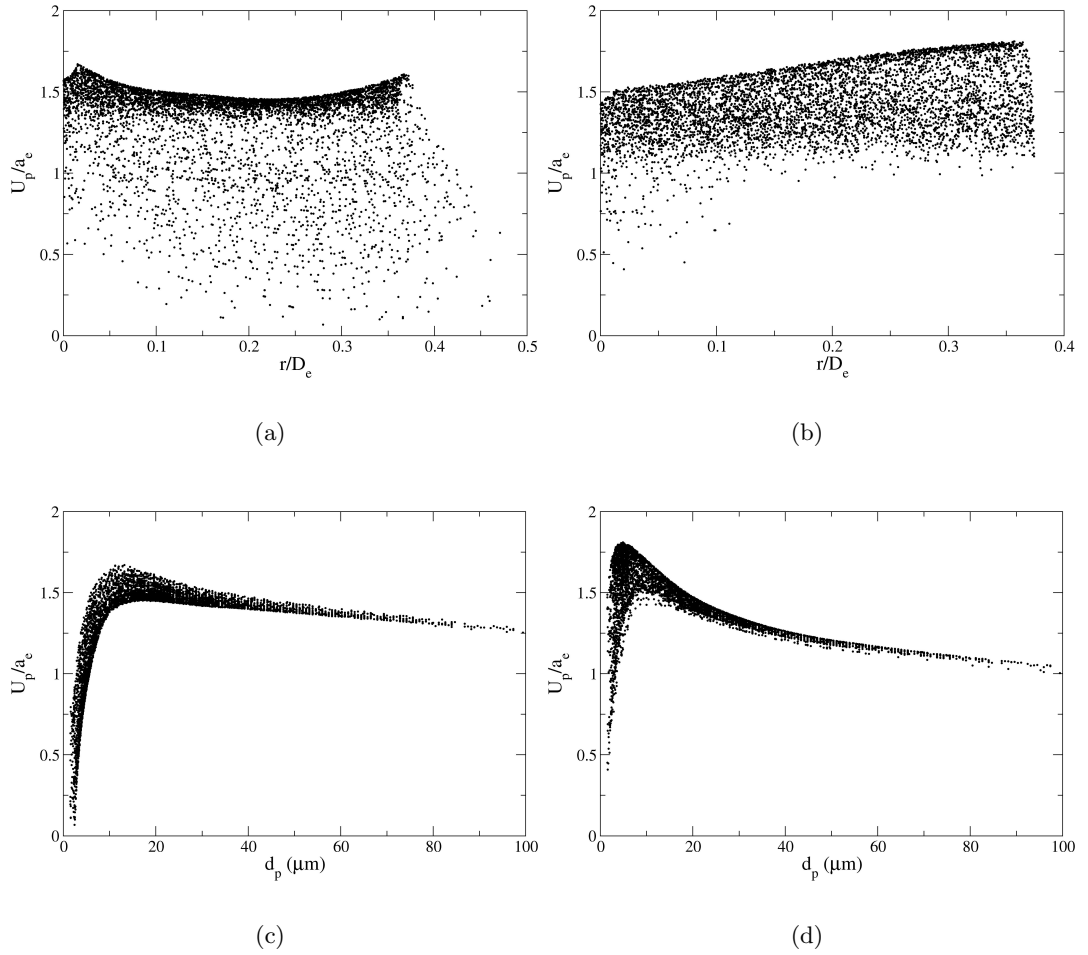


FIGURE 3.29: Particle impact speed during the cold spray process using an (Left column) underexpanded and (Right column) overexpanded impinging jet. The top row plots the impact speed as a function of radial distance and the bottom row plots the speed as a function of diameter.

is shorter in an overexpanded jet, the particle deceleration is considerably lesser (see Figure.3.26). As the particle diameter increases, the drag per unit mass decreases and with it the amount of deceleration between the Mach disk and substrate.

It is often useful to non-dimensionalise the particle size and density in terms of the Stokes number. This was defined back in Section.1.5 using the particle response time and a time scale related to the fluid flow ($St = \frac{\tau_A}{\tau_F}$). The response time of a particle represents the time required for a particle released from rest in a uniform flow to reach 63% of the flow velocity. It is effectively a measure of the aerodynamic responsiveness of a particle. For an incompressible flow, it has been established that particles with a Stokes number much less than one can track the fluid path correctly (see Section.1.5).

In order to define the Stokes number for the particles traveling in a supersonic im-

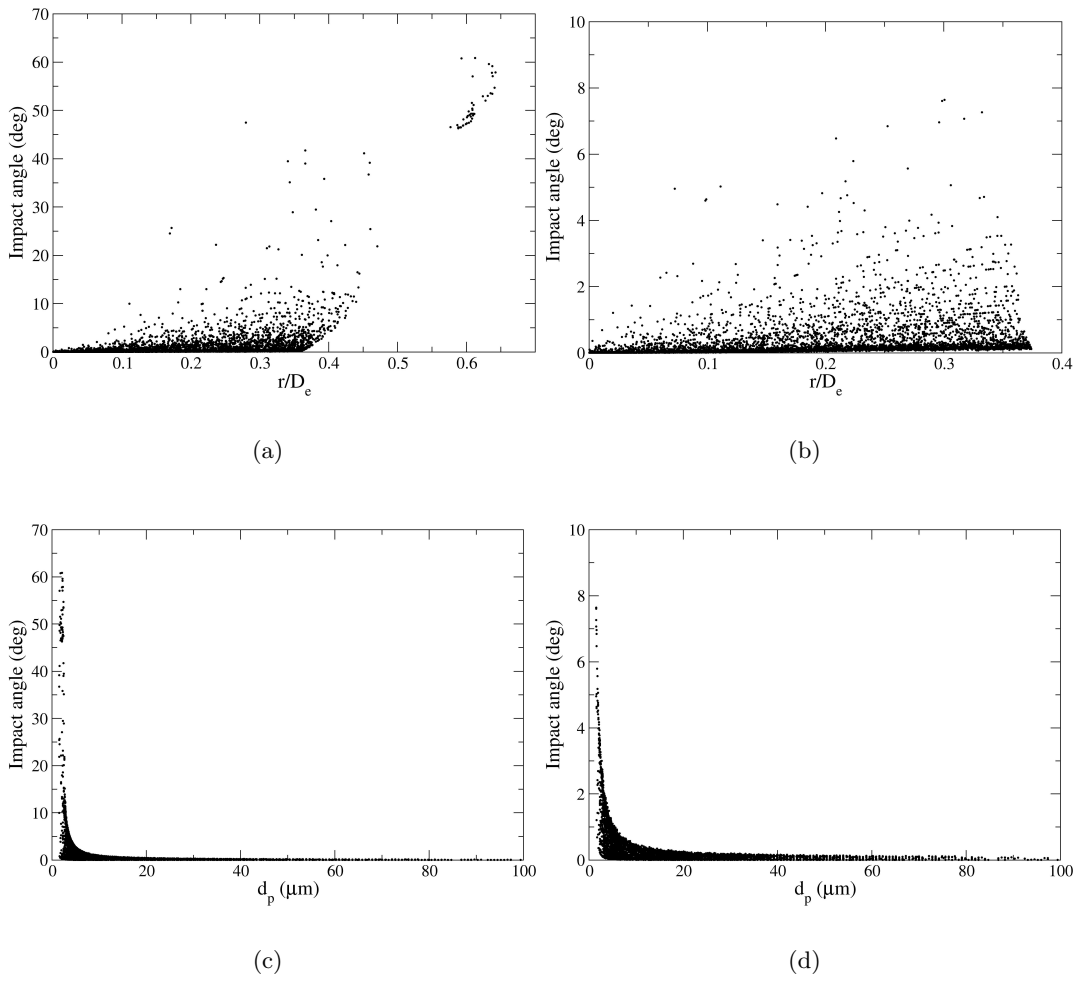


FIGURE 3.30: Particle impact angle during the cold spray process using an (Left column) underexpanded and (Right column) overexpanded impinging jet. The top row plots the impact speed as a function of radial distance and the bottom row plots the speed as a function of diameter.

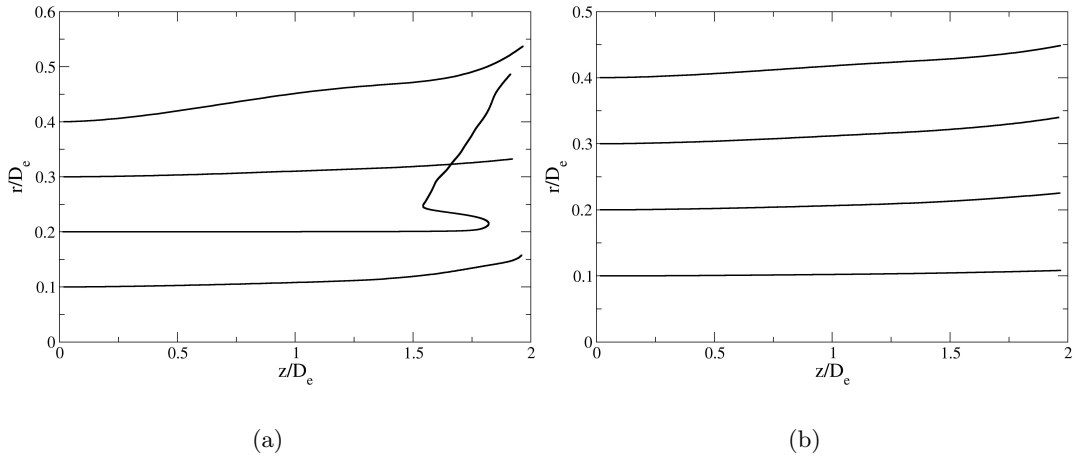


FIGURE 3.31: Particle trajectories of a (a) 5 and (b) 10 μm Aluminium particle injected during the steady cold spray process using an underexpanded impinging jet.

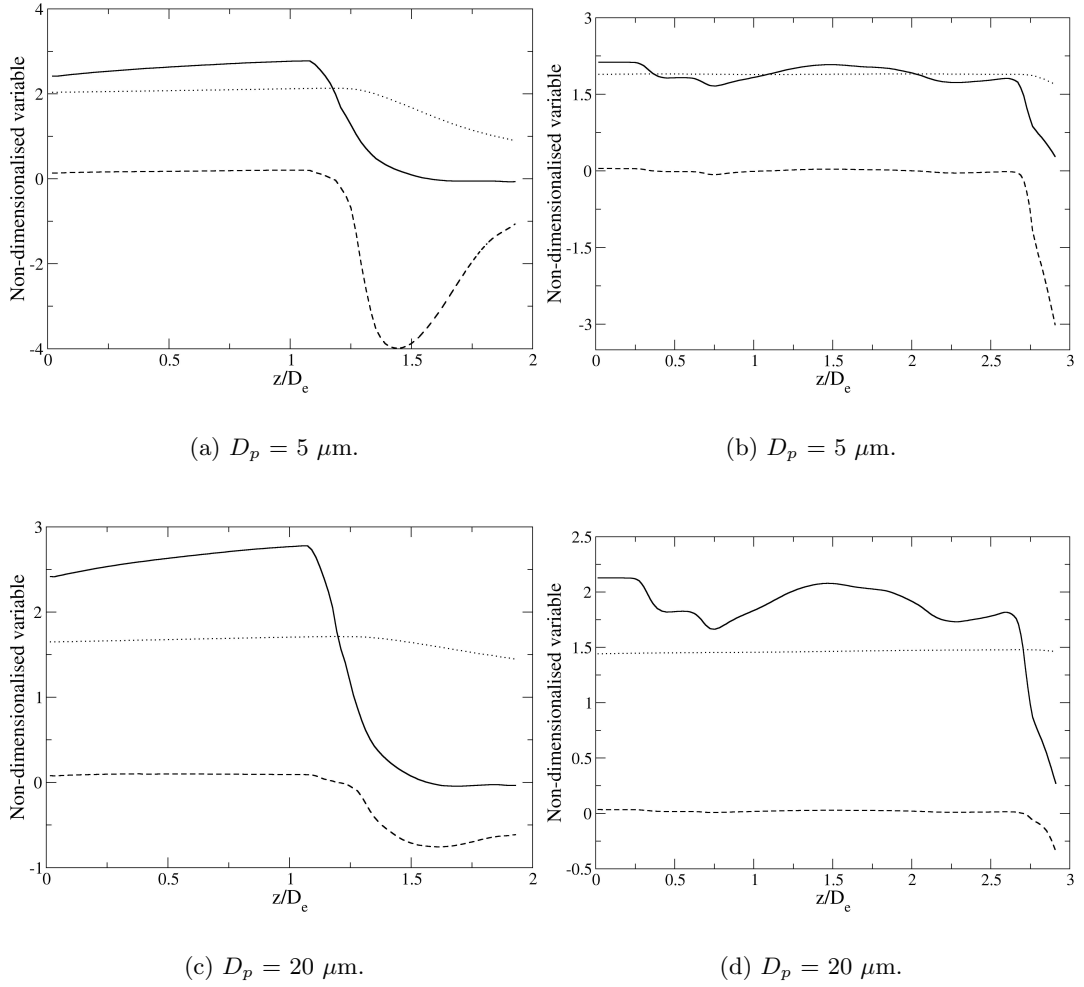


FIGURE 3.32: Streamwise gas and particle velocity and drag force ($r/D_e = 0.2$) during the cold spray process using an (left column) underexpanded and (right column) overexpanded impinging jet. Solid line - $\frac{u}{a_e}$; dotted line - $\frac{u_p}{a_e}$; dashed line - $\frac{du_p}{dt} \left(\frac{D_e}{a_e^2} \right)$.

pinging jet, the response time across the bow shock is used. To simplify the calculation, the bow shock is replaced by a 'normal shock' across which the gas velocity at the nozzle exit is suddenly decelerated as shown in Figure.3.34a. The post shock flow conditions (ρ_s and T_s) may be estimated from Figure.3.33 which plots the axial gas velocity, density and temperature along $r/D_e = 0.2$ for both impinging jets. Reading off this figure, the non-dimensional post shock density and temperature is assumed to be constant at 1.5 and 2.0 (dimensional values of 4.1 kg/m^3 and 308 K) for the underexpanded jet and 3.8 and 2.0 (dimensional values of 5.2 kg/m^3 and 324 K) for the overexpanded jet. Although Figure.3.32 indicates that the gas velocity increases slightly between the nozzle exit and bow shock, their variation has minimal effect on the particle velocity for short standoff distances. Hence, the particle is injected at the nozzle exit speed

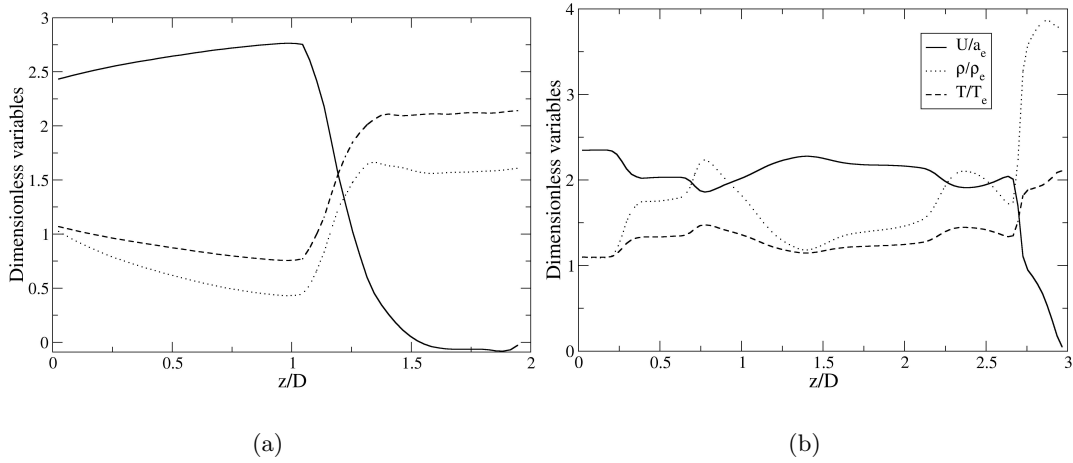


FIGURE 3.33: Axial variation in gas velocity, density and temperature along $r/D_e = 0.2$ during the steady cold spray process using an (a) underexpanded and (b) overexpanded impinging jet.

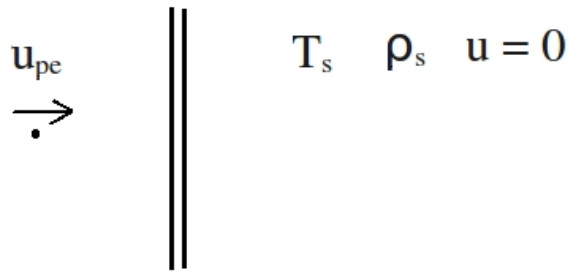
TABLE 3.2: Particle Stokes number when traveling in an (second row) underexpanded and (third row) overexpanded impinging jet.

dp (μm)	5	10	15	20	25	30	35	40	45	50
St	0.96	3.8	9.2	18	29	43	61	81	105	131
St	0.88	3.5	8.5	16	27	40	56	75	97	122

prior to the 'normal shock' and the time taken to reduce this speed by 63% is defined as τ_A shown in Figure.3.34a. The nozzle exit diameter and speed of sound is used to define the fluid time scale $\tau_F = \frac{D_e}{a_e}$. The Stokes number for particles traveling in both supersonic impinging jets are listed in Table.3.2. Referring back to Figure.3.29c-d, the peak impact velocity for both jets occur when injecting Aluminium particles with a Stokes number of approximately 1.0 ($D_p = 10 \mu\text{m}$).

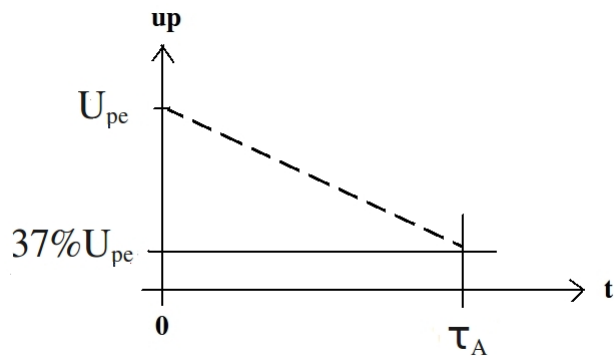
3.2.4 Discussion of results

The data presented in the Section.3.2.2 and 3.2.3 will now be discussed in the context of developing a theoretical model for estimating the particle impact speed during the steady cold spray process. It is clear from Figure.3.32 that despite variation in the axial gas velocity, the particle velocity remains almost constant as it approaches the bow shock for a short standoff distance. Depending on the particle size and the distance between the bow shock and substrate, it may experience some or considerable deceleration after crossing the bow shock. In the previous section, the particle Stokes number was estimated by replacing the bow shock with a 'normal shock', across which

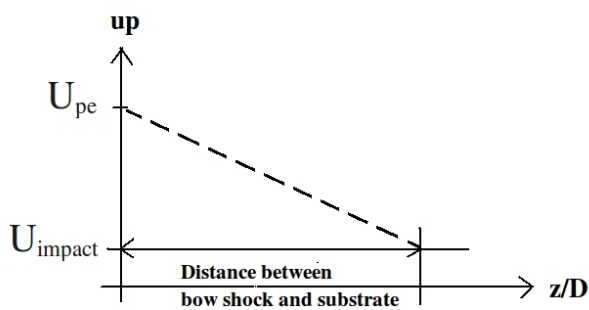


"Normal shock"

(a)



(b)



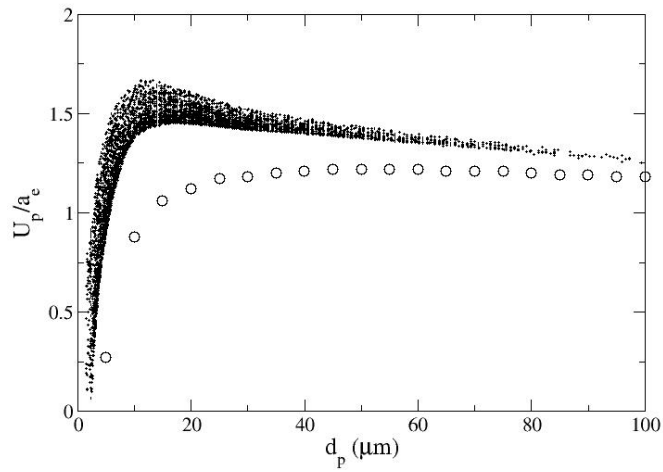
(c)

FIGURE 3.34: (a) Estimation of the particle Stokes number and impact velocity were done using a normal shock model where the post shock conditions are defined by the average flow conditions behind the bow shock. (b) The particle response time (τ_A) is defined as the time needed to reduce the exit particle velocity by 63% after crossing the 'normal shock' at $t = 0$. (c) The impact speed is the final speed of the particle after crossing the 'normal shock' along a distance equal to that between the bow shock and substrate.

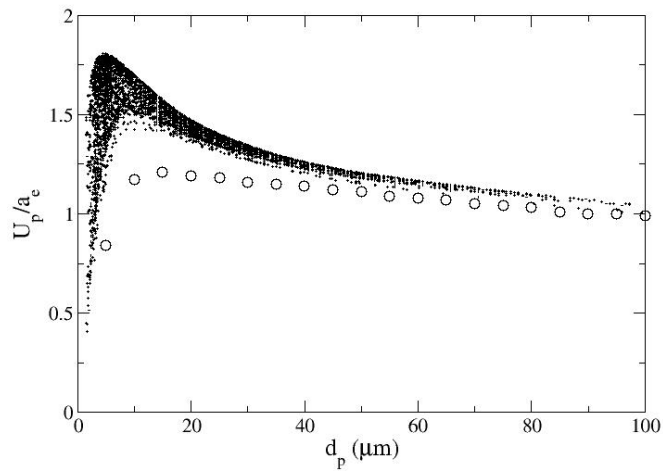
the nozzle exit gas velocity is suddenly brought to rest and with density and temperature increases indicative of those in the real flow. Continuing on this analysis, the distance between the bow shock and the substrate can be used to estimate the particle impact speed as described in Figure.3.34c. A particle traveling at the nozzle exit particle speed is decelerated across the 'normal shock' over a distance equal to that between the bow shock and substrate ($\simeq 1.5D_e$ and $0.5D_e$ for underexpanded and overexpanded jet respectively). The final particle speed calculated using Equation.3.7 then constitutes the estimated particle impact velocity and is plotted alongside the simulated particle impact velocity in Figure.3.35.

It is clear that the present model tends to underestimate the particle impact speed over a range of particle diameters. This result may be interpreted as a consequence of the bow shock being smeared across several cells where as a physical normal shock assumes a sudden discontinuity in the gas velocity, density and temperature. This is highlighted in the underexpanded jet where the velocity gradient across the bow shock covers a distance nearly as long as the nozzle exit diameter. The agreement between the proposed model and simulated results is better when the shock is not as smeared such as in the case of the overexpanded jet. Unfortunately, all TVD schemes suffer from the same drawback as they use artificial viscosity to stabilise the solution (Toro (1999)). Although simulations of the supersonic impinging jet was verified back in Section.3.2.1, it is known that even experimental techniques such as Particle Image Velocimetry suffers from smearing of flow discontinuities due to particle lagging. The effect of the shock induced velocity gradient on the correlation function has been investigated by Mitchell *et al.* (2009). Their work show that the interrogation window not only produces a bias in the mean velocity vectors but also introduces an artificial fluctuating component due to the movement of the peak on the correlation plane.

Nevertheless, the key to making this model a practical tool for estimating the particle impact velocity is being able to identify the bow shock location and post shock density and temperature. A literature review of supersonic impinging jets revealed that there are analytical tools available for calculating the bow shock shape and strength. Gummer & Hunt (1974) investigated the impingement flow produced by eight different underexpanded jets. In their paper, shadowgraphs of the shock structures as well as surface pressure measurements were compared with those obtained using the method of integral relations. The two results agree quite well in the inner impingement region but



(a)



(b)

FIGURE 3.35: Particle impact speed during the cold spray process using an (a) underexpanded and (b) overexpanded impinging jet. Black hollow circles represent the estimated particle impact speed.

deviated in the outer region as shown in Figure.3.36. The discrepancy is ascribed to the inability of the approximate linear flow functions to represent the shear layer emanating from the triple point (see Section.1.4 for supersonic impinging jet schematic). By extension, the method allows an estimation of the average gas density and temperature - assuming an ideal gas - behind the bow shock for a given set of nozzle exit conditions. Currently, the integral method has only been validated for underexpanded impinging jets.

Once the particle impact information (i.e.impact speed) is given, it can be used as

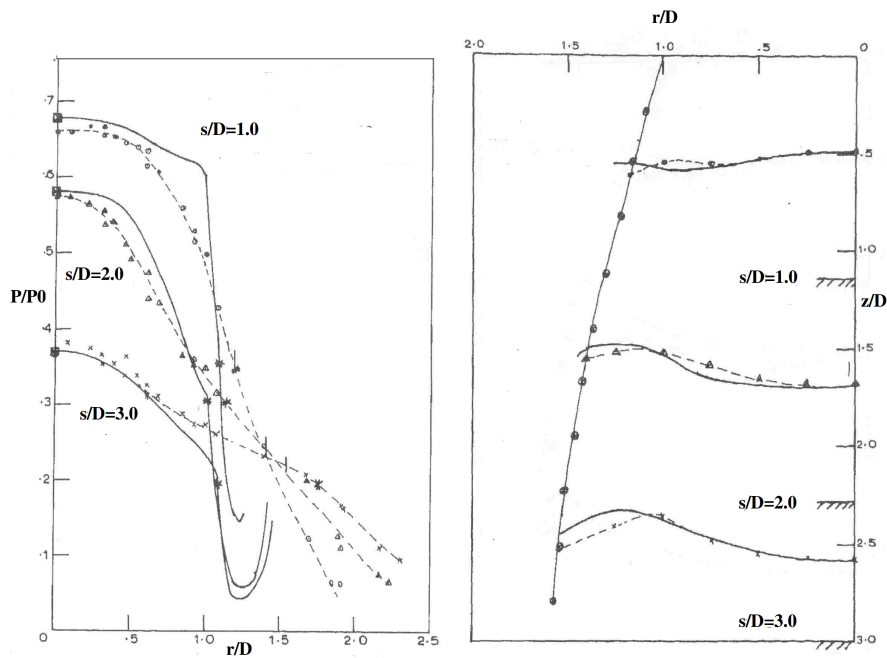


FIGURE 3.36: (Left) Non-dimensionalised surface pressure distributions for an underexpanded impinging jet with $Ma_e = 2.0$, $\theta = 5$, $PR = 3.0$. (Right) The jet boundary and bow shock profile for different standoff distances. The lines represent theoretical values and the points represent experimental data. Adapted with permission from Gummer & Hunt (1974)

the input data for modelling the particle impact phenomena. This technique allows an estimation of the particle deposition efficiency and an understanding of the interfacial bonding phenomena for various combinations of particle and substrate materials (see Figure.1.3). Although the particle impact speed using the current supersonic impinging jets is insufficient for the deposition of Aluminium particles on a Copper substrate - primarily due to the low value of $T_0 = 300K$ - these conditions are nevertheless selected for two reasons. The first one is that it allows the validation of the gas phase and the second one is that it gives a comparison between two supersonic nozzles with similar exit gas speed.

3.3 Transient cold spray process

The final part of the investigation looks into a novel unsteady cold spray process using a shock tube. As seen from the description given in Section.1.6, the process suffers from a number of disadvantages such as the very limited duration of cold spraying, the need to replace the shock tube after each run and the timing of particle injection to coincide with the passing of the moving shock. Nevertheless, monodisperse particles are injected in the wake of the shock to compare the impact speed produced by steady and unsteady cold spray processes. To simplify the mesh, a circular pipe is used on its own instead of being attached to a nozzle. It was found that this process also offers a mean of studying the shock formation process in underexpanded impinging jets. The shock speed can be selected such that either a shock diamond ($Ma_{sh} = 1.5$) or Mach disk ($Ma_{sh} = 1.8$) is reproduced in the impingement region characteristic of a moderately and highly underexpanded jet.

The research objectives for the numerical investigation of unsteady cold spray impinging jet flow are as follows.

1. To visualise the shock formation process during the unsteady cold spray process and compare its flow features with that of a steady supersonic impinging jet
2. To characterise the particle dynamic response as it travels across a transient shock structure

This chapter presents data extracted from simulations of unsteady cold spray impinging jet flow. Section.3.3.1 presents a validation of the gas flow using limited experimental data available. The shock speeds (M_{sh}) are 1.5 and 1.8 and it will be shown that these conditions produce a shock structure which is consistent with those observed in steady underexpanded impinging jets. The flow morphology is visualised using a numerical schlieren technique and is complemented with streamwise and spanwise data in Section3.3.2. Particles are injected across the pipe exit in Section.3.3.3 to assess the particle response in transient high speed gas flows. Finally, the results are summarised and discussed in Section.3.3.4.

3.3.1 Numerical validation

One of the very few experimental data available for a planar shock impingement was obtained by Zare-Behtash *et al.* (2008). The motivation for the study was to characterise

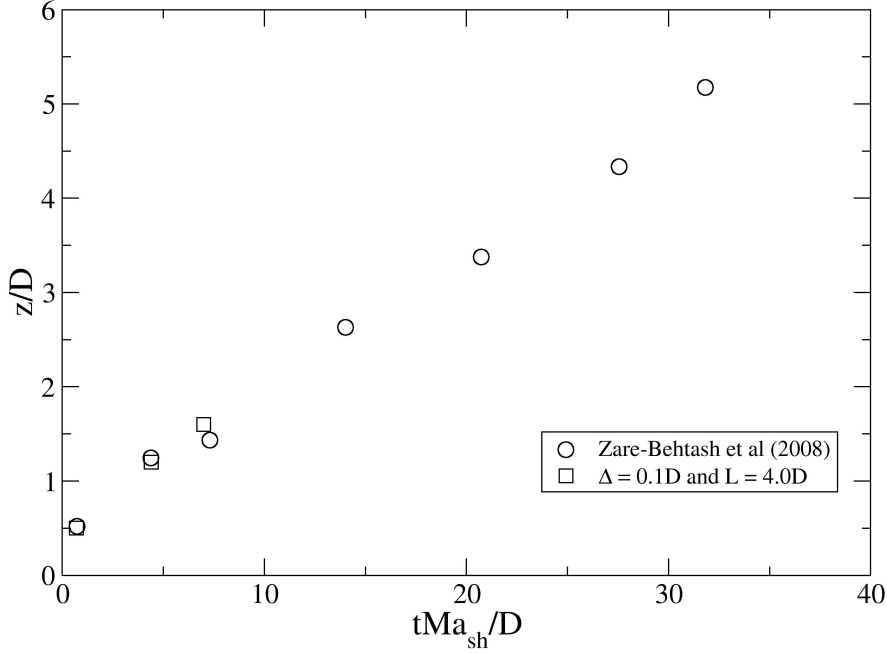


FIGURE 3.37: Validation of Yee’s TVD scheme for a planar shock ($P_P/P_a = 4.0$) exiting from a pipe into ambient conditions.

the evolution of detonation waves commonly found in pulse detonation engines. To model this process, a planar shock passes through a square, circular and elliptical pipe with diaphragm ratios of $P_P/P_a = 4, 8$ and 12 . Both qualitative (schlieren) and quantitative (PIV) techniques are employed to elucidate the formation process of the compressible vortex loops and the embedded shock waves. A model 9306A TSI six-jet atomiser is used to seed the flow with oil droplets of $1 \mu m$ diameter. The particle relaxation time for the droplets is calculated as $\tau_A = 2.2 \mu s$ and the data is post-processed using the software Insight 6.0.

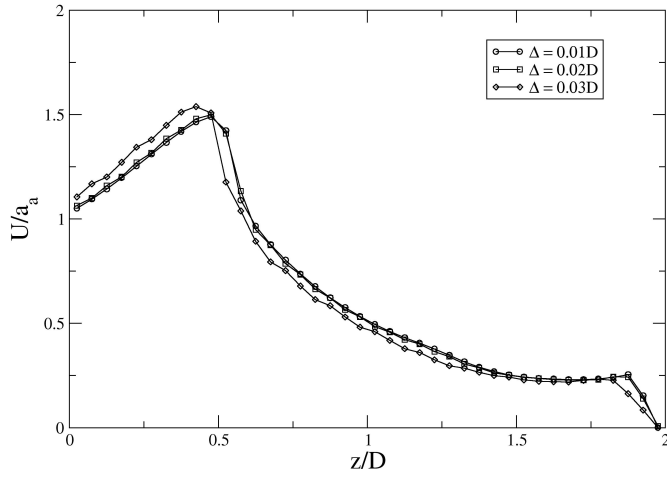
Figure.3.37 shows the convection of the compressible vortex issued from a circular pipe as a function of time. The vortex position is defined by the location of peak vorticity and is non-dimensionalised by the nozzle diameter while the dimensionless time is referenced to the emergence of the shock from the pipe. A grid and domain size of $0.01D$ and $4D$ is used respectively to simulate this flow. In order to minimise the reflections at the outflow computational boundaries, the domain size is defined such that the moving shocks doesn’t reach the boundaries during the course of simulation. The validation case was terminated at $ta_a/D = 8.0$ by which stage two shock cells are fully developed in the evolving free jet. Due to the short stand off distance between the pipe and substrate, a single albeit compressed shock cell is formed during the jet

impingement process. Hence, only the verification of the first shock cell structure in the free jet is relevant. The agreement during the initial stages of the vortex evolution is quite good as seen in Figure.3.37.

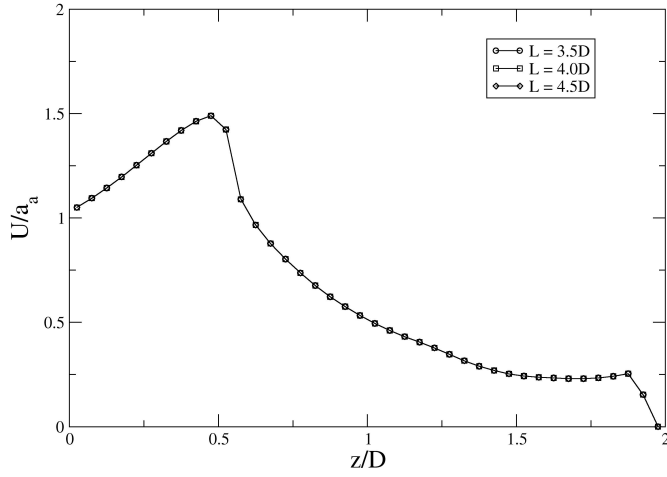
3.3.2 Flow morphology

As usual, a grid and domain study is first performed to characterise the effect of the domain and grid size on the variation in data. To do this, the velocity profile in the streamwise direction at $r/D = 0.1$ is extracted for a planar shock traveling at $M_{sh} = 1.0$ and 1.5 ($P_P/P_a = 2.5$ and 3.6 respectively) and is shown in Figure.3.39. The origin of the z axis is fixed at intersection of the nozzle exit and jet centerline. A uniform grid is used for all simulations and it can be seen that minor changes occur in the velocity profiles as the grid size decreases from $0.03D$ to $0.02D$. The profiles for grid sizes of $0.01D$ and $0.02D$ are nearly superimposed on top of the other suggesting grid convergence. The domain size is changed uniformly by increasing the length of the pipe and the distance between the outer pipe wall and the top computational boundary (see Figure.2.9). The domain sizes have been defined to ensure that the evolving shock structure doesn't leave the computational domain during the simulation. This is done to minimise any reflection which may occur at the far field boundaries as a result of outflow. It can be seen that the increase in domain size produces minimal variation in the streamwise velocity profile. For the data presented in this section, a grid size of $0.01D$ and domain length of $4.0D$ are used.

A series of numerical 'schlieren' flow visualisations are derived by taking the density gradient of the flow field according to the formula ($e^{-0.1|\nabla\rho|}$). This technique clearly outlines the shock formation process during the impingement of the planar shock as shown in Figures.3.40 and 3.41. The drawback of these flow visualisations is that it doesn't provide any quantitative information about the flow. A major advantage in using numerical simulation is that it allows for the extraction of flow variables at any point in time and space. The instantaneous streamwise profiles along $r/D = 0.1$ for the gas speed, density and temperature are plotted in Figures.3.42 to complement the numerical 'schlieren' images. The spanwise profiles before and after the Mach disk at $ta_a/D = 3.0$ is shown in Figure.3.43. This time is selected because the shock structure at this stage is representative of that commonly observed in steady underexpanded impinging jets (see Figure.1.9).



(a) $Ma_{sh} = 1.5$ and $s/D = 2.0$.

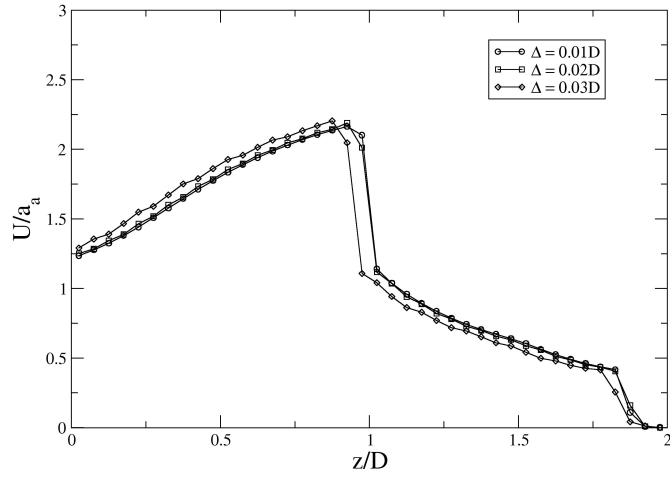


(b) $Ma_{sh} = 1.5$ and $s/D = 2.0$.

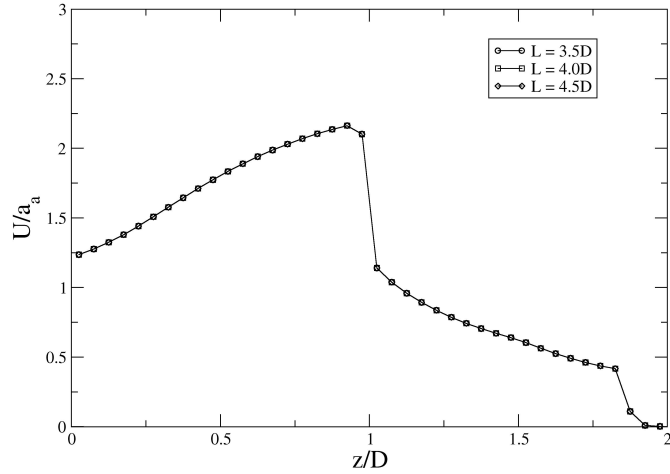
FIGURE 3.38: Comparison of axial velocity profiles at $ta_a/D = 1.4$ and $r/D = 0.1$ using different grid resolutions and domain sizes.

3.3.3 Particle dynamics

In order to capture the response of particles traveling in a transient compressible flow, a single particle is injected at $r/D = 0.1, 0.2, 0.3$ and 0.4 across the pipe exit as was done in the latter part of Section.3.2.2. The non-dimensionalised particle location, velocity and acceleration at each time step is stored until the particle reaches the substrate. The particle trajectories are plotted in Figure.3.44 with the origin located at the intersection of the nozzle exit and jet centerline axis. The axial velocity and acceleration of a particle injected at $r/D = 0.1$ is shown in Figure.3.45 together with the local gas velocity. The



(a) $Ma_{sh} = 1.8$ and $s/D = 2.0$.



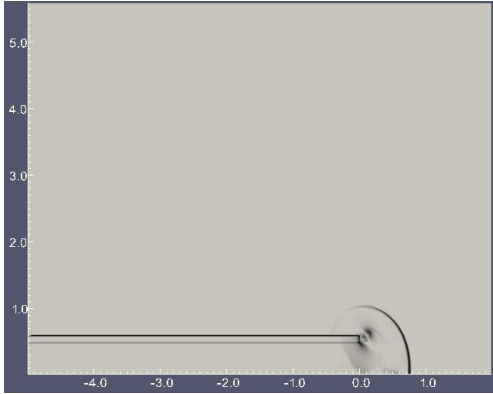
(b) $Ma_{sh} = 1.8$ and $s/D = 2.0$.

FIGURE 3.39: Comparison of axial velocity profiles at $ta_a/D = 1.4$ and $r/D = 0.1$ using different grid resolutions and domain sizes.

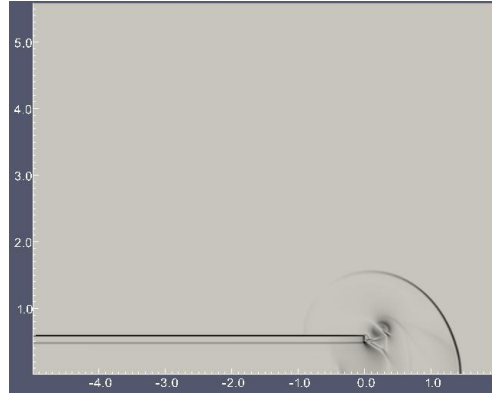
radial velocities are not shown as they are very small by comparison. The ambient speed of sound and pipe diameter are 248 m/s and 3 cm respectively and can be used to extract the physical values from the plots.

3.3.4 Discussion of results

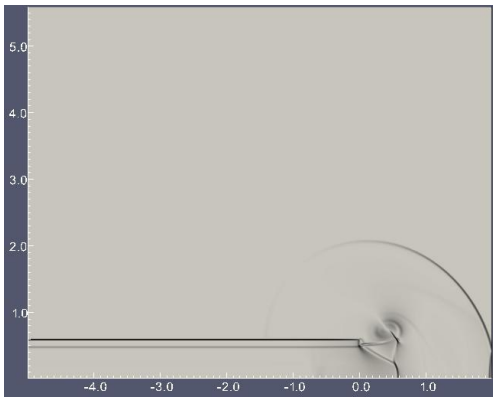
The data presented in the Section.3.3.2 and 3.3.3 will now be used to characterise the shock formation process during an unsteady cold spray process and the associated particle dynamics.



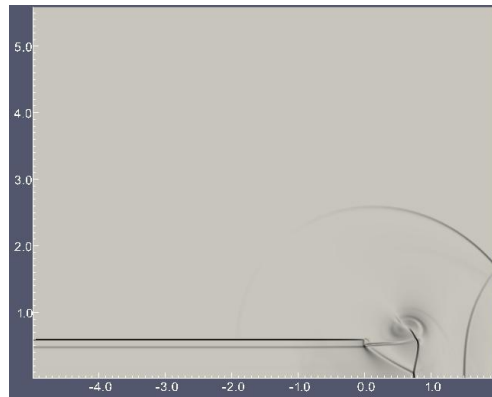
(a) $ta_a/D = 0.5$



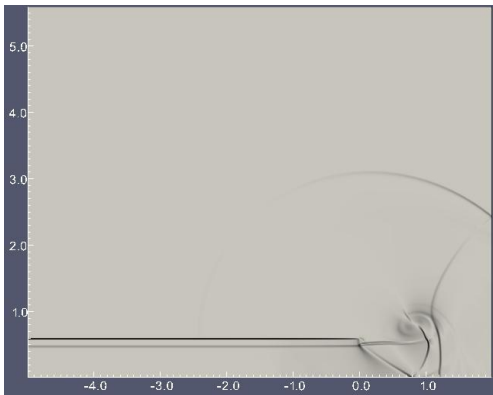
(b) $ta_a/D = 1.0$



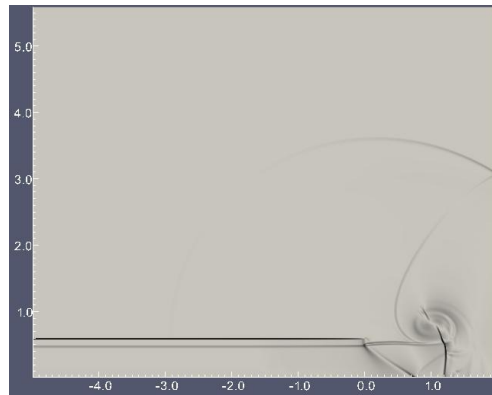
(c) $ta_a/D = 1.5$



(d) $ta_a/D = 2.0$

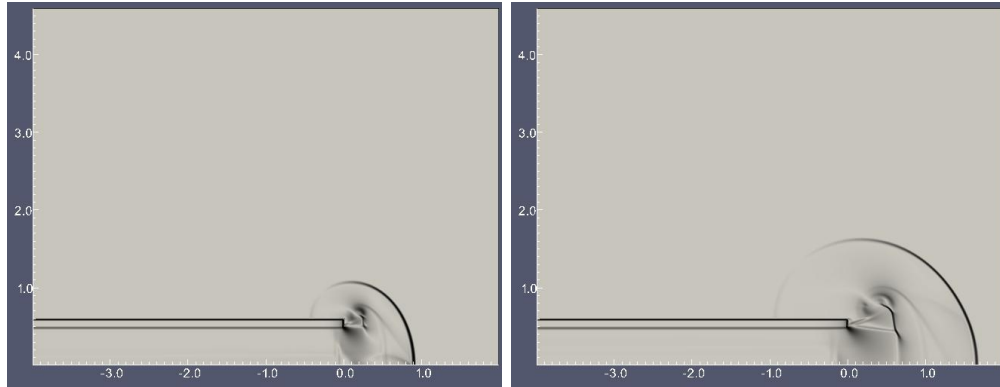


(e) $ta_a/D = 2.5$



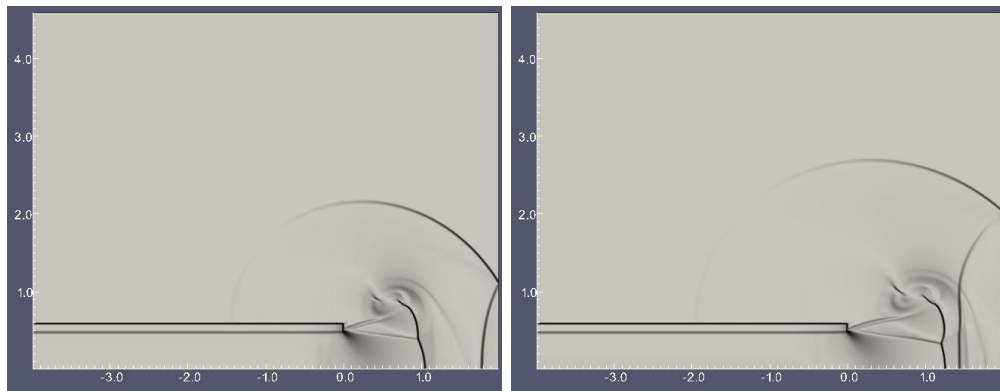
(f) $ta_a/D = 3.0$

FIGURE 3.40: Numerical 'schlieren' of a transient underexpanded impinging jet operating at $Ma_{sh} = 1.5$ and $s/D = 2.0$. The length scales have been non-dimensionalised with respect to the pipe diameter.



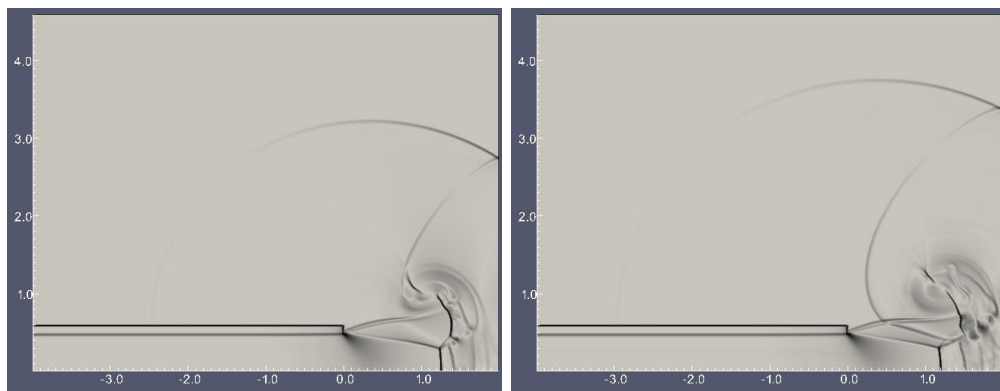
(a) $ta_a/D = 0.5$

(b) $ta_a/D = 1.0$



(c) $ta_a/D = 1.5$

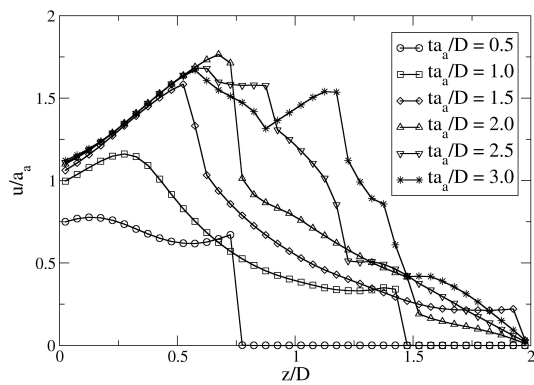
(d) $ta_a/D = 2.0$



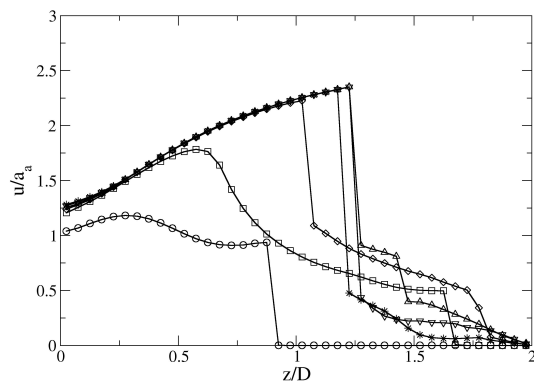
(e) $ta_a/D = 2.5$

(f) $ta_a/D = 3.0$

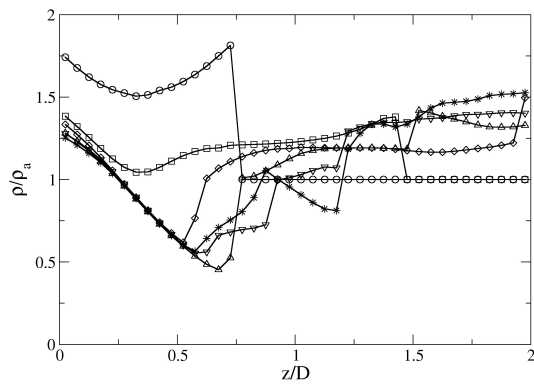
FIGURE 3.41: Numerical 'schlieren' of a transient underexpanded impinging jet operating at $Ma_{sh} = 1.8$ and $s/D = 2.0$. The length scales have been non-dimensionalised with respect to the pipe diameter.



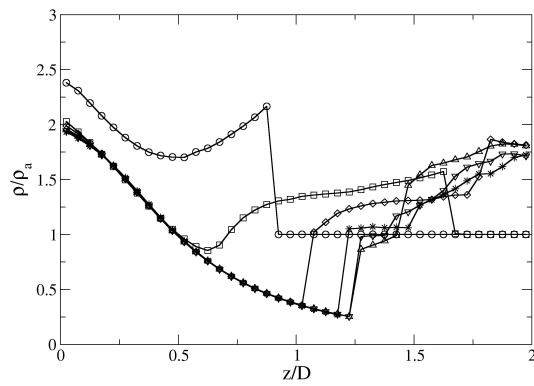
(a) Axial velocity profile



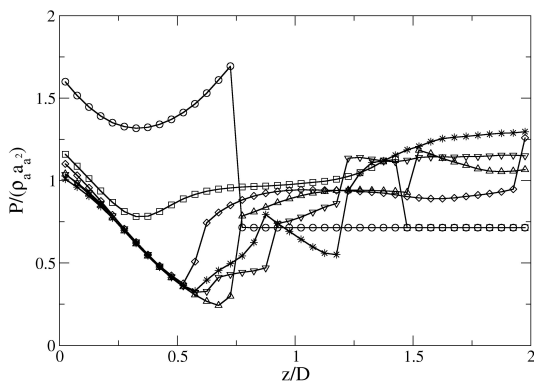
(b) Axial velocity profile



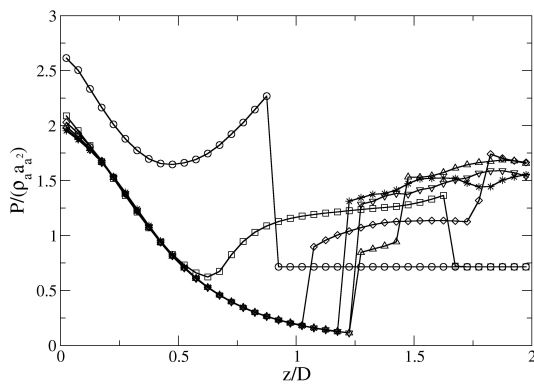
(c) Density profile



(d) Density profile



(e) Pressure profile



(f) Pressure profile

FIGURE 3.42: Evolution of streamwise profiles at $r/D = 0.1$ for a transient underexpanded impinging jet operating at (left column) $Ma_{sh} = 1.5$, $s/D = 2.0$ and (right column) $Ma_{sh} = 1.8$, $s/D = 2.0$.

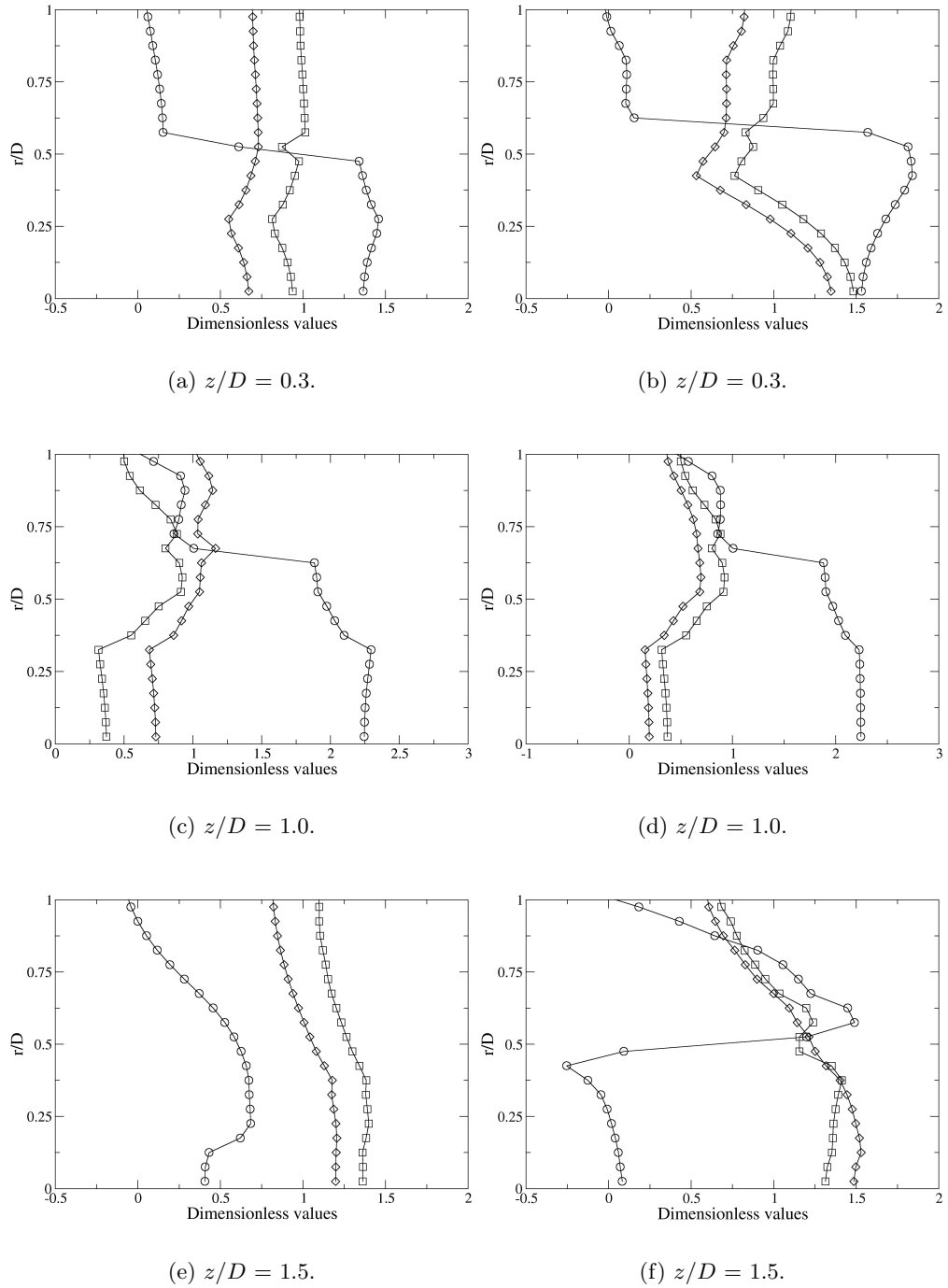
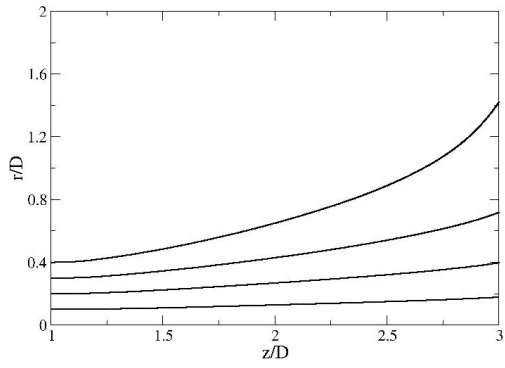
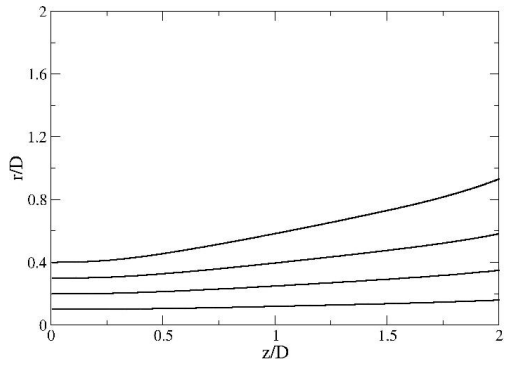


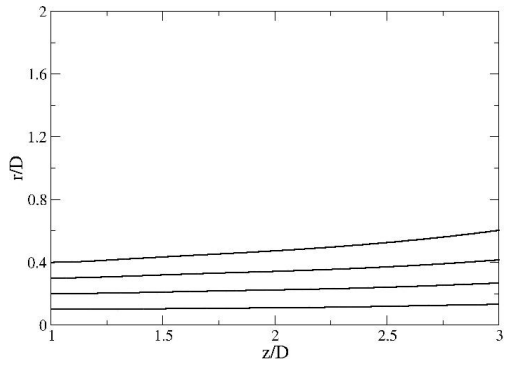
FIGURE 3.43: Spanwise profiles at $ta_a/D = 3.0$ for a transient underexpanded impinging jet operating at (left column) $Ma_{sh} = 1.5$, $s/D = 2.0$ and (right column) $Ma_{sh} = 1.8$, $s/D = 2.0$. \circ - velocity profile $\frac{U}{a_a}$, \square - density profile $\frac{\rho}{\rho_a}$ and \diamond - pressure profile $\frac{P}{\rho_a a_a^2}$.



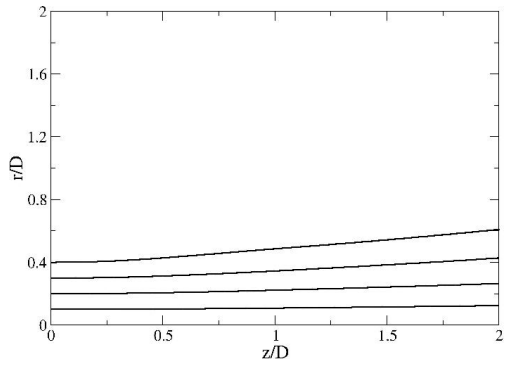
(a) $D_p = 3 \mu\text{m}$.



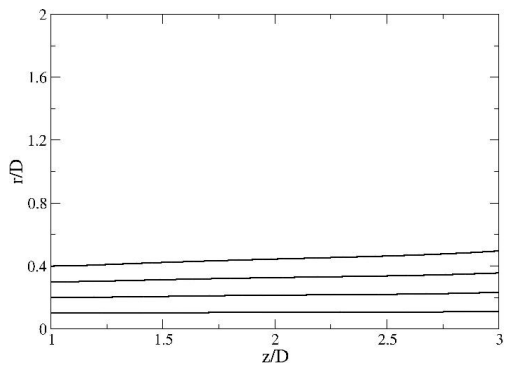
(b) $D_p = 3 \mu\text{m}$.



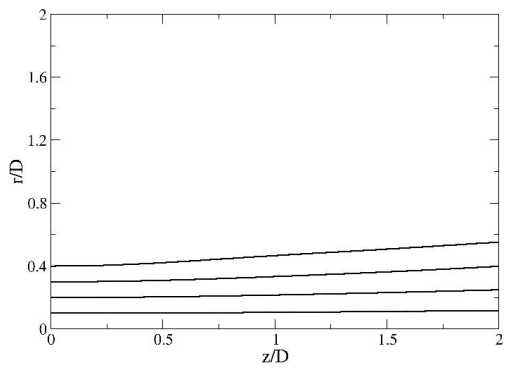
(c) $D_p = 6.5 \mu\text{m}$.



(d) $D_p = 6.5 \mu\text{m}$.



(e) $D_p = 10 \mu\text{m}$.



(f) $D_p = 10 \mu\text{m}$.

FIGURE 3.44: Trajectories of particles injected at $r/D = 0.1, 0.2, 0.3$ and 0.4 across the pipe exit. Left and right columns are results of a transient underexpanded impinging jet operating at (left column) $Ma_{sh} = 1.5, s/D = 2.0$ and (right column) $Ma_{sh} = 1.8, s/D = 2.0$.

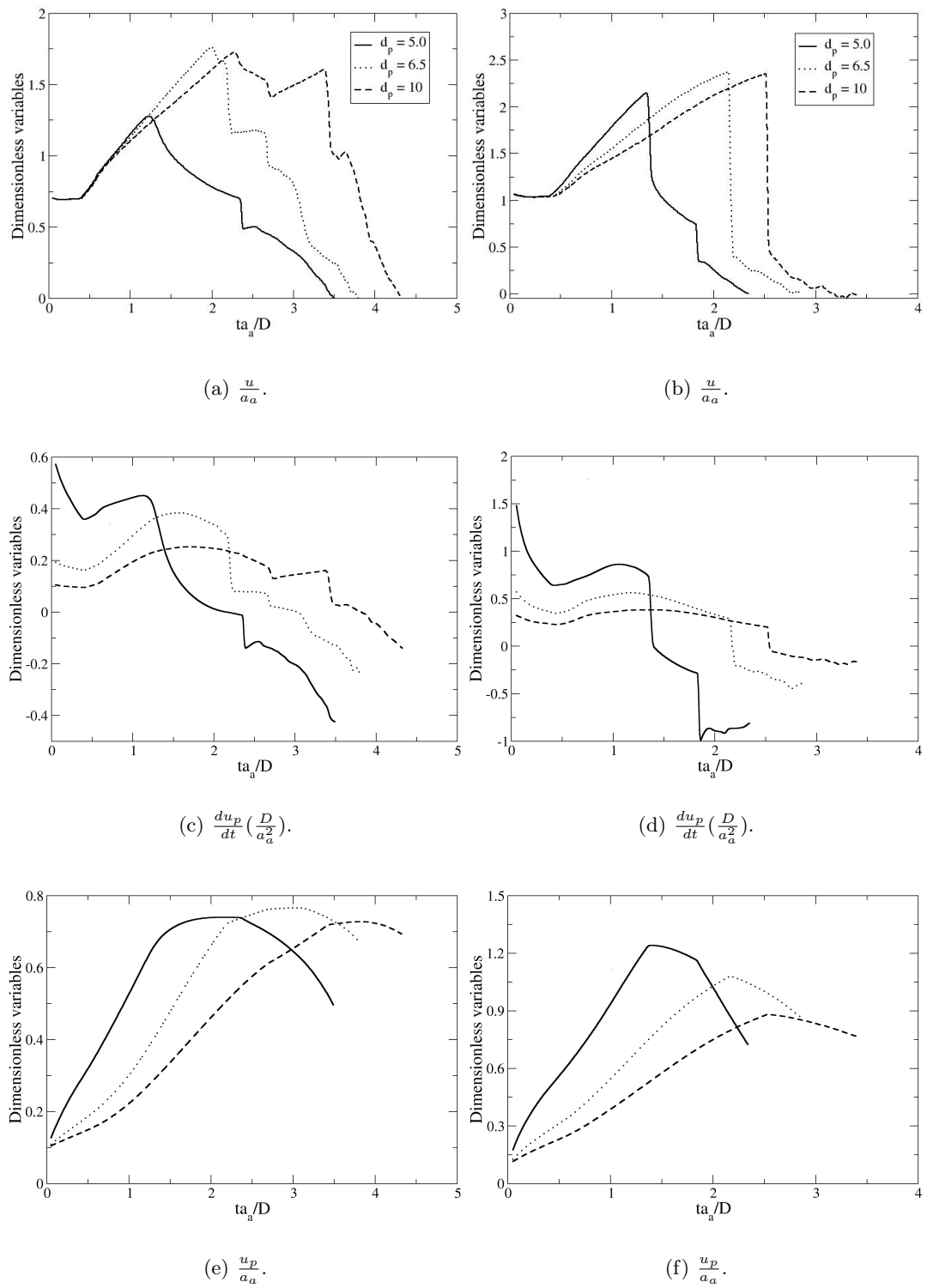


FIGURE 3.45: Time history of a particle injected at $r/D = 0.1$ across the pipe exit into a transient underexpanded impinging jet operating at (left column) $Ma_{sh} = 1.5$, $s/D = 2.0$ and (right column) $Ma_{sh} = 1.8$, $s/D = 2.0$. Note that the particle diameter is in units of μm .

Flow morphology

A series of numerical 'schlieren' flow visualisations for the 'moderately underexpanded' transient jet is shown in Figure.3.40. After the planar shock exits the pipe, it gradually distorts into a spherical shape. This is accompanied by the generation of a large vortex from the pipe wall. As the vortex convects downstream, the jet boundary and inner jet shock are formed intersecting with the tail shock at the triple point (see Figure.1.9 for the schematic of a supersonic impinging jet) as observed at $ta_a/D = 1.0$. A weak Mach disk can be seen at $ta_a/D = 1.5$ which is responsible for the decrease in axial velocity at $z/D \simeq 0.5$ in Figure.3.39. After the spherical shock impinges on the wall, a portion of it is reflected back towards the incoming tail shock and Mach disk. The Mach disk disappears with time and a diamond like shock structure is formed by the jet boundary, inner shock and tail shock. In order to gain a better understanding of the flow properties in relation to the shock structure, the velocity, density and pressure profiles are extracted in both the streamwise and spanwise direction.

Prior to the impact of the spherical shock at $ta_a/D < 1.5$, the flow near the jet centerline $r/D = 0.1$ displays a trend similar to that of a flow through a de-Laval nozzle. Looking at Figure.3.42, the gas velocity increases downstream from the pipe exit as the pressure and density decreases. This is analogous to flow through the converging section of a de-Laval nozzle. The velocity then decreases as the pressure and density increases towards the spherical shock. This is analogous to flow through the diverging section of a de-Laval nozzle. The location of the 'nozzle throat' appears to correspond to where the incipient Mach disk intersects with the jet axis (at $ta_a/D = 1.0$ the 'throat' is positioned at $z/D \simeq 0.4$). The location of the planar shock can be easily identified by the sudden discontinuity in each profile (at $ta_a/D = 1.0$, the shock is located at $z/D \simeq 1.5$). Ideally, the planar shock should result in a sudden step change in flow properties. However, due to the nature of TVD schemes, the inherent artificial viscosity tends to smear the discontinuity across several cells. The spherical shock behaves similar to a moving shock because the gas velocity relative to the shock decreases in the post shock region while the pressure and density increases.

A portion of the spherical shock is reflected from the substrate towards the pipe at around $ta_a/D = 1.5$. Despite the change in shock direction, the relative gas velocity decreases across the reflected shock near the jet centerline while the pressure and density increases. The presence of a Mach disk is still evident from the sudden decrease in

velocity near $z/D \simeq 0.6$. The Mach disk is similar to a moving shock in that the flow experience a sudden increase in both the density and pressure while being stepped down in speed. Referring to Figure.3.40, the Mach disk appears to have disappeared by $ta_a/D = 2.5$ and the inner and tail shocks intersect directly on the jet centerline. The effect of this change in flow field is manifested in the velocity profiles (Figure.3.42) where a small plateau region can be observed in the region bounded by the inner and tail shock. (At $ta_a/D = 2.5$, this occurs at $0.6 \lesssim z/D \lesssim 0.8$) The velocity then decrease non-linearly between the tail shock ($z/D \simeq 0.8$) and reflected shock ($z/D \simeq 1.25$) as the pressure and density both reach steady values.

Once the tail and reflected shocks merge at $ta_a/D = 3$, the flowfield in the jet core and impingement region approaches steady state though the reflected shock exhibits some variation in its position. The velocity profile decreases between the inner and tail shock ($0.6 \lesssim z/D \lesssim 0.8$) and then increases up until the reflected shock at $z/D \simeq 1.2$. The gas then undergoes two rapid drops in velocity at $z/D \simeq 1.2$ and 1.3 before plateauing in a small region defined by $z/D \simeq 1.4$ and 1.5 . On the contrary, the gas pressure and density increases in the region between the inner and tail shock followed by a decrease in magnitude between the tail and reflected shock. A rapid increase near $z/D \simeq 1.2$ is observed after which the variation in density and pressure is minimal. The change in flow properties at $z/D \simeq 1.2$ is consistent with that produced by the reflected shock. However, it is difficult to distinguish any shocks in this region which may be responsible for the small plateau in the velocity and density profile.

A series of numerical 'schlieren' flow visualisations for the 'highly underexpanded' transient jet is shown in Figure.3.41. The Mach disk can be seen at $ta_a/D = 1.5$ and is responsible for the decrease in axial velocity at $z/D \simeq 1.0$ in Figure.3.39. After the spherical shock impinges on the wall, a portion of it is reflected back towards the incoming tail shock and Mach disk. However, unlike the 'moderately underexpanded' impinging jet, the Mach disk remains in the flow even after merging with the tail and reflected shocks. Hence, the absence of a small plateau region near the jet axis at all times in Figure.3.42. A fourth discontinuity - referred to as the slip line in literature (see.Chapter.1.4)- is formed at the triple point which transforms into a series of small vortices downstream. Two faint 'shocks' can be observed in the wake of the Mach disk. These may be the contact waves observed by Henderson *et al.* (2005) and Risborg & Soria (2008) in their study of highly underexpanded impinging jets. To confirm the

Case	P_0 (MPa)	T_0 (K)	Ma_e	PR	U_p
B	1.25	300	2.2	1.2	282
C	0.54	300	2.1	0.63	359

TABLE 3.3: Impact speeds of a 10 μm Aluminium particles injected at $r/D = 0.1$ during the steady cold spray process.

Case	P_P (MPa)	T_P (K)	Ma_{sh}	$\frac{P_P}{P_a}$	U_p
E	0.25	380	1.5	2.5	258
F	0.37	441	1.8	3.6	235

TABLE 3.4: Impact speeds of a 10 μm Aluminium particle injected at $r/D = 0.1$ during the unsteady cold spray process.

existence of these waves, the density and pressure profiles are plotted. At $z/D \simeq 1.4$ and $ta_a/D = 3.0$, the density of the gas experiences a small sudden increase downstream from the Mach of disk while the pressure decreases. This corresponds to the location of the first of two faint 'shocks' in Figure.3.41 and is not characteristic of flow across a contact wave which requires that the density changes while the pressure remains constant (see Chapter.C.1).

The focus of the discussion will now shift to the spanwise profiles (Figure.3.43) as the jet impingement region approaches steady state. Prior to the junction of the inner and tail shocks at $z/D = 0.3$ in the 'moderately underexpanded' transient jet, the axial velocity experiences a local maxima while the pressure and density both experience a minima across the inner shock at $r/D \simeq 0.25$. The same trend is observed across the tail shock further downstream at $z/D = 1.0$. Near the substrate at $z/D = 1.5$, the spanwise profiles are perfectly smooth due to the absence of flow discontinuities in the impingement region. Judging by the transition from positive to negative axial velocity along the vertical plane, the primary convecting vortex must be rotating in the counter-clockwise direction. The spanwise variation across a 'highly underexpanded' transient jet is similar. To determine the rotation of the vortices trailing from the triple point, the spanwise axial velocity profile along $z/D = 1.5$ is chosen as it intersects one of the these vortices. The sudden increase in radial velocity from negative to positive values at $r/D \simeq 0.4$ suggests that the slip line vortices are rotating in the clockwise direction.

Particle dynamics

The particle trajectories in an unsteady cold spray process are not much different from those in a steady underexpanded or overexpanded impinging jet. As Figure.3.44 shows,

this spread in impact location diminishes as the particles become larger due to its inertia. The local velocity and acceleration of a particle injected at $r/D = 0.1$ is shown in Figure.3.45. The impact speed for three different particle sizes (3, 6.5 and 10 μm) are similar despite strong variation in the local gas velocity. This may be attributed to the small amount of acceleration (drag force per unit mass) acting on the particle relative to that experienced in steady supersonic impinging jets (see Figure.3.32). Comparing Figures.3.32.a and 3.45.d, the maximum deceleration ($\frac{du_p}{dt}(\frac{D}{a_a^2})$) for a 5 μm particle is approximately -4.0 and -1 during the steady and unsteady cold spray process respectively. Another benefit is that when cold spraying very small particles using a shock tube, the greater spread in particle trajectory means a slightly larger coating area as seen when comparing Figures.3.45 and 3.31.

In order to compare the efficiency of the unsteady and steady cold spray processes, the driving pressure and temperature required to achieve a certain impact speed are listed in Table.3.3.4. In steady cold spray processes using a de-Laval nozzle, the chamber pressure (P_0) is estimated using the nozzle expansion ratio and the pressure ratio given in validation cases *B* and *C*. The chamber temperature (T_0) is assumed to be 300 K. In unsteady cold spray processes using a shock tube (Case *E*: $M_{sh} = 1.5$ and *F*: $M_{sh} = 1.8$), the driving pressure and temperature is obtained by applying the normal shock relations across the planar shock. The atmospheric pressure and temperature used in these calculations have been assumed as 101.325 kPa and 288 K respectively. It is clear that the impact speed produced by the unsteady cold spray process is almost as high as the steady process using an underexpanded impinging jet. However, the steady underexpanded impinging jet requires a significantly higher nozzle chamber pressure which makes it less efficient.

Chapter 4

Conclusions and future work

A numerical investigation of the cold spray process has been performed. The study is broken down into three parts which examines the gas and particle dynamics during both steady and unsteady cold spray processes. In the first part of the investigation, an examination of the cold spray nozzle is performed in which the particle acceleration is achieved using a diverging section. A barrel section is later attached to the end of a de-Laval (cold spray) and converging (kinetic metallization) nozzle for particle acceleration. The following trends have been established in relation to the particle velocity at the nozzle exit.

1. An increase in the nozzle chamber pressure and diverging length is conducive to increasing the velocity of large particles
2. An increase in the nozzle chamber temperature diminishes in effect for large particles
3. The optimum barrel length for a de-Laval-barrel nozzle increases with particle size and decreasing wall friction
4. The acceleration of particles using a de-Laval-barrel nozzle is more effective for smaller particles while a diverging section is preferred for larger particles
5. The critical particle size for which the de-Laval-barrel nozzle becomes detrimental can be varied through adjustment of the nozzle chamber conditions
6. A low friction barrel section is required to boost the velocity of a wide range of particle sizes
7. The effect of the nozzle chamber conditions are qualitatively similar for both de-Laval and converging nozzles

The second part of the investigation explored the gas and particle dynamics between the nozzle and substrate during the steady cold spray process. An extensive validation of the gas phase simulation is carried out using experimental data of supersonic impinging jets from the fluid literature. The use of Equation.2.51 is only applicable when injecting particles greater than $10\ \mu\text{m}$ in diameter. For both underexpanded and overexpanded impinging jets, the maximum impact velocity is generated when injecting Aluminium particles with a Stokes number of approximately one. The simulations show that an overexpanded nozzle is preferable as it not only requires a lower nozzle chamber pressure but also produces a slightly higher maximum impact velocity. Using a normal shock model, it has been shown that the particle impact speed can be estimated with reasonable accuracy using the nozzle exit conditions. In this model, the nozzle exit gas velocity is brought to rest while undergoing density and temperature increases indicative of those across the bow shock in the real flow. A particle is then injected at the nozzle exit speed prior to the normal shock and decelerated over a distance equal to that between the bow shock and substrate, the final speed being the impact speed. The post shock density and temperature can be estimated using the method of integral relations developed by Gummer & Hunt (1974).

In the third part of the investigation, the numerical 'schlieren' flow visualisations clearly highlighted the shock formation process during unsteady cold spraying. In a 'moderately underexpanded' transient jet, the Mach disk acts like a moving normal shock and reduces in diameter until the inner and tail shocks meet at the jet axis to produce the shock diamond structure. Meanwhile, the propagating planar shock is distorted spherically after leaving the pipe and generates a decrease in gas speed, density and pressure. It behaves like a normal shock before and after being reflected from the impingement surface and merging with the incoming tail shock and Mach disk. The flow field for a 'highly underexpanded' transient jet has a number of features that distinguishes it from the 'moderately underexpanded' jet. The Mach disk remains in the flow as time passes and a slip line emanates from the triple point which transforms into a series of vortices. These rotate in the opposite direction (anti-clockwise) to that of the primary convecting vortex (clockwise). In regards to the particles, it has been shown that the impact speed varies little for different particle diameters. Despite the large drag acting on it, the particles experience a gentle acceleration and deceleration before and after the Mach disk (bow shock). The process is more efficient than the

steady cold spray process but suffers from a number of practical limitations. These include the very limited duration of cold spraying, the need to replace the shock tube after each run and the timing of particle injection to coincide with the passing of the planar shock.

A number of recommendations for further research will be outlined before the conclusion of this thesis. The present study has focused only on perpendicular jet impingement while the general application of cold spray would require coatings to be applied on surfaces with curvatures (i.e. pipes and airfoils). To model this type of jet impingement, a three dimensional model is required to capture the full physics of the high speed multiphase flow. For a more realistic model of the gas and particle interaction, the coupling between the two phases as well as inter-particle collisions needs to be incorporated into the three dimensional model. The Godonov type finite volume methods are specifically designed for hyperbolic conservations laws such as the Euler equations. Consequently, the turbulence modelling has been by-passed in the present investigation. It has been recommended for future research that the Reynolds Averaged Navier Stokes (RANS) equations be used to assess the effect of turbulence and wall friction on the validation and results. Ideally, it would be preferable to model the supersonic impinging jet flow using either Large Eddy Simulation (LES) or Direct Numerical Simulation (DNS) to capture its turbulent structures and instability modes.

Finally, given the lack of experimental data available for compressible particle-laden jets, a particle tracking technique (i.e.PIV) could be used to measure the response of different sized particles in a supersonic impinging jet. Since the objective here is to measure the velocity of the particle and not that of the gas, the issues commonly associated with particle lagging across flow discontinuities are not a major concern. The key is to find seeding particles which are representative of those used in the cold spray process. More experimental data is also needed for overexpanded impinging jets. These can serve as the benchmark data when verifying the method of integral relations (Gummer & Hunt (1974)) for calculating the bow shock curvature and surface pressure distribution of an overexpanded impinging jet. If the method is demonstrated to be reasonably accurate for overexpanded impinging jets, the normal shock model could well become a standard tool for estimating the particle impact velocity.

Appendix A

Euler equations - Jacobian matrices and eigenvectors

The conservation form of the two-dimensional Euler equations is written as.

$$\frac{\partial \mathbf{U}}{\partial t} + \frac{\partial \mathbf{F}}{\partial x} + \frac{\partial \mathbf{G}}{\partial y} = 0 \quad (\text{A.1})$$

$$\mathbf{U} = \begin{bmatrix} \rho \\ \rho u \\ \rho v \\ E \end{bmatrix}, \quad \mathbf{F} = \begin{bmatrix} \rho u \\ (\rho u^2 + P) \\ \rho uv \\ (E + P)u \end{bmatrix}, \quad \mathbf{G} = \begin{bmatrix} \rho v \\ \rho uv \\ (\rho v^2 + P) \\ (E + P)v \end{bmatrix}$$

The Jacobians matrices $\mathbf{A} = \frac{d\mathbf{F}}{d\mathbf{U}}$ and $\mathbf{B} = \frac{d\mathbf{G}}{d\mathbf{U}}$ are:

$$\mathbf{A} = \begin{bmatrix} 0 & 1 & 0 & 0 \\ -u^2 + \frac{1}{2}(\gamma - 1)\mathbf{V}^2 & (3 - \gamma)u & (1 - \gamma)v & \gamma - 1 \\ -uv & v & u & 0 \\ u(\frac{1}{2}(\gamma - 1)\mathbf{V}^2 - H) & H - (\gamma - 1)u^2 & (1 - \gamma)uv & \gamma u \end{bmatrix}$$

$$\mathbf{B} = \begin{bmatrix} 0 & 0 & 1 & 0 \\ -uv & v & u & 0 \\ -v^2 + \frac{1}{2}(\gamma - 1)\mathbf{V}^2 & (1 - \gamma)u & (3 - \gamma)v & \gamma - 1 \\ v(\frac{1}{2}(\gamma - 1)\mathbf{V}^2 - H) & (1 - \gamma)uv & H - (\gamma - 1)v^2 & \gamma v \end{bmatrix}$$

where $\mathbf{V}^2 = u^2 + v^2$ and $H = \frac{1}{2}\mathbf{V}^2 + \frac{a^2}{\gamma - 1}$. The eigenvalues of \mathbf{A} and \mathbf{B} are $\lambda_x^1 = u - c$, $\lambda_x^2 = u$, $\lambda_x^3 = u + c$, $\lambda_x^4 = u$ and $\lambda_y^1 = v - c$, $\lambda_y^2 = v$, $\lambda_y^3 = v + c$, $\lambda_y^4 = v$ respectively.

The right eigenvectors of matrix \mathbf{F} and \mathbf{G} form the columns of matrix $\mathbf{K}_{i+1/2}$ and $\mathbf{K}_{j+1/2}$ respectively.

$$\mathbf{K}_{i+1/2} = \begin{bmatrix} 1 & 1 & 1 & 0 \\ u - c & u & u + c & 0 \\ v & v & 1 & 0 \\ H - uc & \frac{1}{2}(u^2 + v^2) & H + uc & v \end{bmatrix}_{i+1/2}$$

$$\mathbf{K}_{j+1/2} = \begin{bmatrix} 1 & 1 & 1 & 0 \\ u & u & u & 1 \\ v-c & v & v+c & 0 \\ H-vc & \frac{1}{2}(u^2+v^2) & H+vc & u \end{bmatrix}_{j+1/2}$$

The left eigenvector of matrices \mathbf{F} and \mathbf{G} form the rows of matrix $\mathbf{K}_{i+1/2}^{-1}$ and $\mathbf{K}_{j+1/2}^{-1}$ respectively.

$$\mathbf{K}_{i+1/2}^{-1} = \begin{bmatrix} \frac{1}{2}(b_1 + \frac{u}{c}) & \frac{1}{2}(-b_2u) & \frac{1}{2}(-b_2v) & \frac{b_2}{2} \\ 1-b_1 & b_2u & b_2v & -b_2 \\ \frac{1}{2}(b_1 - \frac{u}{c}) & \frac{1}{2}(-b_2u + \frac{1}{c}) & \frac{1}{2}(-b_2v) & \frac{b_2}{2} \\ -v & 0 & 1 & 0 \end{bmatrix}_{i+1/2}$$

$$\mathbf{K}_{j+1/2}^{-1} = \begin{bmatrix} \frac{1}{2}(b_1 + \frac{v}{c}) & \frac{1}{2}(-b_2u) & \frac{1}{2}(-b_2v - \frac{1}{c}) & \frac{1}{2}b_2 \\ 1-b_1 & b_2u & b_2v & -b_2 \\ \frac{1}{2}(b_1 - \frac{u}{c}) & \frac{1}{2}(-b_2u) & \frac{1}{2}(-b_2v + \frac{1}{c}) & \frac{1}{2}b_2 \\ -u & 1 & 0 & 0 \end{bmatrix}_{j+1/2}$$

where

$$H = \frac{c^2}{\gamma-1} + \frac{u^2+v^2}{2}$$

$$b_1 = b_2 \frac{u^2+v^2}{2}$$

$$b_2 = \frac{\gamma-1}{a^2}$$

The matrices \mathbf{A} and \mathbf{B} are diagonalisable because there exists a diagonal matrix $\mathbf{\Lambda}$ whose diagonal elements are the eigenvalues of the matrices such that the following relation is satisfied.

$$\mathbf{A} = \mathbf{K}_{i+1/2} \mathbf{\Lambda}_{i+1/2} \mathbf{K}_{i+1/2}^{-1} \quad \mathbf{B} = \mathbf{K}_{j+1/2} \mathbf{\Lambda}_{j+1/2} \mathbf{K}_{j+1/2}^{-1} \quad (\text{A.2})$$

where

$$\mathbf{\Lambda}_{i+1/2} = \begin{bmatrix} \lambda_x^1 & \cdots & 0 \\ \vdots & \ddots & \vdots \\ 0 & \cdots & \lambda_x^4 \end{bmatrix}_{i+1/2}$$

$$\mathbf{\Lambda}_{j+1/2} = \begin{bmatrix} \lambda_y^1 & \cdots & 0 \\ \vdots & \ddots & \vdots \\ 0 & \cdots & \lambda_y^4 \end{bmatrix}_{j+1/2}$$

To find the values at the mid-point $i+1/2$, Roe's averaging is employed as follows:

$$\begin{aligned}
u_{i+1/2} &= \frac{(\rho u)_{i+1} + (\rho u)_i}{\sqrt{\rho_{i+1}} + \sqrt{\rho_i}} \\
v_{i+1/2} &= \frac{(\rho v)_{i+1} + (\rho v)_i}{\sqrt{\rho_{i+1}} + \sqrt{\rho_i}} \\
c_{i+1/2} &= \frac{(\rho c)_{i+1} + (\rho c)_i}{\sqrt{\rho_{i+1}} + \sqrt{\rho_i}} \\
H_{i+1/2} &= \frac{1}{2}(u_{i+1/2}^2 + v_{i+1/2}^2) + \frac{c_{i+1/2}^2}{\gamma - 1}
\end{aligned} \tag{A.3}$$

The same method applies for calculating the values at the mid-point $j + 1/2$.

Appendix B

Total variation diminishing (TVD) schemes

This section focuses on the resolution of two contradictory requirements of Godunov methods, namely high-order accuracy and the absence of spurious oscillation in the vicinity of large gradients. It is well known that high-order linear schemes produce unphysical oscillations in the vicinity of large gradients. On the other hand, monotone schemes does not have this problem but is of limited use because it is only first order accurate. These difficulties are embodied in Godunov's theorem (Godunov (1954)). One way of obtaining high order schemes which produce minimal oscillations near discontinuities is to construct non-linear methods.

The discussion on TVD property is centered around the solution of the linear advection equation

$$\frac{\partial u}{\partial t} + \frac{\partial f(u)}{\partial x} = 0 \qquad f(u) = cu \qquad (\text{B.1})$$

where c is a constant wave propagation speed.

Given an initial square wave profile $u_0(x)$, the linear advection equation simply translate this profile at a velocity of a to the right if $a > 0$ and to the left if $a < 0$. The general form of schemes used to solve this equation are

$$u_i^{n+1} = \sum_{k=-k_L}^{k_R} b_k u_{i+k}^n \qquad (\text{B.2a})$$

or alternatively

TABLE B.1: Linear schemes for solving the linear advection equation in the form of Equation.B.2a and B.2b

Scheme	b_{-1}	b_0	b_1
Godunov upwind $c > 0$	c	$1 - c$	0
Godunov upwind $c < 0$	0	$1 + c$	$-c$
Lax-Wendroff	$\frac{1}{2}c(1 + c)$	$1 - c^2$	$-\frac{1}{2}c(1 - c)$

Scheme	β_0	β_1
Godunov upwind	$\frac{1}{2}(1 + \text{sign}(c))$	$\frac{1}{2}(1 - \text{sign}(c))$
Lax-Wendroff	$\frac{1}{2}(1 + c)$	$-\frac{1}{2}(1 - c)$

$$u_i^{n+1} = u_i^n + \frac{\Delta t}{\Delta x}(f_{i-1/2} - f_{i+1/2}) \quad f_{i+1/2} = \sum_{k=-k_L}^{k_R} \beta_k(cu_{i+k}^n) \quad (\text{B.2b})$$

where k_L and k_R are two non-negative integers. Table.B.1 lists several linear schemes of first and second order accuracy. The Godunov scheme is first order accurate in space and time whereas the Lax-Wendroff scheme is second order accurate in space and time. A von-Neumann stability analysis shows that the schemes are conditionally stable for $0 < c < 1$

A scheme is monotone when the coefficients b_k are positive or zero. These schemes have the property that the minima and maxima in the solution decreases with time and thus spurious oscillations do not appear. An examination of the coefficients in Table.B.1 indicates that the Godunov schemes are monotone and the Lax-Wendroff scheme is not. It can be seen from Figure.B.1 that the first order Godunov method tends to smooth out large gradients while the second order Lax-Wendroff method produces spurious oscillation near the vicinity of large gradients.

Godunov's theorem states that the desirable properties of accuracy and monotonicity are for linear schemes contradictory requirements. The key to circumventing this theorem lies within the schemes having fixed coefficients. Roe (1981) constructed adaptive (non-linear) schemes that could adjust themselves to the local nature of the solution. A scheme is total variation diminishing when

$$TV(u^{n+1}) < TV(u^n) \quad \forall n \quad (\text{B.3})$$

where

$$TV(u^n) = \sum_{i=-\infty}^{\infty} |u_{i+1}^n - u_i^n|$$

Harten (1983) proved that the following class of nonlinear schemes

$$u_i^{n+1} = u_i^n - C_{i-1/2} \Delta u_{i-1/2} + D_{i+1/2} \Delta u_{i+1/2} \quad \Delta u_{i-1/2} = u_{i+1}^n - u_i^n \quad (\text{B.4})$$

is TVD given the data dependent coefficients satisfy the following conditions

$$C_{i-1/2} > 0 \quad D_{i+1/2} > 0 \quad 0 < C_{i-1/2} + D_{i+1/2} < 1 \quad (\text{B.5})$$

A high-order TVD scheme can be constructed which requires a higher order flux $f_{i+1/2}^{HO}$ associated with a scheme of accuracy greater than or equal to two and a low order flux $f_{i+1/2}^{LO}$ associated with a monotone first order scheme:

$$f_{i+1/2}^{TVD} = f_{i+1/2}^{LO} + \phi_{i+1/2} (f_{i+1/2}^{HO} - f_{i+1/2}^{LO}) \quad (\text{B.6})$$

In order to satisfy Harten's theorem, a suitable limiter function $\phi_{i+1/2}$ must be defined so that it satisfies Equation.B.5. As an example, the Godunov upwind scheme is employed for the lower order flux and the Lax-Wendroff scheme is employed for the higher order flux.

For the case $c > 0$, substitution of these coefficients for the low and high order flux from Table.B.1 followed by rearranging into the form of Equations.B.4 produces

$$\begin{aligned} u_i^{n+1} &= u_i^n - C_{i-1/2} \Delta u_{i-1/2} + D_{i+1/2} \Delta u_{i+1/2} \\ C_{i-1/2} &= c \left[1 + \left(\frac{1}{2} (1+c) - 1 \right) \phi_{i+1/2} \right] \\ D_{i+1/2} &= -c \left[\frac{1}{2} (1-c) \phi_{i+1/2} \right] \end{aligned} \quad (\text{B.7})$$

For the case $c < 0$, Equations.B.4 becomes

$$\begin{aligned} u_i^{n+1} &= u_i^n - C_{i-1/2} \Delta u_{i-1/2} + D_{i+1/2} \Delta u_{i+1/2} \\ C_{i-1/2} &= c \left[\frac{1}{2} (1+c) \phi_{i+1/2} \right] \\ D_{i+1/2} &= -c \left[1 + \left(\frac{1}{2} (1-c) - 1 \right) \phi_{i+1/2} \right] \end{aligned} \quad (\text{B.8})$$

The top two figures in Figure.B.1 plots the results generated using a second order and first order monotone scheme. The higher order scheme produced spurious oscillations near the discontinuities whereas the monotone scheme smeared out the original square profile. Only the high order TVD scheme using ULTRA and SUPERA limiters almost reproduced the exact solution as shown in the bottom two figures.

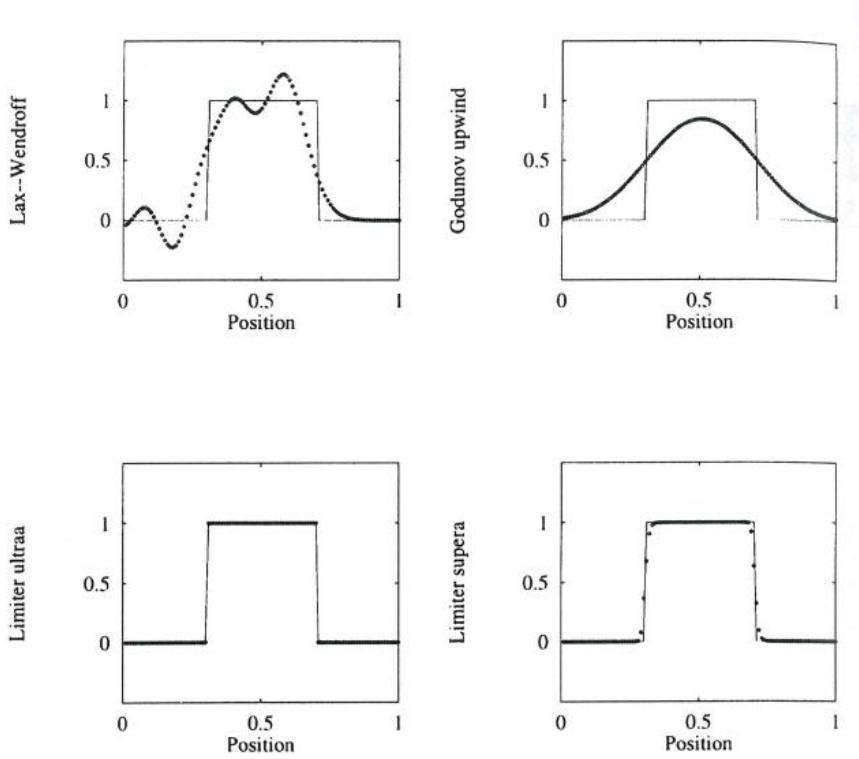


FIGURE B.1: Solution of the linear advection equation with an initial square profile. (Top) Monotone schemes (Bottom) TVD schemes

Appendix C

Compressible flow through a duct with variable cross section area

The governing equations for compressible flow through a duct with variable area may be found in integral form from Shapiro (1953)

$$\frac{dMa^2}{Ma^2} = -\frac{2(1 + \frac{\gamma-1}{2}Ma^2)}{1 - Ma^2} \frac{dA}{A} + \frac{\gamma Ma^2(1 + \frac{\gamma-1}{2}Ma^2)}{1 - Ma^2} 4f \frac{dx}{D} \quad (\text{C.1a})$$

$$\frac{d\rho}{\rho} = \frac{Ma^2}{1 - Ma^2} \frac{dA}{A} - \frac{\gamma Ma^2}{2(1 - Ma^2)} 4f \frac{dx}{D} \quad (\text{C.1b})$$

$$\frac{du}{u} = -\frac{1}{1 - Ma^2} \frac{dA}{A} + \frac{\gamma Ma^2}{2(1 - Ma^2)} 4f \frac{dx}{D} \quad (\text{C.1c})$$

The assumptions made in its derivation include:

1. Steady one dimensional adiabatic flow with no work or potential energy changes
2. Constant wall shear stress along the duct walls
3. No heat or mass transfer across the duct walls

To make these equations practical for modelling the gas dynamics through a diverging section of a de-Laval nozzle, they need to be integrated axially.

Mach number equation

Starting with Equation.C.1.a, the term $\frac{dA}{A}$ needs to be redefined in terms of $\frac{dx}{D(x)}$ so that it can then be integrated by parts. An expression for the nozzle diameter assuming a linear variation between the throat and exit is given below.

$$D = D_t + k_1 x \quad (\text{C.2})$$

where $k_1 = \frac{D_e - D_t}{L_d}$. The corresponding area is given by $A = \pi \frac{D^2}{4}$ and when differentiated with respect to dx becomes

$$\frac{dA}{dx} = \frac{\pi D k_1}{2} \quad (\text{C.3})$$

Dividing by the local nozzle cross section area gives an expression for $\frac{dA}{A}$

$$\frac{dA}{A} = \frac{2k_1}{D} dx \quad (\text{C.4})$$

Equation.C.1.a can then be written as

$$\frac{dv}{v} = \left[-4k_1 \frac{2(1 + k_2 v)}{1 - v} + 4 \frac{k_3 v(1 + k_2 v)}{1 - v} \right] \frac{dx}{D} \quad (\text{C.5})$$

where $k_2 = \frac{\gamma - 1}{2}$, $k_3 = \gamma f$ and $v = Ma^2$.

Rearranging and applying the integrals gives the following problem

$$\int_1^v \frac{1 - v}{4v(1 + k_2 v)(k_3 v - k_1)} dv = \int_0^x \frac{dx}{D} \quad (\text{C.6})$$

The integration is performed from the nozzle throat to a point x downstream. The solution to the integral on the left hand side is found by rearranging it as a partial fraction

$$\frac{A_1}{4v} + \frac{B_1}{1 + k_2 v} + \frac{C_1}{k_3 v - k_1} = \frac{1 - v}{4v(1 + k_2 v)(k_3 v - k_1)} \quad (\text{C.7})$$

The denominator can be condensed into the form

$$1 - v = A_1(1 + k_2 v)(k_3 v - k_1) + B_1 4v(k_3 v - k_1) + C_1 4v(1 + k_2 v) \quad (\text{C.8})$$

and the constants A_1, B_1 and C_1 are found by setting $v = 0$, $v = \frac{k_1}{k_3}$ and $v = \frac{-1}{k_2}$ respectively.

$$A_1 = -\frac{1}{k_1} \quad B_1 = \frac{k_2(k_2 + k_1)}{4(k_1 k_2 + k_3)} \quad C_1 = \frac{k_3(k_3 - k_1)}{4k_1(k_3 + k_2 k_1)} \quad (\text{C.9})$$

Integration of Equation.C.5 eventually gives

$$\left[\frac{D}{D_t} \right]^{1/k_1} = Ma^{A_1/2} \left[\frac{1 + k_2 Ma^2}{1 + k_2} \right]^{B_1/k_2} \left[\frac{-k_1 + k_3 Ma^2}{k_3 - k_1} \right]^{C_1/k_3} \quad (\text{C.10})$$

The equation can also be written in terms of the area ratio as

$$\left[\frac{A}{A_t} \right]^{1/(2k_1)} = Ma^{A_1/2} \left[\frac{1 + k_2 Ma^2}{1 + k_2} \right]^{B_1/k_2} \left[\frac{-k_1 + k_3 Ma^2}{k_3 - k_1} \right]^{C_1/k_3} \quad (\text{C.11})$$

Density equation

The same method is applied to the density equation (Equation.C.1.b) which in terms of v reads

$$\frac{d\rho}{\rho} = \frac{v}{1-v} \frac{dA}{A} - \frac{\gamma v}{2(1-v)} 4f \frac{dx}{D} \quad (\text{C.12})$$

In order to integrate the above equation, the expression for dA/A from Equation.C.4 is substituted

$$\frac{d\rho}{\rho} = \frac{v}{1-v} 2k_1 - \frac{\gamma v}{2(1-v)} 4f \frac{dx}{D} \quad (\text{C.13})$$

To carry out the integration by parts, $\frac{dx}{D}$ needs to be recast in terms of dv using Equation.C.5

$$\frac{d\rho}{\rho} = \left[\frac{v}{1-v} 2k_1 - \frac{2k_3 v}{(1-v)} \right] \left[\frac{1-v}{4v(1+k_2 v)(k_3 v - k_1)} \right] dv \quad (\text{C.14})$$

which can be simplified to

$$\frac{d\rho}{\rho} = \frac{k_1 - k_3}{2(1+k_2 v)(k_3 v - k_1)} dv \quad (\text{C.15})$$

The integration then becomes

$$\int_{\rho_t}^{\rho} \frac{d\rho}{\rho} = \int_1^v \frac{B}{1+k_2v} + \frac{C}{k_3v-k_1} dv \quad (\text{C.16})$$

with the following solution

$$\frac{\rho}{\rho_t} = \left[\frac{1+k_2Ma^2}{1+k_2} \right]^{A_2/k_2} \left[\frac{k_3Ma^2-k_1}{k_3-k_1} \right]^{B_2/k_3} \quad (\text{C.17})$$

where the constants A_2 and B_2 are given below.

$$A_2 = -\frac{k_2(k_1-k_3)}{2(k_2k_1+k_3)} \quad B_2 = \frac{k_3(k_1-k_3)}{2(k_3+k_2k_1)} \quad (\text{C.18})$$

Velocity equation

For the velocity equation (Equation.C.1.c), the integral that needs to be solved is written as

$$\frac{du}{u} = \left[\frac{-1}{1-v} 2k_1 + \frac{2k_3v}{(1-v)} \right] \left[\frac{1-v}{4v(1+k_2v)(k_3v-k_1)} \right] dv \quad (\text{C.19})$$

which simplifies down to

$$\int_{u_t}^u \frac{du}{u} = \int_1^v \frac{2(k_3v-k_1)}{4v(1+k_2v)(k_3v-k_1)} dv \quad (\text{C.20})$$

Its solution is rather elegant

$$\frac{u}{u_t} = Ma \sqrt{\frac{1+k_2}{1+k_2Ma^2}} \quad (\text{C.21})$$

Bibliography

- ADDY, A. 1981 Effects of axisymmetric sonic nozzle geometry on Mach disk characteristics. *AIAA paper* **19**, 121–122.
- AHN, K., KIM, J. & YOON, Y. 2003 Application of PIV to overexpanded supersonic flows: Possibilities and limits. *Journal of Visualisation* **6(4)**, 353–361.
- VAN ALBADA, G., VAN LEER, B. & ROBERTS, W. 1982 A comparative study of computational methods in cosmic gas dynamics. *Astronomy and Astrophysics* **108**, 76–84.
- ALKHIMOV, A. & KOSAREV, V.F. KLINKOV, S. 2003 Features of cold spray nozzle design. *Journal of Thermal Spray Technology* **12(2)**, 265–281.
- ALKHIMOV, A., KOSAREV, V., NESTEROVICH, N. & PAPYRIN, A. Patent No.1618778, Sept 8, 1990 Method of cold spraying.
- ALVI, F. & IYER, K. 1999 Mean and unsteady flowfield properties of supersonic impinging jets with lift plates. *AIAA paper* **99-1829**, 1–12.
- ARBABANEL, S., GOTTLIEB, D. & HESTHAVEN, J. 1996 Well-posed perfectly matched layers for advective acoustics. *Journal of Computational Physics* **154**, 266–283.
- BOURGOING, A. & REIJASSE, P. 2005 Experimental analysis of unsteady separated flows in a supersonic planar nozzle. *Shock waves* **14(4)**, 251–258.
- BUCKLEY, F. 1975 Mach disk location in jet in co-flowing airstreams. *AIAA paper* **13(1)**, 105–106.
- CARLING, J. & HUNT, B. 1974 The near wall jet of a normally impinging, uniform axisymmetric supersonic jet. *Journal of Fluid Mechanics* **66(1)**, 159–176.
- CARLSON, D. & HOGLUND, R. 1973 Particle drag and heat transfer in rocket nozzles. *AIAA paper* **11**, 259–264.
- CROWE, C., GORE, R. & TROUTT, T. 1985 Particle dispersion by coherent structures in free shear flows. *Particulate Science and Technology* **3**, 149–158.

- CUMBER, P., FAIRWEATHER, M., FALLE, S. & GIDDINGS, J. 1995 Predictions of the structure of turbulent, highly underexpanded jets. *Journal of Fluids Engineering* **117**, 599–604.
- DASH, S., WOLF, D. & SEINER, J. 1985 Analysis of turbulent underexpanded jets, Part I: Parabolized Navier-Stokes model. *AIAA paper* **23**, 505–514.
- DAVIS, E. B. J. 2004 *Handbook of thermal spray technology*, 1st edn. Copublished by the Thermal Spray Society and ASM International.
- DONALDSON, C. & SNEDEKER, R. 1971 A study of free jet impingement. Part 1: Mean properties of free and impinging jets. *Journal of Fluid Mechanics* **45(2)**, 281–319.
- DYKHUIZEN, R. & SMITH, M. 1998 Gas dynamic principles of cold spray. *Journal of Thermal Spray Technology* **7(2)**, 205–212.
- ELAVARASAN, R., VENKATAKRISHNAN, L., KROTHAPALLI, A. & LOURENCO, L. 1999 Twin supersonic impinging jets. *AIAA paper* **392**, 155–181.
- FREUND, J. 1997 Proposed inflow and outflow boundary conditions for direct computation of the aerodynamic sound. *AIAA paper* **35**, 740–742.
- FUKANUMA, H., OHNO, N., SUN, B. & HUANG, R. 2006 In flight particle velocity measurements with DPV-2000 in cold spray. *Surface & Coatings Technology* **201**, 1935–1941.
- GODUNOV, S. 1954 Different methods for shock waves. PhD thesis.
- GRINSTEIN, F., ORAN, E. & BORIS, J. 1986 Numerical simulations of asymmetric mixing in planar shear flows. *Journal of Fluid Mechanics* **165**, 201–220.
- GRUJICIC, M., TONG, C., DEROSSET, W. & HELFRITCH, D. 2003 Flow analysis and nozzle-shape optimization for the cold-gas dynamic spray process. In *Proceedings of the Institution of Mechanical Engineers*.
- GRUJICIC, M., ZHAO, C., DEROSSET, W. & HELFRITCH, D. 2004 Analysis of the impact velocity of powder particles in the cold-gas dynamic-spray process. *Materials Science & Engineering:A* **A368**, 222–230.
- GUMMER, J. & HUNT, B. 1974 The impingement of a uniform, axisymmetric supersonic jet on a perpendicular flat plate. *Aeronautical Quarterly* **12(3-4)**, 221–235.
- GUTMARK, E., SCHADOW, K. & WILSON, K. 1991 Effect of convective Mach number on mixing of coaxial circular and rectangular jets. *Physics of Fluids* **3(1)**, 29–35.

- HADJADJ, A., KUDRYAVTSEV, A. & IVANOV, M. 2004 Numerical investigation of shock-reflection phenomena in overexpanded supersonic jets. *AIAA paper* **42(3)**, 570–577.
- HAMED, A. & VOGIATZIS, C. 1997 Overexpanded two-dimensional convergent-divergent nozzle flow simulations: Assessment of turbulence models. *Journal of Propulsion and Power* **13(3)**, 444–445.
- HARTEN, A. 1983 High resolution schemes for hyperbolic conservation laws. *International Journal of Computers and Fluids* **49**, 357–393.
- HARTEN, A. & OSHER, S. 1987 Uniformly high-order accurate nonoscillatory schemes. *SIAM Review* **24(2)**, 279–309.
- HENDERSON, B., BRIDGES, J. & WERNET, M. 2005 An experimental study of the oscillatory flow structure of tone-producing supersonic impinging jets. *Journal of Fluid Mechanics* **542**, 115–137.
- HENDERSON, B. & POWELL, A. 1993 Experiments concerning tones produced by an axisymmetric choked jet impinging on flat plates. *Journal of Sound and Vibrations* **168(2)**, 307–326.
- HENDERSON, B. & POWELL, A. 1996 Sound producing mechanisms of axisymmetric choked jet impinging on small plates. *Journal of the Acoustical Society of America* **99**, 153–162.
- HOU, T. & LEFLOCH, P. 1994 Why non-conservative schemes converge to the wrong solutions: Error analysis. *Mathematics of Computer Science* **62**, 497–530.
- HU, F. 1996 On absorbing boundary conditions of linearised Euler equations by a perfectly matched layer. *Journal of Computational Physics* **129**, 201–219.
- HUNTER, C. 1998 Experimental, theoretical and computational investigation of separated nozzle flows. *AIAA paper* **1998-3107**.
- IVANOV, M., KUDRYAVTSEV, A., KHOTYANOVSKY, A., NIKIFOROV, S. & PAVLOV, A. 2003 Experiments on shock wave reflection transition and hysteresis in low-noise wind tunnel. *Physics of Fluids* **15(6)**, 1807–1810.
- JEN, T.-C., LI, L., CUI, W., CHEN, Q. & ZHANG, X. 2005 Numerical investigation of cold gas dynamic spray process with nano-and microsize particles. *International Journal of Heat & Mass Transfer* **48**, 4384–4396.
- JODOIN, B. 2002 Cold spray nozzle mach number limitation. *Journal of Thermal Spray Technology* **11(4)**, 496–507.

- JODOIN, B., RALETZ, F. & VARDELLE, M. 2006 Cold spray modeling and validation using an optical diagnostic method. *Surface & Coatings Technology* **200**, 4424–4432.
- KALGHATGI, G. 1976 The occurrence of stagnation bubbles in supersonic jet impinging flows. *Aeronautical Quarterly* **27(3)**, 169–185.
- KALGHATGI, G. & HUNT, B. 1975 The three-shock confluence problem for normally impinging, overexpanded jets. *Aeronautical Quarterly* **26(2)**, 117–132.
- KATANODA, H., FUKUHARA, M. & LINO, N. 2007 Numerical study of combination parameters for particle impact velocity and temperature in cold spray. *Journal of Thermal Spray Technology* **16(5-6)**, 627–633.
- KLINKOV, S., KOSAREV, V. & REIN, M. 2005 Cold spray deposition: Significance of particle impact phenomena. *Aerospace Science and Technology* **9**, 582–591.
- KOSAREV, V., KLINKOV, S., ALKHIMOV, A. & PAPYRIN, A. 2003 On some aspects of gas dynamics of the cold spray process. *Journal of Thermal Spray Technology* **12(2)**, 265–281.
- KROTHAPALLI, A., BUZYNA, G. & LOURENCO, L. 1991 Streamwise vortices in an underexpanded axisymmetric jet. *Physics of Fluids* **3**, 1848–1864.
- KROTHAPALLI, A., RAJKUPERAN, E. & LOURENCO, L. 1999 Flow field and noise characteristics of a supersonic impinging jet. *Journal of Fluid Mechanics* **392**, 155–181.
- KUO, C. & DOWLING, A. 1996 Oscillations of a moderately underexpanded choked jet impinging upon a flat plate. *Journal of Fluid Mechanics* **315**, 267–291.
- LAMONT, P. & HUNT, B. 1980 The impingement of underexpanded, axisymmetric jets on perpendicular and inclined flat plates. *Journal of Fluid Mechanics* **100(3)**, 471–511.
- LEE, K., SETOGUCHI, T., MATSUO, S. & KIM, H. 2004 An experimental study of underexpanded sonic, coaxial, swirl jets. In *Proceedings of the Institution of Mechanical Engineers*.
- LI, C.-J., LI, W.-Y. & LIAO, H. 2006 Examination of the critical velocity for deposition of particles in cold spraying. *Journal of Thermal Spray Technology* **15(2)**, 212–222.
- LOURENCO, L. & KROTHAPALLI, A. 1998 Mesh-free second order accurate algorithm for PIV processing. In *International Conference on Optical Technology and Image Processing in Fluid, Thermal and Combustion flows*, pp. 224–231.

- LUO, X., OLIVIER, H. & FENERCIOGLU, I. 2009 The generation of high particle velocities by shock tunnel technology for coating application. *Shock waves* **11**, 887–892.
- MARK, H. 1959 The interaction of a reflected shock wave with boundary layer in a shock tube. *Tech. Rep.*. NACA TM-1418.
- MASUDA, W. & MORIYAMA, E. 1994 Aerodynamic characteristics of underexpanded coaxial impinging jets. *Journal of Fluid Mechanics* **37(4)**, 769–775.
- MITCHELL, D., HONNERY, D. & SORIA, J. 2009 The influence of shockwave induced velocity gradients on the correlation function. *8th International Symposium on Particle Image Velocimetry*. .
- MORRISETTE, E. & GOLBERG, T. 1978 Turbulent flow separation criteria for overexpanded supersonic nozzles. *Tech. Rep.*. NASA TP 1027.
- MOURONVAL, A., HADJADJ, A., KUDRYAVTSEV, A. & VANDROMME, D. 2002 Numerical investigation of transient nozzle flow. *Shock waves* **12**, 403–411.
- NARAYANAN, A. & DOMODARAN, K. 1993 Mach disk of dual coaxial axisymmetric jets. *AIAA paper* **31(7)**, 1343–1345.
- NICKEL, R., BOBZIN, K., LUGSCHEIDER, E., PARKOT, D., VARAVA, W., OLIVIER, H. & LUO, X. 2007 Numerical studies of the application of shock tube technology for cold gas dynamic spray process. *Journal of Thermal Spray Technology* **16(5-6)**, 720–735.
- NOVOPASHIN, S. & PEREPELKIN, A. 1989 Axial symmetry loss of a supersonic preturbulent jet. *Physics of Fluids* **135**, 290–310.
- OCTOBE, Y., KASHIMURA, H., MATSUO, S., SETOGUCHI, T. & KIM, H. 2008 Influence of nozzle geometry on the near-field structure of a highly underexpanded sonic jet. *Journal of Fluids and Structures* **24**, 281–293.
- PAPAMOSCHOU, D. 2000 Mixing enhancement using axial flow. *AIAA paper* **2000-0093**.
- PAPAMOSCHOU, D. 2001 Experiments on mixing enhancement in dual-stream jets. *AIAA paper* **2001-0668**.
- PAPAMOSCHOU, D. 2004 Fundamental investigation of supersonic nozzle flow separation. *AIAA paper* **2004-1111**.
- PHANI, S., VENKATACHALAPATHY, V., JOSHI, S. & GOVINDAN, S. 2008 Optical diagnostics study of gas particle transport phenomena in cold gas dynamic spraying

- and comparison with model predictions. *Journal of Thermal Spray Technology* **17**(4), 551–563.
- PRASAD, J., MEHTA, R. & SREEKANTH, A. 1994 Impingement of supersonic jets on an axisymmetric deflector. *AIAA paper* **32**, 1535–1538.
- RESHOTKO, E. & TUCKER, M. 1955 Effect of a discontinuity on turbulent boundary layer thickness parameters with applications to shock induced separation. *Tech. Rep.*. NASA TN 3454.
- RISBORG, A. & SORIA, J. 2008 High-speed optical measurements of an underexpanded supersonic jet impinging on an inclined plate. In *28th International Congress on High-Speed Imaging and Photonics*.
- ROE, P. 1980 Approximate Riemann solvers, parameter vectors and difference schemes. *Journal of Computational Physics* **43**, 357–372.
- ROE, P. 1981 Numerical algorithms for the linear wave equation. *Tech. Rep.*. Royal Aircraft Establishment.
- ROSSITER, J. 1964 Wind tunnel experiments on the flow over rectangular cavities at subsonic and transonic speeds. *Tech. Rep.*. Aeronautical research council reports and memo.
- SAMAREH, B. & DOLATABADI, A. 2007 A three-dimensional analysis of the cold spray process: the effects of substrate location and shape. *Journal of Thermal Spray Technology* **16**(5-6), 634–642.
- SHAPIRO, A. 1953 *The Dynamics and Thermodynamics of Compressible Fluid Flow*, 1st edn. The Ronald Press Company.
- SHIMSHI, E., BEN-DOR, G. & LEVY, A. 2009 Viscous simulation of shock-reflection hysteresis in overexpanded planar nozzles. *Journal of Fluid Mechanics* **635**, 189–206.
- SOMMERFELD, M. 1994 The structure of particle-laden, underexpanded free jets. *Shock waves* **3**, 299–311.
- STOLTENHOFF, T., KREYE, H. & RICHTER, H. 2002 An analysis of the cold spray process and its coatings. *Journal of Thermal Spray Technology* **11**(4), 542–550.
- TA'ASAN, S. & NARK, D. 1995 An absorbing buffer zone technique for acoustic wave propagation. *AIAA paper* **95-0164**.
- TAM, C. & WEBB, J. 1993 Dispersion-relation-preserving finite difference schemes for computational acoustics. *Journal of Computational Physics* **107**, 262–281.

- TEDESCHI, G., GOUIN, H. & ELENA, M. 1999 Motion of tracer particles in supersonic flows. *Experiments in Fluids* **26**, 288–296.
- THOMPSON, K. 1987a Lecture series in computational fluid dynamics. *Tech. Rep.*. NASA Technical Memo.
- THOMPSON, K. 1987b Time dependent boundary conditions for hyperbolic systems. I. *Journal of Computational Physics* **68**, 1–24.
- THOMPSON, K. 1990 Time dependent boundary conditions for hyperbolic systems. II. *Journal of Computational Physics* **89**, 439–461.
- TORO, E. 1997 Exact and approximate Riemann solvers for the artificial compressibility equations. *Tech. Rep.*. Manchester Metropolitan University.
- TORO, E. 1999 *Riemann solver and numerical methods for fluid dynamics*, 2nd edn. Springer.
- TORO, E. 2001 *Shock-Capturing Methods for Free-Surface Shallow Flows*, 1st edn. Wiley.
- TORO, E. & CHOU, C. 1993 A linearised Riemann solver for the steady supersonic Euler equations. *International Journal of Numerical Methods in Fluids* **16**, 173–186.
- TORO, E., SPRUCE, M. & SPEARES, W. 1994 Restoration of the contact surface in the HLL Riemann solver. *Shock waves* **4**, 25–34.
- WASISTHO, B., GUERTS, B. & KUERTEN, J. 1997 Simulation techniques for spatially evolving instabilities in compressible flow over a flat plate. *Computers and Fluids* **7**, 713–739.
- WEBER, Y., ORAN, E., BORIS, J. & ANDERSON, JR, J. 1995 The numerical simulation of shock bifurcation near the end wall of a shock tube. *Physics of Fluids* **7(10)**, 2475–2488.
- WERNET, M. 1999 Fuzzy logical digital PIV processing software. In *18th International Congress on Instrumentation for Aerospace Simulation Facilities Conference*.
- WHITE, F. 1999 *Fluid Mechanics*, 4th edn. McGraw-Hill.
- WILMOTH, R. & LEAVITT, L. 1987 Navier-Stokes predictions of multifunction nozzle flows. *Society of Automotive Engineers Transactions* **6.865-6.879**.
- WU, J., FANG, H., YOON, S., KIM, H. & LEE, C. 2005 Measurement of particle velocity and characterization of deposition in aluminium alloy kinetic spraying process **252**, 1368–1377.

- WU, J., TANG, L., LUKE, E., TONG, X.-L. & CINNELLA, P. 2002 Comprehensive numerical study of jet-flow impingement over flat plates. *Journal and Spacecraft and Rockets* **39**(3), 357–366.
- XU, J.-L., LIN, C.-F., SHA, J. & ZHANG, K.-Y. 2006 A PIV study and numerical simulation of overexpanded supersonic impinging jet. In *14th AIAA/AMI Space Planes and Hypersonic Systems and Technologies Conference*.
- YEE, H. 1990 High resolution shock-capturing schemes for inviscid and viscous hypersonic flows. *Journal of Computational Physics* **88**, 31–61.
- ZAMAN, K., DAHL, M., BENCIC, T. & LOH, C. 2002 Investigation of a transonic resonance with convergent-divergent nozzles. *Journal of Fluid Mechanics* **263**, 313–343.
- ZARE-BEHTASH, H., KONTIS, K. & GONGORA-OROZCO, N. 2008 Experimental investigations of compressible vortex loops. *Physics of Fluids* **20**, 105–126.